5-2017

An Integrative Approach to Elucidating the Governing Mechanisms of Particles Movement under Dielectrophoretic and Other Electrokinetic Phenomena

Yu Zhao
Clemson University, yzhao3@g.clemson.edu

AN INTEGRATIVE APPROACH TO ELUCIDATING THE GOVERNING MECHANISMS OF PARTICLES MOVEMENT UNDER DIELECTROPHORETIC AND OTHER ELECTROKINETIC PHENOMENA

A Dissertation
Presented to
the Graduate School of
Clemson University

In Partial Fulfillment
of the Requirements for the Degree
Doctor of Philosophy
Bioengineering

---

by
Yu Zhao
May 2017

Accepted by:
Dr. Guigen Zhang, Committee Chair
Dr. Bruce Gao
Dr. Rodrigo Martinez-Duarte
Dr. Xiangchun Xuan

ABSTRACT

Dielectrophoresis (DEP) has been a subject of active research in the past decades and has shown promising applications in Lab-on-Chip devices. Currently researchers use the point dipole method to predict the movement of particles under DEP and guide their experimental designs. For studying the interaction between particles, the Maxwell Stress Tensor (MST) method has been widely used and treated as providing the most robust and accurate solution. By examining the derivation processes, it became clear that both methods have inherent limitations and will yield incorrect results in certain occasions. To overcome these limitations and advance the theory of DEP, a new numerical approach based on volumetric-integration has been established. The new method has been proved to be valid in quantifying the DEP forces with both homogeneous and non-homogeneous particles as well as particle-particle interaction through comparison with the other two methods. Based on the new method, a new model characterizing the structure of electric double layer (EDL) was developed to explain the crossover behavior of nanoparticles in medium. For bioengineering applications, this new method has been further expanded to construct a complete cell model. The cell model not only captures the common crossover behavior exhibited by cells, it also explains why cells would initiate self-rotation under DEP, a phenomenon we first observed in our experiments.

To take a step further, the new method has also been applied to investigate the interaction between multiple particles. In particular, this new method has been proved to be powerful in elucidating the underlying mechanism of the tumbling motion of pearl

chains in a flow condition as we observed in our experiments. Moreover, it also helps shed some new insight into the formation of different alignments and configurations of ellipsoidal particles.

Finally, with the consideration of the Faradic current from water electrolysis and effect of pH, a new model has been developed to explain the causes for the intriguing flow reversal phenomenon commonly observed (but not at all understood) in AC-electroosmosis (ACEO) with reasonable outcomes.

DEDICATION

To my parents and wife

ACKNOWLEDGMENTS

I would like to thank everyone who has helped and guided me in my journey of PhD research.

First, I would like to sincerely thank my advisor Dr. Guigen Zhang. He is not only my advisor in my academic research but also a mentor in my life. His wisdom and knowledge have always inspired me to come up with innovative ideas in my research. Through his word and deed I have realized that learning how is more important than learning that. This will always be a valuable lesson in my future career and life.

I would express my gratitude to my committee members: Dr. Bruce Gao, Dr. Rodrigo Martinez-Duarte and Dr. Xiangchun Xuan for their valuable advice guiding my research work. I want to also thank my mentors at the Tokyo Electron Technology Center, America, LLC: Dr. Jozef Brcka and Dr. Jacques Faguet. Through in-depth discussion with my committee members and company mentors, I have obtained deeper understanding of the field I have been working on.

I want to thank Mr. Scheen Thurmond of the IBIOE for his kind help in designing my experiments. Without his help, many of the research accomplishments would not be achieved.

I would like to acknowledge all previous and current lab members who has helped me in my research for the past five years, including Johnie Hodge, Samuel Bearden, Hetal Maharaja, Lucy Lu, Zhanhe Liu and Jaylin Carter.

I want to thank all the friends I have made in Clemson. They have brought me a lot of joy in the boring days. They have also offered support and help when I was confused and frustrated. Although there are too many to list, I would particularly like to thank Xinran Tao, Xin She, Yilong Zhou and Xiaotian Wang.

I appreciate the support from all members of the Bioengineering department and the funding support from Tokyo Electron Technology Center, America, LLC.

Lastly, but not least, I would like to thank my parents and wife for their support, love and encouragement.

TABLE OF CONTENTS

Page

Table of Contents (Continued)

Page

Table of Contents (Continued)

Page

Table of Contents (Continued)

Page

LIST OF TABLES

Table Page

LIST OF FIGURES

Figure Page

CHAPTER II

CHAPTER III

List of Figures (Continued)

Figure Page

CHAPTER IV

List of Figures (Continued)

Figure Page

CHAPTER V

List of Figures (Continued)

Figure Page

NOMENCLATURE

$\vec{\boldsymbol{m}}$	dipole moment
$\vec{\boldsymbol{E}}$	electric field
ε_m	permittivity of medium
ε_p	permittivity of particle
f_cm	Clausius-Mossotti factor
σ_p	electric conductivity of particle
σ_m	electric conductivity of medium
ω	angular frequency
$\vec{\vec{\boldsymbol{T}}}$	Maxwell stress tensor
σ	surface charge density
μ	ion mobility
κ	inverse of Debye length
$\vec{\boldsymbol{P}}$	polarization density
c	concentration of electrolyte
T	temperature

ϕ	potential in EDL
η	viscosity of medium
ζ	zeta potential
γ	Intrinsic binding constant
C_{mem}	capacitance of cell membrane
$\vec{\boldsymbol{r}}$	distance vector to rotational axis
C_{ω}	dimensionless drag torque coefficient
$\boldsymbol{u}_{fluid}$	velocity of the fluid
ρ_{fluid}	density of the fluid
$\mathbf{u}_{solid}$	displacement of particle
$\rho_{particle}$	density of particle
$\boldsymbol{\sigma}$	stress tensor
$\boldsymbol{\varepsilon}$	strain tensor
D_i	diffusion coefficient of ion *i*
z_i	valence charge of ion *i*
k_d	forward reaction rate constant of water self-ionization

k_b	backward reaction rate constant of water self-ionization
k_e	reaction rate constant of water electrolysis

CHAPTER ONE

INTRODUCTION

1.1 Background

Numerous efforts have been made toward the development of Lab-on-chip (LOC) devices in recent decades due to their promising potential to be applied in various fields including bioengineering, environmental engineering, food safety and so on (Chin *et al* 2007, Mairhofer *et al* 2009). An LOC device acts as a laboratory which combines different functions and features including concentrating, purification, separation, patterning and sensing all on a single miniaturized chip platform. One typical type of LOC devices is the microfluidic device. The microfluidic devices are operated by controlling the flow of small amount of fluid (usually in the amount of μL) in specifically designed channels to achieve desired functions. To realize more diversified functions, the microfluidic devices are often integrated with other components like electrodes, magnets and/or piezoelectric materials, among others. Electrode structures are most commonly used for two reasons: First, the advancement of modern fabrication techniques allows fabrication of electrodes with elaborate configurations to provide precise control of the electric field distribution. Second, through generation of electric field in the medium, different types of electrokinetic phenomena can be activated and utilized. A lot of work has been done to take advantage of these phenomena toward bioengineering applications such as cell separation and manipulation. Of the many electrokinetic phenomena, DEP has received a lot of attention

in the past two decades because it has been found to be conveniently applicable to cell separation, cell patterning and rapid biofabrication.

DEP was initially discovered as a phenomenon occurring when a dielectric particle is placed in a non-uniform electrical field (Pohl 1951). Depending on the difference in polarization between a particle and its surrounding medium, the particle will move either towards the strong field region (when the particle is more polarizable than the medium) or the weak field region (when the particle is less polarizable than the medium). The work in the past decades has laid the foundation for the development and improvement of DEP theory. This has led to many of the recent works in the field focusing more toward DEP applications and not much on advancing the understanding of the DEP mechanism as if the prevailing DEP theory developed in the past has been well accepted and validated. This appears to be the case even when many observed DEP phenomena could not be explained by the prevailing theory. On the application side, while many microfabrication techniques have been developed to achieve more flexible controls for DEP delivery, all these applications are still in a preliminary stage. There is still a long way to go before DEP driven mechanism can be transformed into viable tools for applications like biosensing and tissue engineering. In the following sections, we will review the achievements made in DEP from three perspectives mentioned above: theory, technology and application.

1.1.1 Theory

The analytical expression for representing the DEP forces exerted on a dielectric particle was developed based on two assumptions: 1) the electric field is uniform and infinite, and 2) the particle is of spherical shape. Under these two assumptions, the particle can be treated as an electric dipole. The force exerted by electric field upon a dipole can be expressed as:

$$\vec{\boldsymbol{F}} = \left(\vec{\boldsymbol{m}} \cdot \nabla\right)\vec{\boldsymbol{E}} \tag{1}$$

where $\vec{\boldsymbol{m}}$ is the dipole moment and $\vec{\boldsymbol{E}}$ is the original electric field at the center of the particle. The potential distribution inside and outside the particle are calculated based on Laplace's equation. The dipole moment can be obtained through the distortion of electric field and the DEP force is thus expressed as:

$$\vec{\boldsymbol{F}} = 2\pi a^3 \varepsilon_m Re(f\_cm)\nabla \boldsymbol{E}_{rms}^2 \tag{2}$$

where a is the radius of the particle, ε_m is the absolute permittivity of the medium, *Re(f_cm*) is the real part of the Clausius-Mossotti factor (Wang *et al* 1994). The Clausius-Mossotti factor is determined by the complex permittivity of particle (ε_p^*) and the medium (ε_m^*) with the following relationship: $f\_cm = (\varepsilon_p^* - \varepsilon_m^*)/(\varepsilon_p^* + 2\varepsilon_m^*)$. The complex permittivity depends upon conductivity ($\sigma_{p,m}$), angular frequency (ω) and the absolute permittivity: $\varepsilon^* = \varepsilon - i\frac{\sigma_{p,m}}{\omega}$. Because the Clausius-Mossotti factor is frequency dependent,

the frequency at which the Clausius-Mossotti factor transits from positive to negative, or vice versa, is called crossover frequency.

Eq. (2), which is derived from the point-dipole model, offers a closed-form analytical expression to quantify the DEP force on a single spherical particle. Based on this expression, the direction and magnitude of the DEP force can be easily obtained from the electric field distribution which is governed by the electrode configuration and biasing signal. Most DEP applications rely on this equation for experimental designs. But this equation has its own limitations due to the assumptions made. For example, the estimated DEP force magnitude is not accurate when the electric field is highly non-uniform. Also, particle-particle interaction and non-homogeneity of particle are not considered. To overcome these limitations, modifications have been made to the point-dipole model. For example, ellipsoidal shaped particle has been considered (Jones 2005) with the use of a modified Clausius-Mossotti factor as a function of axis direction. The new expression allows researchers to determine the DEP force and torque exerted on ellipsoidal particles. As the point dipole model only uses the electric field at the center of particle to calculate the force, the force magnitude is not accurate when the electric field is non-uniform (Liang *et al* 2004). To provide more accurate estimation of the magnitude of DEP forces, multipole model was developed (Jones and Washizu 1996a, Washizu and Jones 1996b). The multipole model considers higher order moments (quadruple, octupole etc) which are represented by dyadic tensors. Initially this model can only be used for spherical shaped particle. Later it has been expanded to account for non-spherical shaped particle (Green

and Jones 2006). However, it requires numerical integration to determine the moments, which negates the advantage of the original analytical expression.

Both the point dipole model and the multipole model only consider the case of an individual particle in electric field. When multiple particles present, especially when one particle gets close to another particle, the dipole of the first particle will generate an electric field affecting the electric field experienced by the second particle. To count for particle-particle interaction, the interaction force between two particles is often represented by an inverse relationship to the fourth order of the distance between the two particles (Stoy 1994). By combing the point-dipole model and the analytical interactive model, the relative movement of multiple particles were considered to understand the governing mechanism of particle interaction (Aubry and Singh 2006, Kadaksham *et al* 2004, 2006). Other than the particle-particle interaction, the interaction between a particle and a wall was also studied (Lo and Lei 2009). However, this effect has not received as much attention as particle-particle interaction. Similar to the point-dipole model, the interaction based on multipole model was also developed (Washizu and Jones 1996c).

To apply the DEP technique to manipulate biological cells, the point-dipole model needs to be modified. Different from a simple dielectric particle, a cell is normally formed by complex inner components. To simplify the cell structure, the cell is often considered to be composed of cell membrane and cytoplasm. The simplification of shell structure yields an effective permittivity of cell which can be expressed as (Gascoyne 1997):

$$\varepsilon_{eff}^{*} = \frac{\varepsilon_2^{*}[(R_2 / R_1)^3 + 2(\varepsilon_1^{*} - \varepsilon_2^{*}) / (\varepsilon_1^{*} + 2\varepsilon_2^{*})]}{(R_2 / R_1)^3 - (\varepsilon_1^{*} - \varepsilon_2^{*}) / (\varepsilon_1^{*} + 2\varepsilon_2^{*})} \tag{3}$$

where R_1 and R_2 are the radius of cytoplasm and cell respectively. ε_1^* and ε_2^* are the complex permittivity of cytoplasm and cell membrane respectively. The two-shell model can be expanded to multiple-shell structure to consider more inner components such as cell nucleus (Huang *et al* 1992, Turcu and Lucaciu 1989).

Unsatisfied with the analytical methods for their inaccurate quantification of force magnitude, researchers have begun to use numerical approach to obtain more accurate results. The Maxwell Stress Tensor (MST) method is currently treated as providing the most accurate and robust solutions to DEP force quantification. The DEP force is calculated by integrating the MST over the surface of the particle as:

$$\vec{\boldsymbol{F}} = \oiint \frac{1}{4}\varepsilon_m \left[(\vec{\boldsymbol{E}}\vec{\boldsymbol{E}}^{*} + \vec{\boldsymbol{E}}^{*}\vec{\boldsymbol{E}}) - |\boldsymbol{E}|^2 \vec{\boldsymbol{U}} \right] \cdot \vec{\boldsymbol{n}} \mathrm{d}A \tag{4}$$

The MST method is mainly used to dynamically analyze the relative movement of particles under particle interaction by combining with other methods (such as Arbitrary Lagrangian Eulerian method) (Ai and Qian 2010, Ai *et al* 2014, Hu *et al* 2015, Xie *et al* 2015). It is commonly regarded that most DEP phenomena can be explained by the MST method at current stage.

1.1.2 Technology

The flourishing applications of DEP rely on the fabrication of miniaturized electrodes, which largely reduces the required electric field strength. The most commonly

used type of electrode, 2D metal electrode, is usually fabricated by using photolithographic approach. Although metal electrode has been criticized for having some limitations, such as electrolysis and induced electro-osmotic flow, it has irreplaceable advantages including low resistance and high resolution of critical features. Different electrode patterns have been designed, such as interdigitated, castellated, spiral and saw tooth, for different application purposes. To compensate the limitation of low volumetric throughput of 2D electrode, 3D metal electrodes have been fabricated by extrapolating (Voldman *et al* 2002). The 3D metal electrodes can be used for trapping and separation purposes. However, the fabrication process is relatively complicated. To simplify the electrode design, arrays of insulating posts have been fabricated to create non-uniform electric field. This design, also named iDEP, provides high throughput and has low fabrication costs (Zellner *et al* 2013). Aside from metal electrodes, other materials can be used to fabricate electrodes. For example, silicon and PDMS can be doped to create conductive composites. Carbon electrodes can be fabricated by pyrolyzing patterned organic material (Martinez-Duarte 2012). Other technological innovations of DEP include contactless DEP (cDEP) and optically-induced DEP (oDEP). In cDEP, electrodes are immersed in side channels filled with high-conductive solution. The side channels are isolated from main channel by thin barrier (Shafiee *et al* 2009). oDEP uses photosensitive material so that the geometry of electrodes can be flexibly varied (Huang *et al* 2013).

1.1.3 Application

The DEP technique has been applied to separate cells. Per the shell model, different types of cells have different frequency responses due to variation in effective permittivity. By tuning the frequency, different types of cells can be guided to accumulate in different regions (Li and Bashir 2002). Cells can also be separated through the difference in DEP force magnitude. With iDEP, live and dead cells form different bands in the gap region between insulating posts (Lapizco-Encinas *et al* 2000). With DEP-FFF (field-flow-fractionation), cells are levitated to different heights and collected in different time periods (Wang *et al* 2000). Later efforts have been made to apply the DEP technique in tissue engineering field for cell patterning. Hepatocytes and endothelial cells were sequentially trapped by one or two sets of stellate concentric electrodes to form liver-like pattern (Ho *et al* 2006, 2013). Through patterning bacteria cells on field-effect-transistors with integrated DEP microelectrodes, the microsystem can be used as pH sensor (Castellamau *et al* 2007). Other than manipulating cells, DEP has also been used to capture tiny particles such as molecules. A single protein molecule has been trapped at the tip of sharp nanoelectrodes (Hölzel *et al* 2005). Nanowires are trapped between the edges of two closely aligned electrodes (Lao *et al* 2006, Freer *et al* 2010). New applications tend to combine DEP with other techniques (e.g. optical sensing) to achieve higher detection sensitivity (Hu *et al* 2014).

1.2 Motivations

Although it is widely considered that current DEP theory has been well developed and can be used to explain most DEP phenomena, this is not true judging from the facts that different methods for DEP quantification are needed to explain different DEP phenomena. The point-dipole model is most often used by researchers in their experiment design as the force direction can be easily predicted to determine the movement direction and accumulation regions of particles. However, as more and more efforts have been shifted from studying cell separation to cell patterning and precise manipulation of single cells, the point dipole method is no longer an effective method. That is also the reason why more and more recent works on DEP use the MST method as the theoretic basis. Although the MST method is so widely used, the torque generated by DEP force is often calculated through surface integration. There appears to be a misconception regarding the DEP force calculated based on the MST method because of its surface integration form. The Maxwell stress tensor is derived in vacuum space with a net charge. It is converted from volume integration to surface integration through Gauss's theorem. The circumstance of a dielectric particle immersed in medium does not quite match the hypothetic condition set forth in the derivation process. Moreover, the MST method does not consider the case of particle with non-uniform dielectric property. It is therefore doubtful if the MST method can be used to study cell behavior under DEP.

The author also noticed that many recent publications on studying the movement of particles with MST method were based on abstract conditions. Most Simulations were

conducted in 2D models and the electrode setups rarely matched the real experimental conditions. Although different algorithms were combined with MST method, the conclusions obtained normally just showed the pearl chain alignment which had already been well known. Not much new insight was provided by these studies.

To advance the DEP application in bioengineering, it is imperative that a new method that can overcome the limitations of both the point-dipole method and MST method and capture all observed DEP phenomena be developed. The new method should be able to accurately quantify the DEP force on both homogeneous and non-homogeneous particles. It should also be able to quantify the interaction force between particles. This new method will then be applied to explain interesting DEP phenomena observed in our experiments. Theses phenomena either have not been reported or not well explained by current DEP theories. It is believed that the works presented here will help elucidate the true governing mechanism of the DEP phenomena such that wide spread applications of DEP in the bioengineering field can be realized.

References

Ai, Y., and Qian, S., "DC dielectrophoretic particle–particle interactions and their relative motions," Journal of colloid and interface science 346, 448-454 (2010)

Ai, Y., Zeng, Z., and Qian, S., "Direct numerical simulation of AC dielectrophoretic particle–particle interactive motions," Journal of colloid and interface science 417, 72-79 (2014)

Aubry, N., and Singh, P., "Control of electrostatic particle-particle interactions in dielectrophoresis," EPL (Europhysics Letters) 74, 623-629 (2006)

Chin, C. D., Linder, V., and Sia, S. K., "Lab-on-a-chip devices for global health: Past studies and future opportunities," Lab on a Chip 7, 41-57 (2007)

Freer, E. M., Grachev, O., Duan, X., Martin, S., and Stumbo, D. P., "High-yield self-limiting single-nanowire assembly with dielectrophoresis," Nature nanotechnology 5, 525-530 (2010)

Gascoyne, P. R., Wang, X. B., Huang, Y., and Becker, F. F., "Dielectrophoretic separation of cancer cells from blood. IEEE transactions on industry applications," 33, 670-678 (1997)

Green, N. G., and Jones, T. B., "Numerical determination of the effective moments of non-spherical particles," Journal of Physics D: Applied Physics 40, 78-85 (2006)

Ho, C. T., Lin, R. Z., Chang, W. Y., Chang, H. Y., and Liu, C. H., "Rapid heterogeneous liver-cell on-chip patterning via the enhanced field-induced dielectrophoresis trap," Lab on a Chip 6, 724-734 (2006)

Ho, C. T., Lin, R. Z., Chen, R. J., Chin, C. K., Gong, S. E., Chang, H. Y., Peng, H. L., Hsu, L., Yew, T. R., Chang, S. F., and Liu, C. H., "Liver-cell patterning lab chip: mimicking the morphology of liver lobule tissue," Lab on a Chip 13, 3578-3587 (2013)

Hölzel, R., Calander, N., Chiragwandi, Z., Willander, M., and Bier, F. F., "Trapping single molecules by dielectrophoresis," Physical review letters 95, 128102 (2005)

Hu, S., Zhao, Y., and Hu, H., "Modeling and simulation of tapered fiber-optic oil concentration sensor using negative dielectrophoresis," Sensors and Actuators B: Chemical 199, 70-75 (2014)

Hu, S., Zhao, Y., and Qian, X. L., "Dielectrophoretic behavior of a single cell when manipulated by optoelectronic tweezers: A study based on COMSOL ALE simulations," Journal of Electrostatics, 75, 72-76 (2015)

Huang, S. B., Wu, M. H., Lin, Y. H., Hsieh, C. H., Yang, C. L., Lin, H. C., Tseng, C. P., and Lee, G. B., "High-purity and label-free isolation of circulating tumor cells (CTCs) in a microfluidic platform by using optically-induced-dielectrophoretic (ODEP) force," Lab on a Chip 13, 1371-1383 (2013)

Huang, Y., Holzel, R., Pethig, R., and Wang, X. B., "Differences in the AC electrodynamics of viable and non-viable yeast cells determined through combined

dielectrophoresis and electrorotation studies," Physics in medicine and biology 37, 1499 (1992)

Jones, T. B., "Electromechanics of Particles," Cambridge University Press, Cambridge (2005)

Jones, T. B., and Washizu, M., "Multipolar dielectrophoretic and electrorotation theory," Journal of Electrostatics 37, 121-134 (1996a)

Kadaksham, J., Singh, P., and Aubry, N., "Dielectrophoresis of nanoparticles," Electrophoresis 25, 2625-3632 (2004)

Kadaksham, J., Singh, P., and Aubry, N., "Manipulation of particles using dielectrophoresis," Mechanics Research Communications 33, 108-122 (2006)

Lao, C. S., Liu, J., Gao, P., Zhang, L., Davidovic, D., Tummala, R., and Wang, Z. L., "ZnO nanobelt/nanowire Schottky diodes formed by dielectrophoresis alignment across Au electrodes," Nano Letters 6, 263-266 (2006)

Lapizco-Encinas, B. H., Simmons, B. A., Cummings, E. B., and Fintschenko, Y., "Dielectrophoretic concentration and separation of live and dead bacteria in an array of insulators," FEMS Microbiol. Lett 189, 39-44 (2000)

Li, H., and Bashir, R., "Dielectrophoretic separation and manipulation of live and heat-treated cells of Listeria on microfabricated devices with interdigitated electrodes," Sensors and Actuators B: Chemical 86, 215-221 (2002).

Liang, E., Smith, R. L., and Clague, D. S., "Dielectrophoretic manipulation of finite sized species and the importance of the quadrupolar contribution," Physical Review E 70, 066617 (2004)

Lo, Y. J., and Lei, U., "Quasistatic force and torque on a spherical particle under generalized dielectrophoresis in the vicinity of walls," Applied Physics Letters 95, 253701 (2009)

Mairhofer, J., Roppert, K., and Ertl, P., "Microfluidic systems for pathogen sensing: a review," Sensors 9, 4804-4823 (2009)

Martinez‐Duarte, R., "Microfabrication technologies in dielectrophoresis applications—A review," Electrophoresis 33, 3110-3132 (2012)

Pohl, H. A., "The motion and precipitation of suspensoids in divergent electric fields," Journal of Applied Physics 22, 869-871 (1951)

Stoy, R. D., "Interactive dipole model for two-sphere system," Journal of Electrostatics 33, 385-392 (1994)

Turcu, I., and Lucaciu, C. M., "Dielectrophoresis: a spherical shell model," Journal of Physics A: Mathematical and General 22, 985 (1989)

Voldman, J., Gray, M. L., Toner, M., and Schmidt, M. A., "A microfabrication-based dynamic array cytometer," Analytical chemistry 74, 3984-3990 (2002)

Wang, X. B., Huang, Y., Becker, F. F., and Gascoyne, P. R., "A unified theory of dielectrophoresis and travelling wave dielectrophoresis," Journal of Physics D: Applied Physics 27, 1571-1574 (1994)

Wang, X. B., Yang, J., Huang, Y., Vykoukal, J., Becker, F. F., and Gascoyne, P. R., "Cell separation by dielectrophoretic field-flow-fractionation," Analytical chemistry, 72, 832 (2000)

Washizu, M., and Jones, T. B., "Generalized multipolar dielectrophoretic force and electrorotational torque calculation," Journal of Electrostatics 38, 199-211 (1996b)

Washizu, M., and Jones, T. B., "Dielectrophoretic interaction of two spherical particles calculated by equivalent multipole-moment method," IEEE Transactions on Industry Applications 32, 233-242 (1996c)

Xie, C., Chen, B., Ng, C. O., Zhou, X., and Wu, J., "Numerical study of interactive motion of dielectrophoretic particles," European Journal of Mechanics-B/Fluids 49, 208-216 (2015)

Zellner, P., Shake, T., Sahari, A., Behkam, B., and Agah, M., "Off-chip passivated-electrode, insulator-based dielectrophoresis (OπDEP)," Analytical and bioanalytical chemistry 405, 6657-6666 (2013)

CHAPTER TWO

ELUCIDATING THE DEP PHENOMENA USING A VOLUMETRIC POLARIZATION APPROACH WITH CONSIDERATION OF THE ELECTRIC DOUBLE LAYER

Abstract

Dielectrophoretic (DEP) phenomena have been explored to great successes for various applications like particle sorting and separation. To elucidate the underlying mechanism and quantify the DEP force experienced by particles, the point-dipole and Maxwell Stress Tensor (MST) methods are commonly used. However, both methods exhibit their own limitations. For example, the point-dipole method is unable to fully capture the essence of particle-particle interactions and the MST method is not suitable for particles of non-homogeneous property. Moreover, both methods fare poorly when it comes to explain DEP phenomena such as the dependence of crossover frequency upon medium conductivity. To address these limitations, we have developed a new method, termed volumetric-integration method, with the aid of computational implementation, to reexamine the DEP phenomena, elucidate the governing mechanism, and quantify the DEP force. The effect of electric double layer (EDL) on particles' crossover behavior is dealt with through consideration of the EDL structure along with surface ionic/molecular adsorption, unlike in other methods where the EDL is accounted for through simply assigning a surface conductance value to the particles. For validation, by comparing with

literature experimental data, we show that our new method can quantify the DEP force on not only homogeneous particles but also non-homogeneous ones, and predict particle-particle interactions fairly accurately. Moreover, we also show that the predicted dependence of crossover frequency upon medium conductivity and particle size agrees very well with experimental measurements.

2.1 Introduction

DEP has been a subject of active research in the past decades and has shown promising applications in Lab-on-Chip devices. One of the active applications of DEP is to manipulate small particles (usually in the range of several microns to tens of microns) like cells for their sorting and separation (Church *et al* 2011, Huang *et al* 1992, Li *et al* 2013). Particles can be separated by being pushed towards either the strong field region or the weak field region through excitation via an alternating current (AC) signal at an appropriate frequency determined by the dielectric properties of particles and surrounding medium. They can also be guided into different channels depending on their physical properties (e.g., particle size). Lately, efforts have been made to explore the application of DEP in biomanufacturing field. For example, cells of different types have been aligned to form 2D tissue-like patterns (Ho *et al* 2006, 2013). Attempts have also been made to construct 3D tissue structures (Ramón-Azcón *et al* 2012). Encouraged by these successes, several technological improvements for DEP applications have also been developed. For example, insulator-based DEP (iDEP) creates large scale arrays and makes use of the

strong local electric field generated by insulating materials to capture cells so that the configuration of electrodes can be largely simplified (Zellner *et al* 2013). Optically-induced DEP (oDEP) takes advantage of the property of photosensitive material so that the control of particles is not limited by fixed geometry of electrodes (Huang *et al* 2013).

2.1.1 Elucidating the DEP phenomena based on the dipole and multipole concepts

While new techniques of DEP applications are emerging constantly, not much progress has been made on elucidating the mechanism governing the DEP phenomena (Pethig 2010). The prevailing DEP theory, which treats particles as point dipoles, predicts the DEP force ($\vec{F}$) exerted on a spherical particle as $\vec{F} = 2\pi a^3 \varepsilon_m Re(f\_cm)\nabla \boldsymbol{E}_{rms}^2$, in which a is the radius of the particle, ε_m the absolute permittivity of the medium, *Re(f_cm)* the real part of the Clausius-Mossotti factor, and $\boldsymbol{E}$ the electrical field (Wang *et al* 1994). This method has its unique advantage as it provides a closed-form expression to quantify the DEP force on individual spherical particles. With this expression, the direction and magnitude of the DEP force on a single spherical particle can be estimated. To date, almost all DEP applications have relied on this expression as the guiding principle, although its limitations are quite obvious. First, due to its point-dipole nature, this method does not consider volumetric polarization of particles, which in turn will distort electric field by the presence of particles. When the influence of surrounding particles is considered, the particle-particle interaction force is often assumed to vary inversely to the fourth order with the distance (L) between particles, or ~$1/L^4$ (Aubry and Singh 2006). Second, although the

force expression is often applied to non-uniform electric field, in its derivation $\boldsymbol{E}$ is actually regarded as a vector independent of any spatial variations (namely a uniform field). In reality, the electric field can be highly non-uniform.

To address these issues, a multipole method containing higher-order terms is developed (Jones and Washizu 1996a, Washizu and Jones 1996b). The contribution of higher-order terms has been found not negligible in certain conditions (Liang *et al* 2004). This multipole method has further been expanded from dealing with individual spherical particles to considering non-spherical particles (Green and Jones 2006) as well as particle-particle interactions (Washizu and Jones 1996c). Although the multipole method provides improved estimate for DEP force, it is rarely used in experimental design or numerical analysis because it is not intuitive how many high-order terms are needed.

2.1.2 Elucidating the DEP phenomenon based on the Maxwell Stress Tensor

While the dipole and multipole methods are useful in estimating the magnitude of DEP force, numerical integration often provides more accurate quantitative solutions. The Maxwell stress tensor (MST) method is one such method currently regarded as providing the most robust and accurate solutions to DEP force quantification. In the MST method, the DEP force is calculated by integrating a stress tensor over the surface of a particle as $\vec{\boldsymbol{F}} = \oiint \vec{\boldsymbol{T}} \cdot \vec{\boldsymbol{n}} \mathrm{d}A$, in which $\overleftrightarrow{\boldsymbol{T}} = \frac{1}{4}\varepsilon_m \left[(\vec{\boldsymbol{E}}\vec{\boldsymbol{E}}^* + \vec{\boldsymbol{E}}^*\vec{\boldsymbol{E}}) - |\boldsymbol{E}|^2 \overleftrightarrow{\boldsymbol{U}} \right]$ is the Maxwell stress tensor, $\vec{\boldsymbol{n}}$ the norm vector along the surface, $\vec{\boldsymbol{E}}$ the electric field at the surface, $\vec{\boldsymbol{E}}^*$ the conjugate of

$\vec{E}$, and $\overleftrightarrow{U}$ the unit tensor (Wang *et al* 1997). This method can be applied to particles of various shapes. Moreover, because the electric-field-distortion effect from neighboring particles has already been considered in the determination of the electric field of a given particle, the obtained DEP force inherently includes the effect of particle-particle interactions.

While the MST method has shed valuable insight into the alignment of particles due to particle-particle interactions (Ai and Qian 2010, Hossan *et al* 2013, Xie *et al* 2015), its application has been limited to studying relative movements of a small number of particles, and in most cases in simplified 2D situations. In applying the MST method, the stress tensor is integrated over the particle surface (Kumar and Hesketh 2012, Song *et al* 2015), which often leads to a misconception that the resulting force is a physical surface force. This in turn could result in incorrect predictions of DEP force and physical movement of particles (Rinaldi and Brenner 2002). Moreover, because of the surface integration nature, the MST method is not suited for dealing with particles of non-homogeneous dielectric properties like cells.

2.1.3 Dealing with particles' non-homogeneity and the influence of surface conductivity

To account for the various components of cells, a shell-model approach based on the dipole method is often used by considering the average dielectric property of all components as effective permittivity (Gascoyne *et al* 1997). While this modified dipole

method is useful in predicting the crossover frequency of cells, which is recognized as one crucial metric for cell separation, it does not capture other DEP behavior such as self-rotation of cells in non-rotating electric field (Chau *et al* 2013, Zhao *et al* 2013).

Predicting the crossover frequency of particles possessing different surface property from bulk is often challenging. For example, experimental observations show that small polystyrene particles experience positive DEP (pDEP) at a lower frequency and transition from pDEP to negative DEP (nDEP) as frequency increases (Green and Morgan 1999). This crossover behavior is attributed to the high surface conductivity of the particles caused by the presence of an electric double layer (EDL) at the particle surface (Arnold *et al* 1987, O'Konski 1960). Because polystyrene particles carry net negative surface charge, they will attract positive counter-ions to the surface and form a thin EDL with high conductivity.

Although both the point-dipole method and MST method have been used to study the crossover frequency of polystyrene particles, the influence of EDL is often considered by assigning a surface conductance value without dealing with the actual structure and ion distribution inside the EDL. For example, a typical way to deal with this issue is to express surface conductivity as $K_s = \sigma\mu$ by assuming that the overall surface charge is balanced with counter ions, where σ is the surface charge density and μ the mobility of counter-ions (O'Konski 1960). With this surface conductivity expression, one can write the total conductivity of the particle as $K_{total} = K_{bulk} + \frac{2K_s}{a}$, where K_{bulk} is the bulk conductivity and a the radius of the particle (Arnold et al. 1987). This relationship, however, does not

capture the dependence of crossover frequency upon medium conductivity (Green and Morgan 1999). One reason, as argued by Green and Morgan, is that the balance between counter-ion density and surface charge density does not hold when the thickness of double layer is not negligible in relation to the size of particle. To reflect this, an additional term accounting for the effect of thickness change in Debye length is included: $K_{total} = K_{bulk} + (A_1 + A_2 \kappa a)\frac{2\sigma\mu}{a}$, where κ is the inverse of Debye length, and A_1 and A_2 are constants determined through curve fitting. A similar approach by Hughes and Morgan (1999) sought empirical fit to the data by adding a term of medium conductivity, σ_m, as $K_{total} = K_{bulk} + \frac{2\sigma\mu}{a} + \frac{2\sigma_m}{\sqrt{\kappa a}}$.

While in both cases the fitting curves match experimental data well, the physical meaning of the relevant terms are not clear. To provide physical relevance, the surface conductivity was divided into two parts: conductance due to charge movement in the Stern layer and conductance due to charge movement in the diffuse layer governed by zeta potential, with both the Stern layer conductance and zeta potential obtained through statistical fit to experimental data (Hughes *et al* 1999). Two main limitations remain with this approach. First, applying an analytical expression derived for a flat surface to the ionic distribution in EDL of a spherical surface could lead to inaccurate results (Yang and Zhang 2007). Second, the Stern layer conductance and zeta potential are interrelated. With an increase in electrolyte concentration, zeta potential will decrease given that the surface charge is fixed (Elimelech and O'Melia 1990). However, the zeta potential and Stern layer

conductance are treated as constants for the full range of medium conductivity (Hughes *et al* 1999), which could lead to errors in solutions.

2.1.4 Purpose of this study

Based on the aforementioned limitations, it is apparent that the true mechanism governing the DEP phenomena appears to be more complicated than we have recognized. In this work we have developed a volumetric polarization method, with the assistance of finite element software COMSOL Multiphysics, to reexamine some of the DEP phenomena and quantify the force by considering particle-particle interaction and investigate the effect of the EDL on the crossover frequency of particles in detail. For outcome assessment, we compare our results with those obtained by the point-dipole method and the MST method, as well as reported observations on DEP phenomena of particles.

2.2 Development of a new method to reexamine DEP phenomena

2.2.1 Considering the volumetric polarization of particles

We consider a spherical infinitesimal unit of a particle which is placed in an electric field, either uniform or non-uniform. As the size of the particle unit becomes negligible in relation to the scale of the electric field, the electric field passing through the particle unit can be treated as approximately constant. Thus, we can express the force acting on the particle unit as:

$$\vec{\boldsymbol{f}} = (\mathrm{d}\vec{\boldsymbol{m}} \cdot \nabla)\vec{\boldsymbol{E}} \tag{1}$$

where $\mathrm{d}\vec{\boldsymbol{m}}$ is the dipole moment of the particle unit and $\vec{\boldsymbol{E}}$ denotes the original electric field (as if the particle possesses the same property as the surrounding medium or is not there) at the location of the particle unit. The induced electric field, namely the difference between the electric field inside the particle unit and the original electric field, is generated by the dipole. The dipole is considered to have a structure of two charges with opposite polarity (Q and $-Q$) separated by a distance of d (d is the diameter of the spherical particle unit). The induced electric field can be represented by the electric field at the center of line connecting two charges:

$$\vec{\boldsymbol{E}}_{particle} - \vec{\boldsymbol{E}} = -\frac{1}{4\pi\varepsilon_m}\frac{Q}{(d/2)^2}\hat{d} + \frac{1}{4\pi\varepsilon_m}\frac{-Q}{(d/2)^2}\hat{d} = -\frac{1}{2\pi\varepsilon_m}\frac{Q}{(d/2)^2}\hat{d} \tag{2}$$

where ε_m is the permittivity of medium and $\hat{d}$ is the unit vector pointing from the negative charge to positive charge.

According to the definition of polarization density $\vec{\boldsymbol{P}}$, we have:

$$\vec{\boldsymbol{E}}_{particle} - \vec{\boldsymbol{E}} = -\frac{1}{4\pi\varepsilon_m}\frac{Q\vec{d}}{(d/2)^3} = -\frac{\mathrm{d}\vec{m}}{3\varepsilon_m \cdot (4/3)\pi(d/2)^3} = -\frac{\vec{\boldsymbol{P}}}{3\varepsilon_m} \tag{3}$$

With Eq. (3), the relationship between the electric fields and polarization of the particle unit can be established as:

$$3\varepsilon_m(\vec{\boldsymbol{E}} - \vec{\boldsymbol{E}}_{particle}) = \vec{\boldsymbol{P}} \tag{4}$$

Clearly, polarization of the particle unit is proportional to the difference between the original electric field and the electric field inside the particle unit. By replacing $\mathrm{d}\vec{\boldsymbol{m}}$ with $\vec{\boldsymbol{P}}\mathrm{d}V$ the force acting on the particle unit becomes:

$$\vec{\boldsymbol{f}} = (\vec{\boldsymbol{P}} \cdot \nabla)\vec{\boldsymbol{E}}\mathrm{d}V = (3\varepsilon_m(\vec{\boldsymbol{E}} - \vec{\boldsymbol{E}}_{particle}) \cdot \nabla)\vec{\boldsymbol{E}}\mathrm{d}V \tag{5}$$

The net force on target particle can then be expressed in a summation as follows

$$\vec{\boldsymbol{F}} = \iiint (3\varepsilon_m(\vec{\boldsymbol{E}} - \vec{\boldsymbol{E}}_{particle}) \cdot \nabla)\vec{\boldsymbol{E}}\mathrm{d}V \tag{6}$$

With this expression the influence of the dielectric property of the particle and medium as well as the possible impact of neighboring particles are all inherently considered. As the derivation process does not rely on assumptions like homogeneous particle and spherical shape, the formula can be applied to calculate DEP force on non-homogeneous particles and irregular shaped particles as well. This new approach is also different from both the point-dipole and MST methods. In the point-dipole method, the electric field is taken at the center of the particle (which seems problematic when the field is location dependent), whereas in the MST method the force density is calculated as the product of charge and electric field.

2.2.2 Considering the effects of the EDL structure and ionic adsorption

As discussed in the Introduction section, the crossover frequency of a particle is affected by its EDL. Therefore, to be able to correctly predict the crossover frequency it is necessary to consider the effect of the EDL structure influenced by ion distributions.

By assuming that the electrolyte is composed of monovalent ions, the concentration of cations and anions in the EDL is expressed as $c \cdot e^{(-\frac{q\phi}{kT})}$ and $c \cdot e^{(\frac{q\phi}{kT})}$, respectively, according to Boltzmann distribution where c is the concentration of electrolyte, q is the elementary charge unit, k is the Boltzmann constant, T is the temperature and ϕ is the potential distribution generated by surface charge. Then by Gauss's law through Poisson equation, ϕ is determined as:

$$-\nabla^2\phi = \frac{F(c \cdot e^{(-\frac{q\phi}{kT})} - c \cdot e^{(\frac{q\phi}{kT})})}{\varepsilon_m} \tag{7}$$

where F is the Faraday constant. The boundary condition at the particle surface can be expressed in terms of surface charge density (σ) as:

$$\vec{\boldsymbol{n}} \cdot \nabla\phi = \frac{\sigma}{\varepsilon_m} \tag{8}$$

With the potential distribution (ϕ) solved from Eq. (7) and (8), the conductivity of any given point inside EDL, K_{EDL}, can be determined:

$$K_{EDL} = \lambda_+ c \cdot e^{(-\frac{q\phi}{kT})} + \lambda_- c \cdot e^{(\frac{q\phi}{kT})} + \frac{F(c \cdot e^{(-\frac{q\phi}{kT})} - c \cdot e^{(\frac{q\phi}{kT})}) \cdot \varepsilon_m}{\eta(\phi - \zeta)} \tag{9}$$

where λ_+ and λ_- are the limiting molar conductivities of the cation and anion, respectively. η is the viscosity of medium and ζ is zeta potential. The first two terms represent the

conductivity due to conductive transfer of ions in the diffuse layer and the third term represents the electro-osmotic conductivity (Lyklema 1995).

Note that the boundary condition given in Eq. (8) is valid only when the surface charge density is constant. However, experimental measurements of electrophoretic mobility of polystyrene particles in potassium chloride (KCl) solutions of different medium conductivities show that specific adsorption of co-ions will take place on the surface of particles (Elimelech and O'Melia 1990). To consider this effect, Langmuir adsorption is used to describe the adsorption process. According to Langmuir adsorption, the surface charge from adsorption σ_s can be expressed as (Lyklema 1995):

$$\sigma_s = \frac{\sigma_{max} \cdot c^* \cdot \gamma \cdot e^{(\frac{q\phi_i}{kT})}}{1 + c^* \cdot \gamma \cdot e^{(\frac{q\phi_i}{kT})}} \tag{10}$$

where σ_{max} represents the maximum amount of charge that can be adsorbed on the surface, c^* is the dimensionless concentration ($c^*=c/(1\ \text{mol/m}^3)$) and γ is the intrinsic binding constant, which is determined by the non-electrostatic adsorption Gibbs energy. ϕ_i is the potential at the inner Helmholtz plane (iHp). The difference between ϕ_i and ϕ_d, which is the potential at the outer Helmholtz plane (oHp), can be determined as (Lyklema 1995):

$$\phi_i - \phi_d = \frac{(\sigma + \sigma_s)d}{\varepsilon_i} \tag{11}$$

where d is the distance between iHp and oHp and ε_i is the permittivity of the region in between. Then Eq. (10) can be modified to

$$\sigma_s = \frac{\sigma_{max} \cdot c^* \cdot \gamma \cdot e^{(\frac{q\phi_d}{kT})} \cdot e^{(\frac{q(\sigma+\sigma_s)d}{\varepsilon_i kT})}}{1 + c^* \cdot \gamma \cdot e^{(\frac{q\phi_d}{kT})} \cdot e^{(\frac{q(\sigma+\sigma_s)d}{\varepsilon_i kT})}} \tag{12}$$

Considering that $\frac{q\sigma_s d}{\varepsilon_i kT}$ is small, the exponential term $e^{(\frac{q\sigma_s d}{\varepsilon_i kT})}$ can be replaced by $1+\frac{q\sigma_s d}{\varepsilon_i kT}$ through Taylor series expansion. In this way, the surface charge from adsorption can be analytically expressed as:

$$\sigma_s = \frac{B\sigma_{max} - A - 1 + \sqrt{(B\sigma_{max} - A - 1)^2 + 4AB\sigma_{max}}}{2B} \tag{13}$$

where $A = c^* \cdot \gamma \cdot e^{(\frac{q\phi_d}{kT})} \cdot e^{(\frac{q\sigma d}{\varepsilon_i kT})}$ and $B = \frac{qAd}{\varepsilon_i kT}$.

By replacing σ with $\sigma + \sigma_s$ in the boundary condition, Eq. (8), the potential distribution and surface ionic adsorption can be recalculated. To determine the crossover frequency, the contribution of adsorbed ions to Stern layer conductance is also included:

$$K_{stern} = \sigma_s \mu_s \tag{14}$$

where μ_s is the mobility of co-ion in the Stern layer. Based on the common understanding that the mobility in the Stern layer is smaller than in the diffuse layer, we assign $\mu_s = 0.5\mu_c$ in the models where μ_c is the mobility of co-ion in the diffuse layer. Through coupling our

volumetric-integration method with our new EDL model, the effect of EDL structure on the electric field distribution is inherently included by accounting for the continuously varying dielectric property within the EDL, unlike in other methods where the influence of EDL is simplified by assigning a surface conductivity.

2.3 Numerical implementation

To solve all these equations simultaneously, we use a computational approach by developing 2D and 3D models using COMSOL Multiphysics with the Electric Current Module and Frequency Domain Study. In these models, the differential electric field is determined by considering cases with and without particle presence. Note that in the case with particle presence, different intrinsic dielectric properties for the particle and the medium are assigned, and in the case without particle presence, the dielectric property of the medium is assigned to the particle as well. With the electric field expressed in a complex form along with possible phase lag between polarization and electric field, the expression for the DEP force in the models is expressed as:

$$\vec{\boldsymbol{F}} = \frac{1}{2} real\left(\oiiint (3\varepsilon_m(\vec{\boldsymbol{E}} - \vec{\boldsymbol{E}}_{particle})\cdot\nabla)\vec{\boldsymbol{E}}^{*}\,\mathrm{d}V\right) \tag{15}$$

For situations with multiple particles, the effect of electrical field distortion caused by the volumetric polarization of surrounding particles is considered when solving the electric fields. The geometry and setup of models are discussed in each individual study in the following sections. It is worth noting that in computational modeling, 2D situations are

regarded as simplified 3D situations with the third dimension assigned a unity in size (1 m in SI units). This means that for all 2D studies, volumetric integration is performed over 2D domains of particles.

2.3.1 Validation through comparisons

A. Quantification of DEP force

Both 2D and 3D COMSOL models are built to quantify the DEP force on a single homogeneous particle. The 2D model geometry shown in Fig. 1(a) represents a square domain with a spherical particle located in the center. The side length of the square domain is 40a and the diameter of the particle 2a (a = 5 μm in this case). The entire left edge of the square domain is grounded and the middle segment of the right edge with length of 10a is biased by an AC signal of 5 V (equivalent to a 10 Vpp biasing in experiments). In this setting, the electric field on the right side will be stronger than on the left side, causing the DEP force exerted on particle to point to the right under pDEP and to the left under nDEP. By considering a third dimension with depth of 40a and placing the spherical particle in the center of the cubic domain we can obtain the geometry of 3D model. To compare our modeling results with those from other methods such as the point-dipole and the MST methods, we quantify the DEP force in x direction. We consider two situations. In the first, both the particle and surrounding medium are treated as pure dielectric material (conductivity equals zero), with the relative permittivity of medium set at 78.5 and the relative permittivity of particle varied from 10 to 150. In the second situation, the influence

of frequency on the DEP force is studied. The relative permittivity and conductivity are set at 78.5 and 10^{-3} S/m for the medium and 2.5 and 10^{-2} S/m for the particle while the frequency is varied from 200 kHz to 10 MHz.

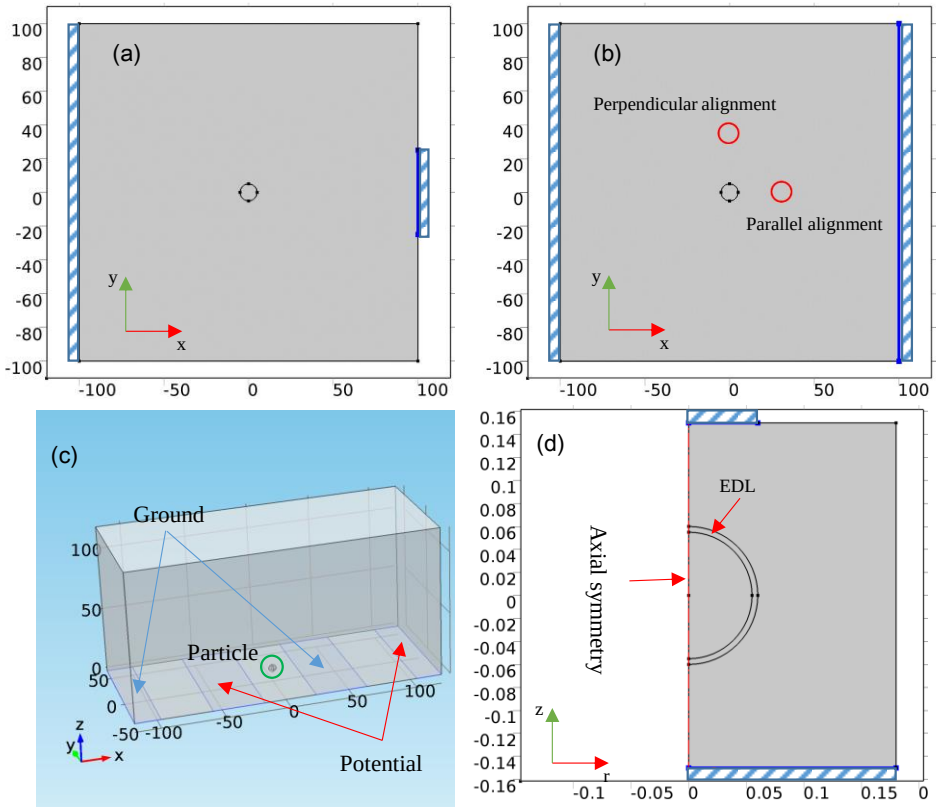

FIG. 1. (a) Geometry of a 2D model for quantifying the DEP force on a single particle located at center of a square domain medium. (b) Geometry of a 2D model for quantifying the particle-particle interaction, with one particle fixed at the center and the other particle (red) placed along either the *x* or *y* direction. (c) Geometry of a 3D model showing a particle in the center region of gap. The bottom electrodes are marked by blue color. (d) Geometry of a 2D axisymmetric model for determining the crossover frequency of polystyrene particles (the outer layer is where the EDL resides).

B. Examination of particle-particle interaction

To study the interaction between two particles, a second 2D model as shown in Fig. 1(b) is built. To minimize the effect of non-uniform electric field, the entire right edge of the square domain is biased to create a uniform electric field. For the two particles, we consider two alignment configurations: 1) parallel to the electric field and 2) perpendicular to the electric field. In both cases, one particle is fixed at the center and the other is placed along either a parallel or perpendicular direction (shown by the red circles). In the model, the distance between the centers of the two particles is varied from 2a to 8a. Additionally we constructed a 3D model by considering a third dimension with depth of 40a and fixing one spherical particle at the center. Parallel and perpendicular alignment of a second particle is considered. For convenience sake, both the particle and medium are treated as pure dielectric material with the relative permittivity for the particle and medium set at 2.5 and 78.5, respectively. The DEP force on the fixed particle in-line with the particles is

determined using our volumetric-integration method, the MST method and point-dipole method.

C. A close look of the crossover behavior of nonhomogenous particles

Aside from investigating the DEP behavior of homogeneous particles, we also investigated the crossover phenomena of nonhomogeneous particles with the same model shown in Fig. 1(a) except that the homogeneous particle is replaced by particle with multiple layers. For non-homogeneous particles, the computational demand will become overwhelming if we mesh the thin layers in 3D model. Thus we only compared the volumetric polarization method and MST method in 2D situations. Polystyrene particles with the entire surface coated with gold or with one half of the surface coated with gold (commonly known as the Janus particle) are considered. For comparison with experimental results, the particles are assigned with the same properties as provided in the literature (table 1) (García-Sánchez *et al* 2012, Zhang and Zhu 2010). The frequency is varied from 10^4 to 10^5 Hz for the particle with entire surface coated by gold and from 25 kHz to 20 MHz for the Janus particle. For the latter, an additional alkanethiol coating atop of the gold part is also considered. Although it might be a debatable issue whether the listed dielectric property of gold is valid for predicting the DEP behavior of particles within the range of frequency examined here (e.g., García-Sánchez stated that the frequency-dependent DEP behavior of gold coated particle is attributed to the EDL charging around gold layer, but in Zhang and Zhu's work Maxwell-Wagner relaxation is applied in shell model without

considering the EDL to explain the crossover behavior of Janus particle), we utilize it in this study for quantitative evaluation purpose.

Table 1. Parameters for particles with entire and half surface coated by gold (García-Sánchez *et al* 2012, Zhang and Zhu 2010)

	Particle with entire surface coated by gold	Particle with half surface coated by gold
Diameter of particle	10 μm	3.8 μm
Thickness of gold layer	50 nm	30 nm
Medium conductivity	0.7 mS/m	2 mS/m
Thickness of alkanethiol layer	NA	2 nm
Relative permittivity of alkanethiol	NA	2.0
Relative permittivity of gold	6.9	
Conductivity of gold	4.5×10^7 S/m	

D. A close look of the particle levitation behavior

To examine particles' levitation behavior, a 3D model is developed to evaluate the vertical levitation height of the particle (6 μm in diameter). Fig. 1(c) shows the 3D model with the same setup and dimensions as in Markx's experiment (1997). For comparison, the vertical lifting DEP force is calculated using the volumetric-integration method, the MST method and the point-dipole method. The levitation height is determined in three steps: First, with a fixed horizontal position, the vertical position of particle is parametrically

varied until a height position is reached where the DEP force is in equilibrium with the net of gravitation and buoyance forces. Second, a series of new horizontal positions for the particle are assigned and the vertical equilibrium positions are found by repeating the previous step. Third, we assess the horizontal stability of these vertical equilibrium positions, and the point at which equilibrium is reached in both the vertical and horizontal directions is considered as the stable levitation point for the particle with the vertical position regarded as the levitation height.

2.3.2 The influence of EDL on the dependence of crossover frequency upon medium conductivity and particle size

To examine the influence of the EDL on crossover frequency, a 2D axisymmetric model considering the EDL structure is constructed as shown in Fig. 1(d), in which a represents the radius of particle. A thin layer with thickness of t is included for refining the meshes for the space near the surface where the EDL resides. For easy size scaling, the height of the rectangle domain is set at $5(a + t)$ and the width of rectangle domain at $3(a + t)$. The entire bottom edge of the rectangle domain is grounded and a segment of the top edge with width of $(a + t)$ is biased by 5 V. The crossover frequency is determined as the frequency point at which DEP force in z direction changes sign.

To study the medium conductivity effect, KCl is used as the medium electrolyte so the simulation result can be compared with experimental measurements. The limiting molar conductivities of potassium ion and chloride ion are assigned with values of 7.36

$mS \cdot m^2/mol$ and 7.62 $mS \cdot m^2/mol$ respectively (Vanysek 2000). Particles of three different sizes (93 nm, 216 nm and 557 nm in diameter) are considered.

To highlight the differences in considering the influence of EDL, in our model we first assign the particle of a given size a fixed surface charge density at all medium conductivities. In this case we determine the surface charge density through an iterative procedure as described below. With an initially estimated value for the charge density, we first solve Eq. (7) through (9) to find electric field distribution. Then with Eq. (6) we determine the crossover frequency. The obtained crossover frequency is compared with the crossover frequency data shown in Fig. 5(a) in a lower conductivity range ($< 10^{-3}$ S/m). If the two values differ, we adjust the initial estimate for the charge density (e.g., if the obtained frequency is higher, we will reduce the initial value, or vice versa, and repeat process). With the resolved surface charge density, we determine the change of crossover frequency as a function of medium conductivity.

By contrast, we also consider the effect of EDL influenced by surface adsorption of co-ions. In this case, the above resolved charge-density value is used as the initial surface charge density and the surface adsorption effect (discussed in section **2.2.2**) is considered to determine the overall surface charge density for the evaluation of crossover frequency at each medium conductivity. For easy comparison, the particle sizes and medium conductivity are all taken as the same as in experiments (Ermolina and Morgan 2005, Green and Morgan 1999, Wei *et al* 2009).

2.4 Results and discussion

2.4.1 Validation through comparisons

A. Quantification of DEP force

Fig. 2(a) shows the variation of the x component of DEP force with the dielectric property of the particle for our volumetric-integration method, the MST method and the point-dipole method, respectively in 2D models. For all cases, the particle undergoes a transition from nDEP to pDEP when the relative permittivity is 78.5. The force magnitude for the MST method is slightly smaller compared with that for the other two cases. Fig. 2(b) shows the corresponding results in 3D models. All three methods produce identical DEP force magnitude. Fig. 2(c) shows the variation of the DEP force with frequency, in which the force magnitude of the MST method is again smaller than that for the other two cases. The MST method and the volumetric-integration method predict a similar crossover frequency (2.2 MHz) while the point-dipole method yields a slightly lower crossover frequency (1.6 MHz). Similarly, in 3D models all three methods yield almost identical DEP force magnitude (Fig. 2(d)). These results suggest that when particles are homogenous, these three methods predict comparable outcomes. The observed difference in the force magnitude is attributed to the 2D simplification of the actual 3D situations. The DEP force is essentially a volume force and the Maxwell stress tensor is the result of mathematical operation based on Gauss's theorem. In a 2D model, the circular particle is actually a cylinder structure when we consider the third dimension extrusion. Because of this, only the circumferential edges are exposed to medium. This is different from a 3D model in

which the entire outer surface is exposed to medium. Therefore, it is not expected to yield same results when the volume integration is converted to surface integration by Gauss's theorem, leading to the disagreement in results of the two methods. While 2D model provides less accurate estimation of force magnitude, it is often used to simplify the modeling process.

B. Examination of particle-particle interaction

To quantify particle-particle interaction, we examined the results from our volumetric-integration method, the MST method and point-dipole method. In plotting the results, the distance between two particles are non-dimensionalized through division by the radius of particle. The results for particles aligning parallel to electric field in 2D models are shown in Fig. 3(a). The volumetric-integration method and point-dipole method predict a higher force magnitude than the MST method when the two particles are close to each other. The magnitude of attraction force for point-dipole method decays faster than that for the other two methods. When particles align perpendicular to the electric field (see Fig. 3(b)), the repulsion force for both the volumetric-integration method and MST method are much higher than that for the point-dipole method. Since the electric field is highly non-uniform when two particles are close in distance due to the field distortion effect, the point-dipole method appears to generate a much smaller force (4 to 8 times lower) than our volumetric-integration method. On the other hand, the MST method predicts a much higher repulsion force (see data given in the inset table in the figure) when two particles are in

contact. But this force decays to below that for the volumetric-integration method when the particles are more than half-particle distance apart. This is caused by the same reason previously discussed for the single particle case where disagreement in results of volume-integration method and MST method occurs. The difference becomes larger when particle-particle interaction is involved. The 3D model results are shown in Fig. 3(c) (parallel alignment) and Fig. 3(d) (perpendicular alignment). All three methods predict close interaction force magnitude when particles are more than half-particle distance apart. The difference appears when particles get into contact. It is obvious that MST method tends to underestimate the interaction force in parallel alignment and point-dipole method tends to underestimate the interaction force in perpendicular alignment. We also compare the consistency between 2D and 3D models by referring to the force magnitude ratio between the case when particles are in contact and the case when particles are half-particle distance apart. In perpendicular alignment case, volumetric-integration method predicts a ratio around 10 in both 2D and 3D models. The MST method predicts a ratio of 50 in 2D model and 10 in 3D model. These results suggest that volumetric-integration method can appropriately characterize particle-particle interaction in different particle orientations in both 2D and 3D models.

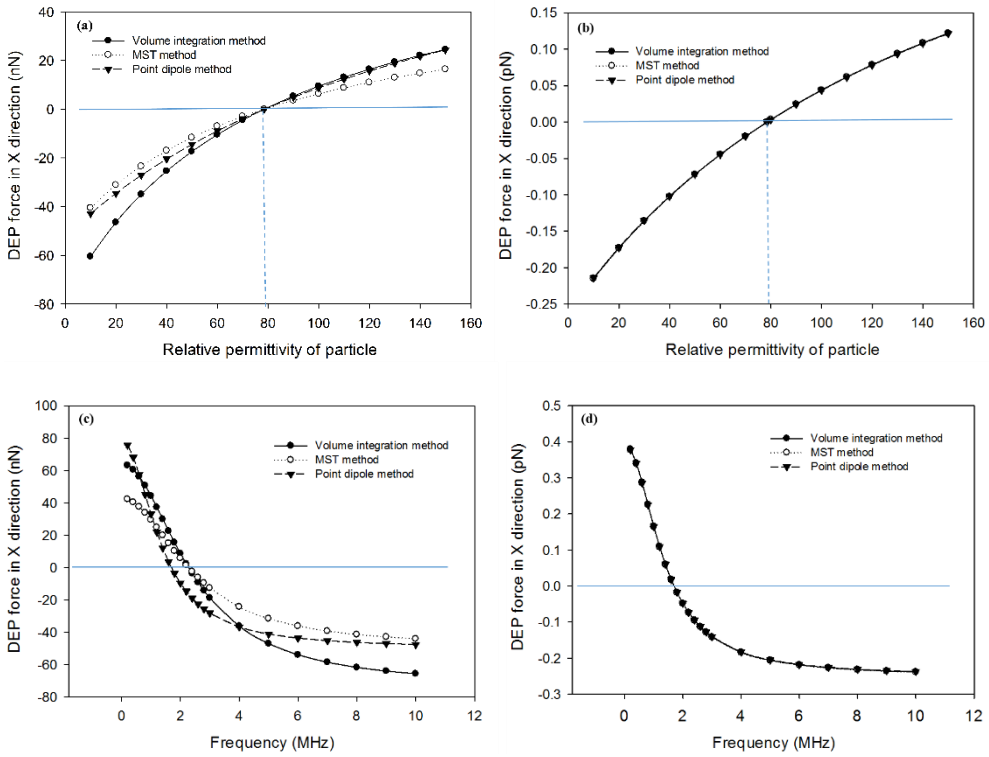

FIG. 2. Results of DEP force determined from three different methods for a single particle: (a) and (b) Variation of DEP force on the single particle with relative permittivity. (c) and (d) Variation of DEP force on the single particle with frequency. (a) and (c) are results from 2D models. (b) and (d) are results from 3D models.

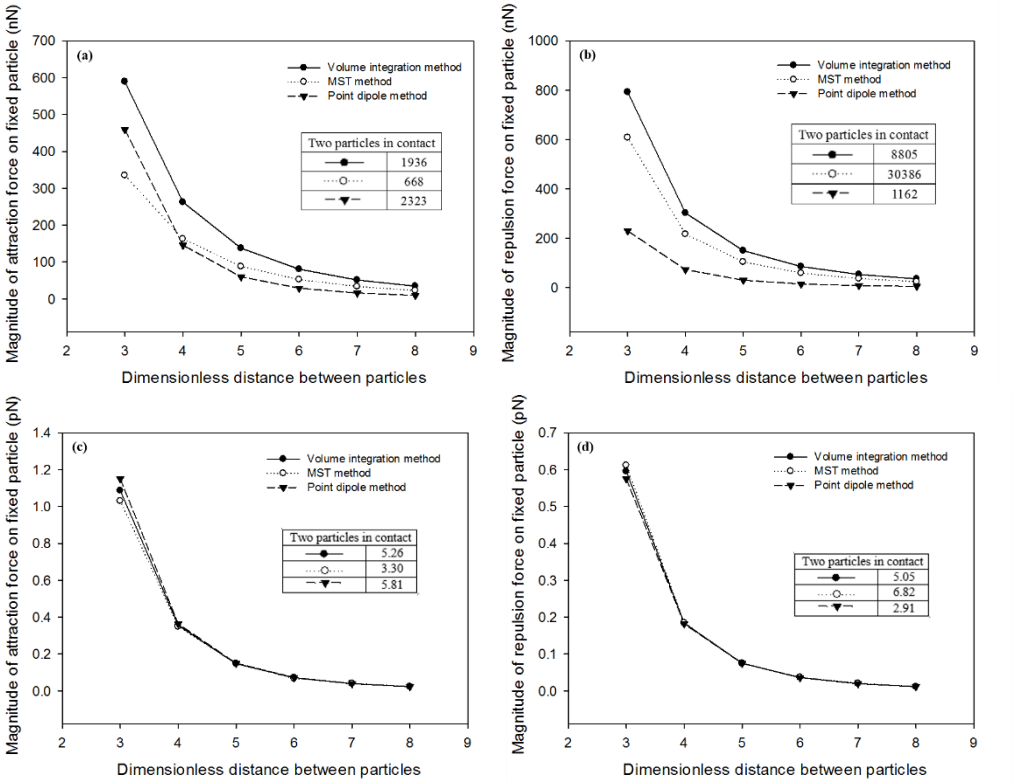

FIG. 3. Results of DEP force determined from three different methods between two particles: (a) and (c) Variation of DEP force between two particles with particle distance when particles are aligned parallel to the electric field. (b) and (d) Variation of DEP force between two particles with particle distance when particles are aligned perpendicular to the electric field. (a) and (b) are results from 2D models. (c) and (d) are results from 3D models.

C. A close look of the crossover behavior of nonhomogenous particles

Table 2 lists the x component DEP force obtained for our volumetric-integration method and the MST method. In comparison, experimental measurement shows that gold coated polystyrene particles experience almost constant pDEP in the frequency range from

10^4 to 10^5 Hz under the given condition listed in Table 1 (García-Sánchez *et al* 2012). Clearly the volumetric-integration method predicts a constant DEP force (~80 nN) close to the value obtained for a homogeneous particle (see Fig. 2(c)), suggesting the results are reasonable. In comparison, the MST method predicts opposite DEP behavior with a force of ~42 μN, which is about 500 times higher in magnitude.

Experimentally, Janus particles are observed (Zhang and Zhu 2010) to exhibit pDEP behavior in the frequency range from 25 kHz to 20 MHz. When a layer of alkanethiol is added atop of the gold part, a crossover frequency is observed around 100 kHz when the medium conductivity is 2 mS/m. The results from our volumetric-integration method show that the Janus particle is always under pDEP in the given frequency range, but with an additional alkanethiol coating layer it exhibits transitional behavior at around 75 kHz, which is close to experimental data (Table 3). The MST method, however, predicts that both types of particles experience nDEP, contradicting with the experimental observation, thus suggesting that it may not be valid for predicting the DEP behavior of non-homogeneous particles. The failure of MST method is attributed to the inappropriate use of Gauss's theorem. In Gauss's theorem, $\iiint_V \left(\nabla \cdot \vec{\boldsymbol{A}}\right) dV = \iint_S \left(\vec{\boldsymbol{A}} \cdot \vec{n}\right) dS$ is only valid when $\vec{\boldsymbol{A}}$ has continuous first order partial derivatives. Due to the non-homogeneous dielectric property inside the particle, the electric field is discontinuous so that the Gauss's theorem is not valid, meaning the MST method is not applicable to non-homogeneous particle.

Table 2. DEP force on gold coated particle

	10^4 Hz	$10^{4.5}$ Hz	10^5 Hz
Volumetric-integration method (nN)	80.04	80.04	80.04
MST method (nN)	-4.24×10^4	-4.24×10^4	-4.23×10^4

Table 3. DEP force on Janus particles

	Volumetric-integration method						
	25 kHz	50 kHz	75 kHz	100 kHz	1 MHz	5 MHz	20 MHz
Janus particle (nN)	27.4	27.4	27.6	27.8	51.7	105	114
Janus particle with alkanethiol layer (nN)	-77.2	-17.3	2.1	10.2	32.1	77.0	97.4
	MST method						
	25 kHz	50 kHz	75 kHz	100 kHz	1 MHz	5 MHz	20 MHz
Janus particle (nN)	-1.23×10^4	-3.40×10^4	-5.08×10^4	-6.04×10^4	-8.02×10^4	-2.76×10^4	-2.95×10^3
Janus particle with alkanethiol layer (nN)	-9.63×10^4	-9.63×10^4	-9.62×10^4	-9.61×10^4	-7.32×10^4	-1.06×10^4	-667

D. A close look of the particle levitation behavior

To assess the accuracy of the DEP force predicted by the volumetric-integration method in real case, a 3D model with the same conditions as in the levitation experiment (Markx *et al* 1997) is analyzed with a surface conductance of 1.2 nS assigned to the particle. For a homogeneous particle placed in an electric field with a dimensional scale much larger than the particle size, the results for the three methods show almost the same levitation height under different conditions (Fig. 4(a) and 4(b)), confirming again that all these methods can be used to quantify the magnitude of DEP force when particles are homogenous. The difference between the simulation and experiment results is possibly attributed to the negligence of the Stokes drag force (Cao *et al* 2008).

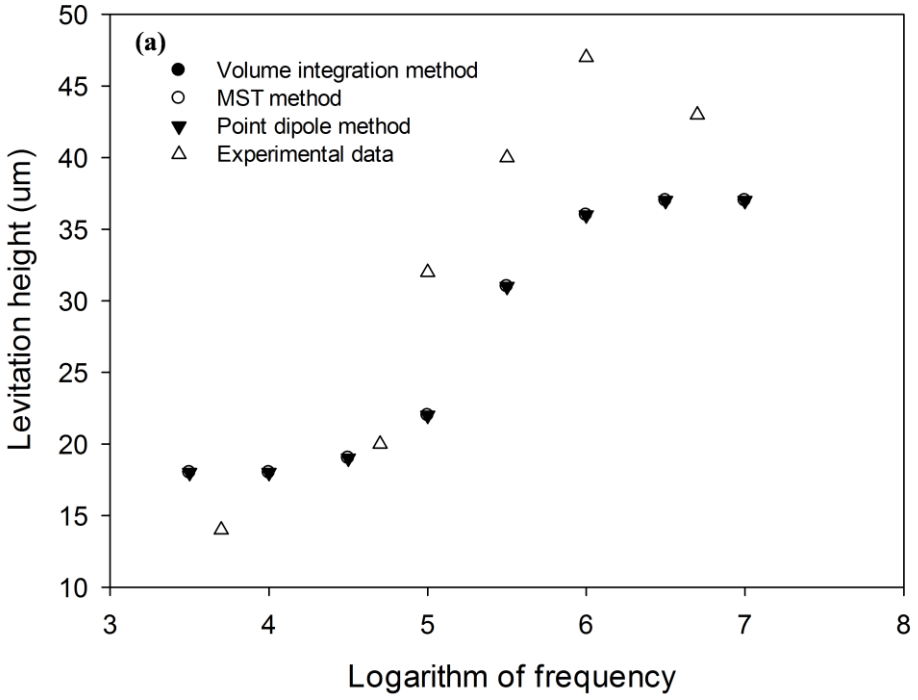
(a)
Volume integration method
MST method
Point dipole method
Experimental data
Levitation height (um)
Logarithm of frequency
50
45
40
35
30
25
20
15
10
3
4
5
6
7
8

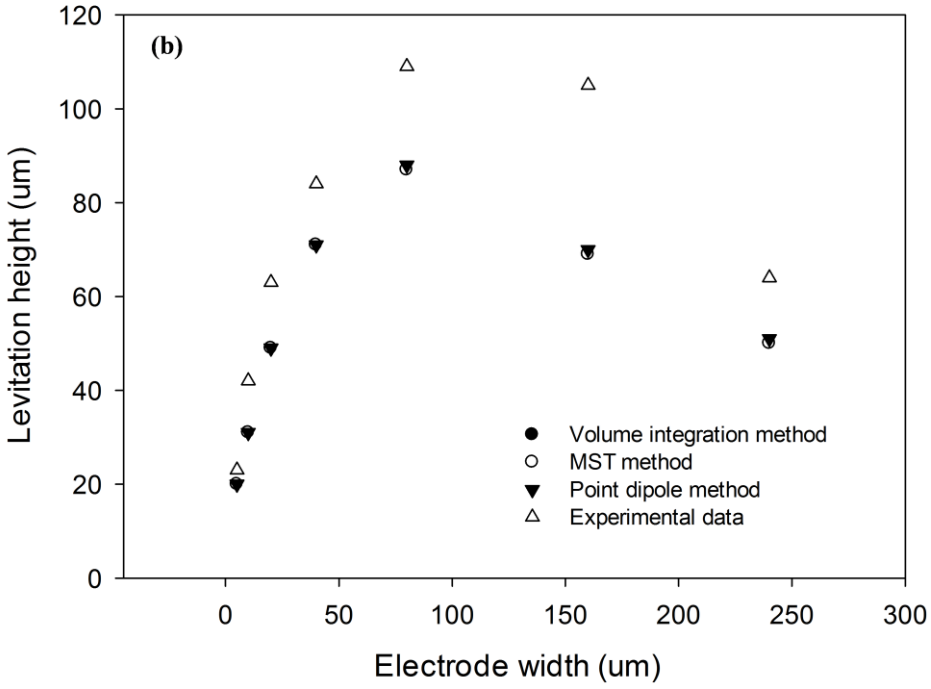
(b)
Volume integration method
MST method
Point dipole method
Experimental data
Levitation height (um)
Electrode width (um)
120
100
80
60
40
20
0
0
50
100
150
200
250
300

FIG. 4. Variation of particle levitation height with (a) frequency and (b) electrode width obtained from three different methods along with experimental measurements.

In above discussion, we only examined the situations of homogeneous spherical particles. However, this volumetric integration method is also applicable to non-spherical particles (e.g., ellipsoidal particles) and non-homogeneous particles (e.g., cells). Due to the space limitation, we would discuss these situations in separate papers.

2.4.2 The influence of EDL on the dependence of crossover frequency upon medium conductivity and particle size

A. Effect of medium conductivity

First, we examine the situation with the assumption of constant surface charge density. With a resolved surface charge density value of -13 mC/m^2, we found that the crossover frequency predicted by our model agrees well with the measurement data for all three sizes of particles only when medium conductivity is low, as shown in Fig. 5(a). As the medium conductivity increases, experimental measurements (Green and Morgan 1999) start to deviate drastically from the modeling results in all cases, suggesting that the assumption of constant surface charge density is questionable when the medium conductivity varies.

Second, we look at the situation in which the EDL structure affected by ionic adsorption is considered with the parameters listed in Table 4, where the value of d and ε_i are taken from literature (He *et al* 2006, Yang and Zhang 2007). Since the value of σ_{max} is unknown and the initial surface charge normally only occupy a small portion of surface area, we assume $\sigma_{max}=10\,\sigma$. Then with $\gamma=e^2$ (for γ is an exponential function of the adsorption Gibbs energy), we found that our results capture almost perfectly the measured data as shown in Fig. 5(b).

Here we compare our approach of modeling EDL with the methods discussed in the three papers by Basuray et. al. (Basuray and Chang 2007, Basuray *et al* 2010, Basuray and Chang 2010). In the 2007 paper (Basuray and Chang 2007), the authors used an analytical approach to determine the impact of EDL on dipole moment by treating the particle as a point dipole. It also argued that the conductance of Stern layer and diffuse layer cannot be directly added to obtain the total surface conductance when the thickness of the diffuse layer is comparable to the size of particle. In this paper, we used integration of polarization density to account for the dipole moment, which allowed us to fully determine the EDL effect by quantifying the distorted electric field distribution inside the particle due to EDL. For the Stern and diffuse layers, we used surface conductance to capture the Stern layer effect because its thickness is always negligible compared with the particle size, but considered the diffuse layer as a separate band region outside the Stern layer having varying conductivity due to charge accumulation. However, regarding ionic adsorption in the Stern layer, while Basuray et. al. related the amount of charge adsorption

to the space charge in diffuse layer in a linear manner, their curve fitting did not seem to consider the effect of the adsorbed charges on the Stern layer conductance. Instead, the conductance of Stern layer was empirically estimated. In our work, we considered surface adsorption as a function of medium conductivity, as observed experimentally (Elimelech and O'Melia 1990). While both results captured the experimental observations very closely, the benefits of our using a numerical approach based on Finite Element Analysis (FEA) include: 1) consideration of the EDL effect can be implemented much easily and with great quantitative accuracy, and 2) the impact of EDL can be related to the underlying physics including the amount of charge adsorbed and Stern layer conductance.

In the other two papers (Basuray *et al* 2010, Basuray and Chang 2010), the authors improved the analytical approach from two aspects. First, the full nonlinear Poisson-Boltzmann equation was solved to replace the Debye-Hückel linearization assumption used in the 2007 paper. Second, different structures of EDL under different conditions were considered. Below a critical bulk electrolyte concentration, a collapsed layer was used to represent the EDL. The thickness and conductivity was independent of the medium conductivity. Beyond this critical bulk electrolyte concentration, the collapsed layer was replaced by an ionic-strength dependent Debye diffuse layer with varying thicknesses. This treatment inherently introduced unrealistic discontinuity in the EDL behavior. In our method, the issue of fully nonlinear limit does not exist as we don't need to use linearization to analytically solve the potential distribution. The Poisson-Boltzmann equation was always expressed in an exponential form. Linearization was only used when we considered the contribution of adsorbed co-ions in the Stern layer because the amount of adsorption is

very low. Due to this advantage, we don't need to estimate the thickness of the diffuse layer and compare it to the Debye length, which is not a precise representation of the EDL structure sometimes. Our modeling approach provided a continuous means to capture the actual EDL behavior. This was made possible by building upon our previous works where we distinctively defined the interface between Stern layer and diffuse layer through consideration of the interior structure of the Stern layer along with the inner and outer Helmholtz plane (Yang and Zhang 2007, 2008).

In summary, above results and discussions suggest that the consideration of the effect of EDL influenced by ionic adsorption in our model allows a much coherent elucidation of the dependence of the crossover frequency upon medium conductivity when incorporated with our volumetric polarization approach.

Table 4. Parameters for dealing with the EDL and surface ionic adsorption (He et al 2006, Yang and Zhang 2007)

Parameter	Value	Physical meaning
σ	-13 mC/m^2	Initial surface charge
σ_{max}	-130 mC/m^2	Maximum amount of charge adsorption
d	0.3 nm	Thickness between iHp and oHp
ε_i	$40\,\varepsilon_0$	Permittivity of the region between iHp and oHp
γ	e^2	intrinsic binding constant

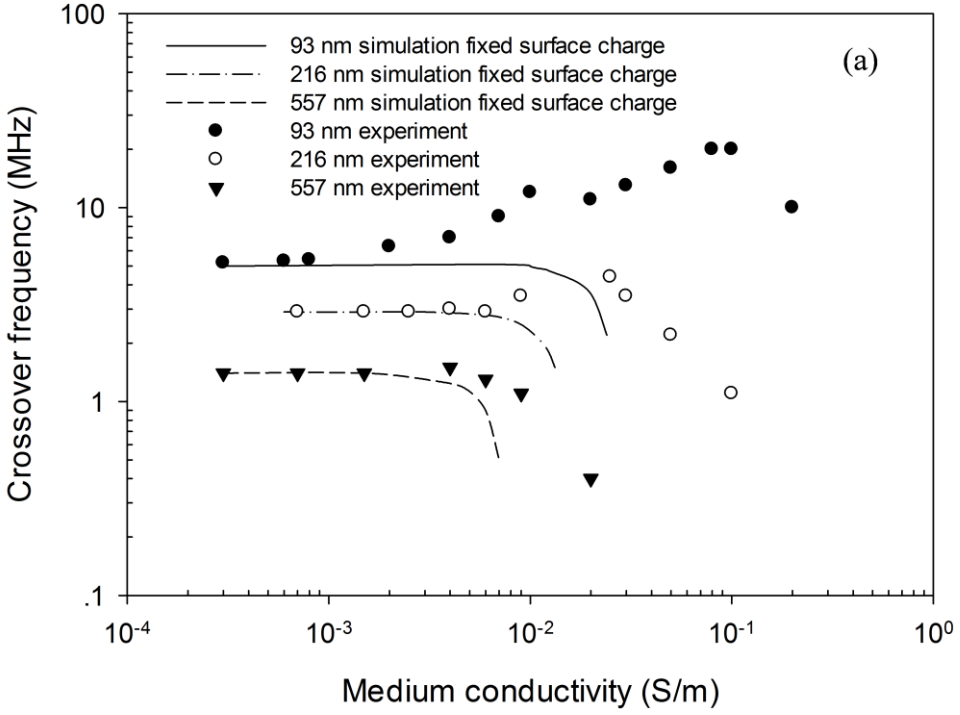
100
10
1
.1
Crossover frequency (MHz)
93 nm simulation fixed surface charge
216 nm simulation fixed surface charge
557 nm simulation fixed surface charge
93 nm experiment
216 nm experiment
557 nm experiment
(a)
10-4
10-3
10-2
10-1
100
Medium conductivity (S/m)

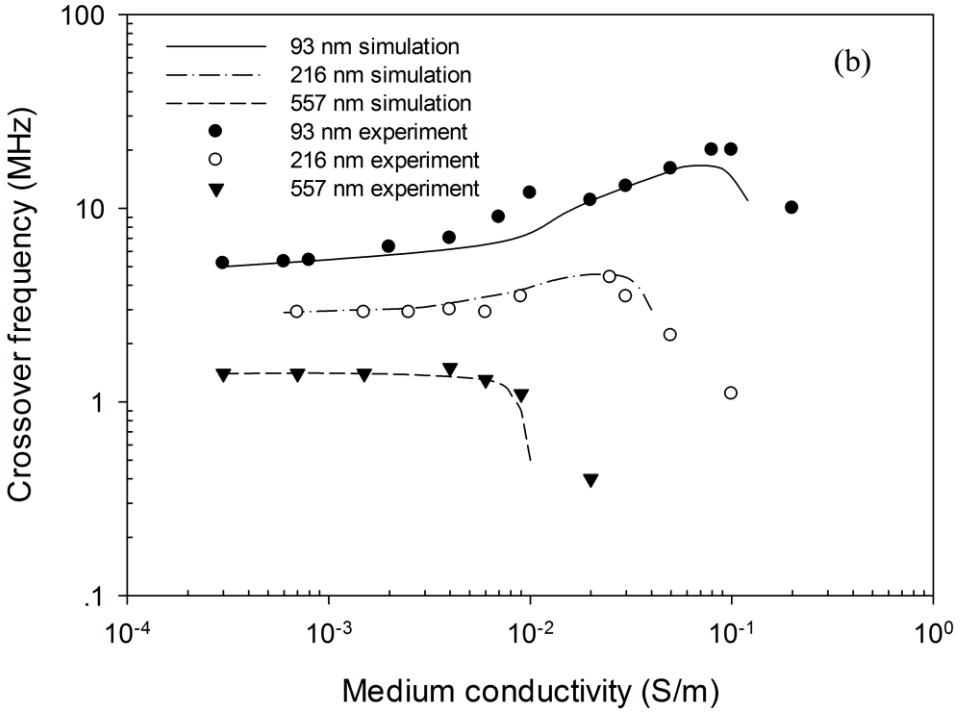
100
10
1
.1
Crossover frequency (MHz)
93 nm simulation
216 nm simulation
557 nm simulation
93 nm experiment
216 nm experiment
557 nm experiment
(b)
10-4
10-3
10-2
10-1
100
Medium conductivity (S/m)

FIG. 5. Variation of crossover frequency with medium conductivity obtained from our volumetric-integration method and experimental measurements for particles of three different sizes when the effect of EDL (a) is considered with fixed surface charge density and (b) is considered with ionic adsorption fully accounted for.

B. Effect of particle size

Fig. 6 shows the variation of crossover frequency as a function of particle size obtained from our volumetric-integration method, along with measurements from Green (1999), Wei (2009) and Ermolina (2005), all obtained at same medium conductivity of 10^{-3} S/m. Overall, our modeling results almost overlap with data from Green and Ermolina's work. In comparison with Wei's measurements, however, our predictions captured the same sudden dropping trend but with slight offset in values. The observed differences between these experiments may be attributed to the differences in particle surface property and in the measurement methods. Nevertheless, these results clearly show that our volumetric-integration method is able to predict the crossover frequency of different sized polystyrene particles with very good agreement with experimental measurements.

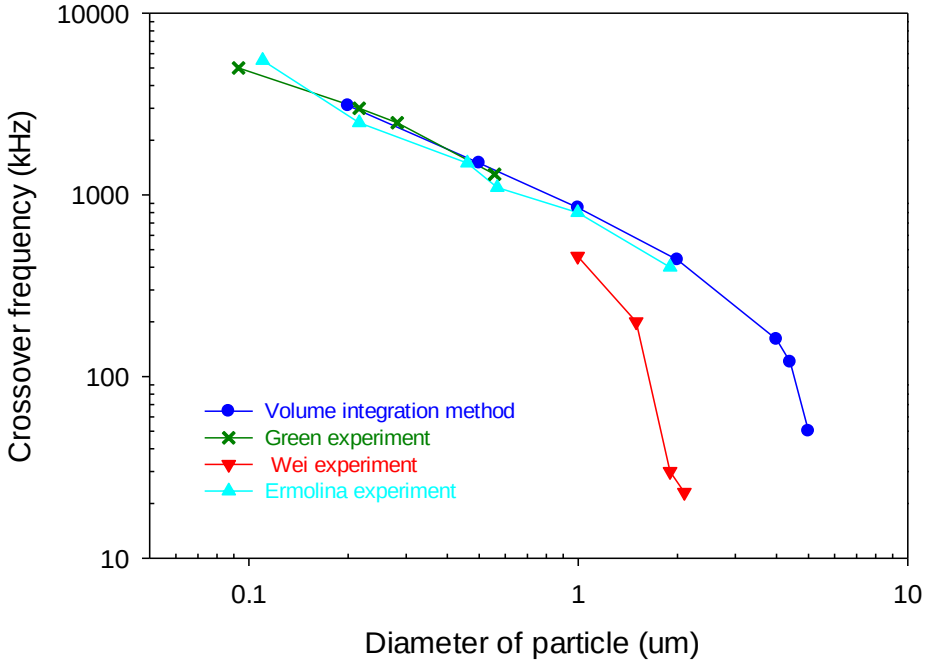

FIG. 6. Variation of crossover frequency with particle size obtained from our volumetric integration method and several experimental measurements.

2.5 Conclusions

We have developed a volumetric integration method assisted by computational modeling to reexamine some of the DEP phenomena and quantify the DEP force such that the effects of particle size, shape, location, particle volumetric polarization, and the influence of EDL structure along with surface adsorption of co-ions are all inherently considered. In comparison with the other methods such as the point-dipole method and the MST method, our results show that our method can predict very well the DEP force and particle-particle interactions of homogenous particles. Moreover, our method is proven

relevant to explaining the crossover behavior of dielectric particles of homogenous and non-homogenous properties, which appears to be a major challenge for other methods including the point-dipole method and the MST method. This work has shed significant new insight into the DEP behavior of particles and provided the basis for elucidating the underlying mechanisms for more complicated DEP phenomena.

Acknowledgements

We appreciate the use of Clemson's Palmetto Cluster computing resources and the support from the Department of Bioengineering and the Institute for Biological Interfaces of Engineering at Clemson University. The funding supported for this work is provide by Tokyo Electron through a research agreement with Clemson University and by the Institute for Biological Interfaces of Engineering at Clemson University.

Reference

Ai, Y., and Qian, S., "DC dielectrophoretic particle–particle interactions and their relative motions," Journal of colloid and interface science 346, 448-454 (2010)

Arnold, W. M., Schwan, H. P., and Zimmermann, U., "Surface conductance and other properties of latex particles measured by electrorotation," Journal of Physical Chemistry 91, 5093-5098 (1987)

Aubry, N., and Singh, P., "Control of electrostatic particle-particle interactions in dielectrophoresis," EPL (Europhysics Letters) 74, 623-629 (2006)

Basuray, S., and Chang, H. C., "Induced dipoles and dielectrophoresis of nanocolloids in electrolytes," Physical Review E 75, 060501 (2007)

Basuray, S., Wei, H. H., and Chang, H. C., "Dynamic double layer effects on ac-induced dipoles of dielectric nanocolloids," Biomicrofluidics, 4, 022801 (2010)

Basuray, S., and Chang, H. C., "Designing a sensitive and quantifiable nanocolloid assay with dielectrophoretic crossover frequencies," Biomicrofluidics, 4, 013205 (2010)

Cao, J., Cheng, P., and Hong, F., "A numerical analysis of force imposed on particles in conventional dielectrophoresis in microchannels with interdigitated electrodes," Journal of Electrostatics 66, 620-626 (2008)

Chau, L. H., Liang, W., Cheung, F. W., Liu, W. K., Li, W. J., Chen, S. C., and Lee, G. B., "Self-rotation of cells in an irrotational AC E-field in an opto-electrokinetics chip," PloS one 8, e51577 (2013)

Church, C., Zhu, J., and Xuan, X., "Negative dielectrophoresis‐based particle separation by size in a serpentine microchannel," Electrophoresis 32, 527-531 (2011)

Elimelech, M., and O'Melia, C. R., "Effect of electrolyte type on the electrophoretic mobility of polystyrene latex colloids," Colloids and Surfaces 44, 165-178 (1990)

Ermolina, I., and Morgan, H., "The electrokinetic properties of latex particles: comparison of electrophoresis and dielectrophoresis," Journal of colloid and interface science 285**,** 419-428 (2005)

García-Sánchez, P., Ren, Y., Arcenegui, J. J., Morgan, H., and Ramos, A., "Alternating current electrokinetic properties of gold-coated microspheres," Langmuir 28, 13861-13870 (2012)

Gascoyne, P. R., Wang, X. B., Huang, Y., and Becker, F. F., "Dielectrophoretic separation of cancer cells from blood," IEEE transactions on industry applications 33, 670-678 (1997)

Green, N. G., and Jones, T. B., "Numerical determination of the effective moments of non-spherical particles," Journal of Physics D: Applied Physics 40, 78-85 (2006)

Green, N. G., and Morgan, H., "Dielectrophoresis of submicrometer latex spheres. 1. Experimental results," The Journal of Physical Chemistry B 103, 41-50 (1999)

He, R., Chen, S., Yang, F., and Wu, B., "Dynamic diffuse double-layer model for the electrochemistry of nanometer-sized electrodes," The Journal of Physical Chemistry B 110, 3262-3270 (2006)

Ho, C. T., Lin, R. Z., Chang, W. Y., Chang, H. Y., and Liu, C. H., "Rapid heterogeneous liver-cell on-chip patterning via the enhanced field-induced dielectrophoresis trap," Lab on a Chip 6, 724-734 (2006)

Ho, C. T., Lin, R. Z., Chen, R. J., Chin, C. K., Gong, S. E., Chang, H. Y., Peng, H. L., Hsu, L., Yew, T. R., Chang, S. F., and Liu, C. H., "Liver-cell patterning lab chip: mimicking the morphology of liver lobule tissue," Lab on a Chip 13, 3578-3587 (2013)

Hossan, M. R., Dillon, R., Roy, A. K., and Dutta, P., "Modeling and simulation of dielectrophoretic particle–particle interactions and assembly," Journal of colloid and interface science 394, 619-627 (2013)

Huang, Y., Holzel, R., Pethig, R., and Wang, X. B., "Differences in the AC electrodynamics of viable and non-viable yeast cells determined through combined dielectrophoresis and electrorotation studies," Physics in medicine and biology 37, 1499-1517 (1992)

Huang, S. B., Wu, M. H., Lin, Y. H., Hsieh, C. H., Yang, C. L., Lin, H. C., Tseng, C. P., and Lee, G. B., "High-purity and label-free isolation of circulating tumor cells (CTCs) in a microfluidic platform by using optically-induced-dielectrophoretic (ODEP) force," Lab on a Chip 13, 1371-1383 (2013)

Hughes, M. P., and Morgan, H., "Dielectrophoretic characterization and separation of antibody-coated submicrometer latex spheres," Analytical Chemistry 71, 3441-3445 (1999)

Hughes, M. P., Morgan, H., and Flynn, M. F., "The dielectrophoretic behavior of submicron latex spheres: influence of surface conductance," Journal of colloid and interface science 220, 454-457 (1999)

Jones, T. B., and Washizu, M., "Multipolar dielectrophoretic and electrorotation theory," Journal of Electrostatics 37, 121-134 (1996a)

Kumar, S., and Hesketh, P. J., "Interpretation of ac dielectrophoretic behavior of tin oxide nanobelts using Maxwell stress tensor approach modeling," Sensors and Actuators B: Chemical 161, 1198-1208 (2012)

Li, M., Li, S., Li, W., Wen, W., and Alici, G., "Continuous manipulation and separation of particles using combined obstacle - and curvature - induced direct current dielectrophoresis," Electrophoresis 34, 952-960 (2013)

Liang, E., Smith, R. L., and Clague, D. S., "Dielectrophoretic manipulation of finite sized species and the importance of the quadrupolar contribution," Physical Review E 70, 066617 (2004)

Lyklema, J., "Fundamentals of interface and colloid science Vol. II: Solid-liquid interfaces," Academic Press, London (1995)

Markx, G. H., Pethig, R., and Rousselet, J., "The dielectrophoretic levitation of latex beads, with reference to field-flow fractionation," Journal of Physics D: Applied Physics 30, 2470-2477 (1997)

O'Konski, C. T., "Electric properties of macromolecules. V. Theory of ionic polarization in polyelectrolytes," The Journal of Physical Chemistry 64, 605-619 (1960)

Pethig, R., "Review article—dielectrophoresis: status of the theory, technology, and applications," Biomicrofluidics 4, 022811 (2010)

Ramón-Azcón, J., Ahadian, S., Obregón, R., Camci-Unal, G., Ostrovidov, S., Hosseini, V., Kaji, H., Ino, K., Shiku, H., Khademhosseini, A., and Matsue, T., "Gelatin methacrylate as a promising hydrogel for 3D microscale organization and proliferation of dielectrophoretically patterned cells," Lab on a Chip 12, 2959-2969 (2012)

Rinaldi, C., and Brenner, H., "Body versus surface force in continuum mechanics: Is the Maxwell stress tensor a physically objective Cauchy stress?" Physical Review E 65, 036615 (2002)

Song, M., Lei, Y., and Sun, H., "Comparison of spherical and non-spherical particles in microchannels under dielectrophoretic force," Microsystem Technologies 21, 381-391 (2015)

Vanysek, P., "Ionic conductivity and diffusion at infinite dilution," CRC handbook of chemistry and physics 83, Boca Raton, FL (2000)

Wang, X. B., Huang, Y., Becker, F. F., and Gascoyne, P. R., "A unified theory of dielectrophoresis and travelling wave dielectrophoresis," Journal of Physics D: Applied Physics 27, 1571-1574 (1994)

Wang, X., Wang, X. B., and Gascoyne, P. R., "General expressions for dielectrophoretic force and electrorotational torque derived using the Maxwell stress tensor method," Journal of electrostatics 39, 277-295 (1997)

Washizu, M., and Jones, T. B., "Generalized multipolar dielectrophoretic force and electrorotational torque calculation," Journal of Electrostatics 38, 199-211 (1996b)

Washizu, M., and Jones, T. B., "Dielectrophoretic interaction of two spherical particles calculated by equivalent multipole-moment method," IEEE Transactions on Industry Applications 32, 233-242 (1996c)

Wei, M. T., Junio, J., and Ou-Yang, H. D., "Direct measurements of the frequency-dependent dielectrophoresis force," Biomicrofluidics 3, 012003 (2009)

Xie, C., Chen, B., Ng, C. O., Zhou, X., and Wu, J., "Numerical study of interactive motion of dielectrophoretic particles," European Journal of Mechanics-B/Fluids 49, 208-216 (2015)

Yang, X., and Zhang, G., "Simulating the structure and effect of the electrical double layer at nanometre electrodes," Nanotechnology 18, 335201 (2007)

Yang, X., and Zhang, G., "The effect of an electrical double layer on the voltammetric performance of nanoscale interdigitated electrodes: a simulation study," Nanotechnology 19, 465504 (2008)

Zellner, P., Shake, T., Sahari, A., Behkam, B., and Agah, M., "Off-chip passivated-electrode, insulator-based dielectrophoresis (OπDEP)," Analytical and bioanalytical chemistry 405, 6657-6666 (2013)

Zhang, L., and Zhu, Y., "Dielectrophoresis of Janus particles under high frequency ac-electric fields," Applied Physics Letters 96, 141902 (2010)

Zhao, Y., Hodge, J., Brcka, J., Faguet, J., Lee, E., and Zhang, G., "Elucidating the mechanism governing the cell rotation behavior under DEP," COMSOL conf. Pro. Boston (2013)

CHAPTER THREE

ELUCIDATING THE MECHANISM GOVERNING THE SELF-ROTATION BEHAVIOR OF CELL UNDER DEP WITH A COMPLETE CELL MODEL

Abstract

Rotating electric field has been used to generate a torque for rotating cells through creating phase lag between dipole moment and electric field. Several published works have reported the self-rotation of cells under normal DEP condition but the underlying mechanism is not well understood. In the authors' experiment of manipulating rat adipose stem cells with parallel interdigitated electrodes under alternating current (AC) DEP, it was observed that apart from the common alignment behavior, some cells constantly rotate in the gap regions between electrodes and the number of rotating cells and the pattern of rotation are dependent upon the frequency of the AC signal. Due to the inability to explain this phenomenon using the current prevailing DEP theory, in this study the authors have incorporated the volumetric-integration method for DEP analysis with a complete cell model to investigate the underlying mechanism for the cell rotation behavior. Our obtained results suggest that the non-uniform dielectric property within a cell and the non-spherical shape of the cell are responsible for the induced cell rotation.

3.1 Introduction

DEP has regained interest in recent years for its promising potential in manipulating cells (Chen *et al* 2014, Hu *et al* 2011, Kimura *et al* 2011, Sen *et al* 2013, Yasukawa *et al* 2012). Works have been done to distinguish and separate different types of cells based on the difference in dielectric property without using cell-specific membrane modification (Ling *et al* 2012, Zhu *et al* 2011). By altering the design of electrodes, cells can also be manipulated to form different patterns to mimic tissues and organs in tissue engineering applications (Ho *et al* 2006, 2013). Other cell behaviors like cell deformation and cell rotation in rotating electric field are also exploited to gain more understanding of the property of cells (Doh *et al* 2012, Gimsa *et al* 1991, Guido *et al* 2011, Sukhorukov *et al* 1998, Yang *et al* 1999). Moreover, the self-rotation behavior of cells in non-rotating electric fields has also been studied (Chau *et al* 2013, Liang *et al* 2015, Ouyang *et al* 2013, Vaillier *et al* 2014, Zhao *et al* 2013). For example, Chau *et al* (2013) observed the rotation behavior through ODEP and experimentally recorded the voltage and frequency response of rotational speed. Ouyang *et al* (2013) induced the rotation of cells which normally does not exhibit self-rotation behavior through ingest of foreign bodies and they concluded that the rotation is generated by uneven distribution of mass inside cell, which also affects the axis of rotation. Vallier *et al* (2014) tried to explain the phenomenon by including the electrothermal effect (ETE). They argued that the rotation is the result of competition between DEP and ETE and self-rotation is augmented around crossover frequency where DEP vanishes. Of all these works, none can quantitatively determine the torque exerted on cell over one rotating cycle or explain the frequency dependent rotation behavior. In this

paper, we introduce a new method to account for cell structures in electric field by considering different components of cells including cell membrane, cytoplasm as well as cell nucleus and present a numerical method to calculate DEP force and torque on each component. Unlike the commonly used shell model, we do not consider the cell a point diploe with an averaged dielectric property. With this new method we are able to predict how frequency affects DEP force exerted on the cell, identify factors affecting cell's crossover frequencies, and explain the mechanism governing self-rotation of a cell and how frequency affects the rotational speed.

3.2 Theoretical development

3.2.1 Conventional method on studying DEP behavior of cell

The conventional expression for the DEP force exerted on a particle with a radius of a immersed in a medium is (Wang *et al* 1994):

$$\vec{F} = 2\pi a^3 \varepsilon_m Re(f\_cm) \nabla E_{rms}^2 \tag{1}$$

where ε_m is the permittivity of the medium and $Re(f\_cm)$ is the real part of Clausius-Mossotti factor (*f_cm*). For a particle with uniform dielectric property, $f\_cm = \frac{\varepsilon_p^* - \varepsilon_m^*}{\varepsilon_p^* + 2\varepsilon_m^*}$ (ε_p is the permittivity of particle, $*$ denotes the permittivity is expressed in complex form $\varepsilon^* = \varepsilon - i\frac{\sigma}{\omega}$). For a biological cell, using the shell model (Gascoyne *et al* 1997), ε_p^* is

replaced with the effective permittivity of the cell. For example, the equation below gives the effective permittivity of a cell composed of two parts: cell membrane and cell cytoplasm.

$$\varepsilon_{eff}^{*} = \frac{\varepsilon_2^{*}[(R_2 / R_1)^3 + 2(\varepsilon_1^{*} - \varepsilon_2^{*}) / (\varepsilon_1^{*} + 2\varepsilon_2^{*})]}{(R_2 / R_1)^3 - (\varepsilon_1^{*} - \varepsilon_2^{*}) / (\varepsilon_1^{*} + 2\varepsilon_2^{*})} \tag{2}$$

ε_1^{*} and ε_2^{*} are the permittivity of cytoplasm and cell membrane, respectively. R_1 and R_2 are the radius of cytoplasm and cell, respectively. Assuming that the cell membrane is completely non-conductive, the analytical expression for predicting the first crossover frequency of the cell can be expressed as:

$$f_{cross} = \frac{\sqrt{2}}{2\pi R_2 C_{mem}} \sigma_m \tag{3}$$

where σ_m is the conductivity of the medium and C_{mem} is the capacitance of the cell membrane.

The limitation of this shell model is that it fails to give information on the DEP force distribution in each component of the cell and that no expression of torque exerted by electric field is available. Moreover, it is based on assumptions such as cells having a spherical shape and interior components. To overcome the limitations, we take advantage of the newly developed numerical way of calculating DEP force based on volumetric integration as discussed in detail as follows.

3.2.2 Volumetric polarization approach for calculating the force and torque on cell

In our previous work (Zhao *et al* 2017), we have developed a volumetric-integration method for quantifying the DEP force. Aside from spherical and homogenous particles, our method is also applicable to irregular shaped particles and particles with non-uniform dielectric property. The force density inside the particle can be expressed as:

$$\vec{\boldsymbol{f}} = (\vec{\boldsymbol{P}} \cdot \nabla)\vec{\boldsymbol{E}} = (3\varepsilon_m(\vec{\boldsymbol{E}} \text{-} \vec{\boldsymbol{E}}_{particle}) \cdot \nabla)\vec{\boldsymbol{E}} \tag{4}$$

where $\vec{\boldsymbol{E}}$ is the original electric field, $\vec{\boldsymbol{E}}_{particle}$ is the electric field after distortion by the presence of particle and $\vec{\boldsymbol{P}}$ is the polarization at the given point. To obtain the DEP force on either the whole cell or a cell component, the force density is integrated over the domain of interest:

$$\vec{\boldsymbol{F}} = \iiint (3\varepsilon_m(\vec{\boldsymbol{E}} \text{-} \vec{\boldsymbol{E}}_{particle}) \cdot \nabla)\vec{\boldsymbol{E}} \mathrm{d}V \tag{5}$$

To obtain the torque exerted by the electric field, we take a similar approach by calculating the torque density. By considering a spherical infinitesimal unit inside the particle placed in electric field as a dipole composed of two point charges with opposite polarity (Q and $-Q$) separated by a distance of d (d is the diameter of the spherical particle unit), the torque on the particle unit can be derived as:

$$\begin{aligned} \vec{\boldsymbol{t}} &= \vec{\boldsymbol{r}}_+ \times (Q\vec{\boldsymbol{E}}_+) + \vec{\boldsymbol{r}}_- \times (-Q\vec{\boldsymbol{E}}_-) = Q(\vec{\boldsymbol{r}}_+ \times (\vec{\boldsymbol{E}} + \frac{(\nabla \cdot \vec{\boldsymbol{E}})\vec{\boldsymbol{d}}}{2}) - \vec{\boldsymbol{r}}_- \times (\vec{\boldsymbol{E}} - \frac{(\nabla \cdot \vec{\boldsymbol{E}})\vec{\boldsymbol{d}}}{2})) \\ &= Q((\vec{\boldsymbol{r}}_+ - \vec{\boldsymbol{r}}_-) \times \vec{\boldsymbol{E}} + (\vec{\boldsymbol{r}}_+ - \vec{\boldsymbol{r}}_-) \times \frac{(\nabla \cdot \vec{\boldsymbol{E}})\vec{\boldsymbol{d}}}{2}) = Q\vec{\boldsymbol{d}} \times \vec{\boldsymbol{E}} + Q\vec{\boldsymbol{d}} \frac{(\nabla \cdot \vec{\boldsymbol{E}})\vec{\boldsymbol{d}}}{2} = \mathrm{d}\vec{\boldsymbol{m}} \times \vec{\boldsymbol{E}} \\ &= \vec{\boldsymbol{P}} \times \vec{\boldsymbol{E}} \mathrm{d}V = 3\varepsilon_m(\vec{\boldsymbol{E}} - \vec{\boldsymbol{E}}_{particle}) \times \vec{\boldsymbol{E}} \mathrm{d}V \end{aligned} \tag{6}$$

where $\vec{r}_+$ and $\vec{r}_-$ are the vectors from a random point to the positive and negative point charges and $\vec{\boldsymbol{d}}$ is a vector pointing from the negative point charge to positive point charge. $\vec{\boldsymbol{E}}_+$ and $\vec{\boldsymbol{E}}_-$ are the electric field at the positive and negative point charges. d$\vec{\boldsymbol{m}}$ is the dipole moment of the particle unit. The net torque exerted by electric field on the whole cell or certain cell component can also be expressed in an integration form as:

$$\vec{\boldsymbol{T}} = \oiiint 3\varepsilon_m(\vec{\boldsymbol{E}} - \vec{\boldsymbol{E}}_{particle}) \times \vec{\boldsymbol{E}} \mathrm{d}V \tag{7}$$

It is worth noting that the torque is not obtained by integrating the cross product of arm and force density. In studying the movement of particles using the MST method, others have quantified the torque exerted on a particle by integrating the cross product of arm and surface stress (Ai and Qian 2010, Ai *et al* 2014, House *et al* 2012). As we already pointed out that the DEP force is, in essence, a volume force, this approach will yield incorrect prediction of the rotational movement of particle. If we select the axis of rotation and integrate the cross product of arm and force density over the volumetric domain of the cell, another expression of torque can be obtained as shown below:

$$\vec{\boldsymbol{T}} = \oiiint \vec{\boldsymbol{r}} \times (3\varepsilon_m(\vec{\boldsymbol{E}} \text{-} \vec{\boldsymbol{E}}_{particle}) \cdot \nabla) \vec{\boldsymbol{E}} \mathrm{d}V \tag{8}$$

where $\vec{\boldsymbol{r}}$ is the distance vector to the axis of rotation. In the Results and discussion Section, we will compare the torque value obtained from Eq. (7) and (8) and discuss the limitation of Eq. (8). With the volumetric-integration method, we can also examine the crossover frequency and elucidate the governing mechanism for self-rotating cells.

3.3 Experiment setup and computational implementation

3.3.1 Experimental setup

Rat adipose stem cells in a culture medium are centrifuged and the cells are resuspended in low conductivity medium (0.3% glucose and 8.5% sucrose). The centrifuge process is repeated three times with the medium replaced each time. Interdigitated electrodes are fabricated using conventional photolithographic processes on gold coated glass slides. A polyethylene sheet of 12 μm thick is used as a cover to insulate the electrodes. A liquid well is formed atop the insulation layer with equal-height spacers on all sides as walls. Cells suspended in the low conductivity medium are injected into the well during experiment. For electric biasing, an AC potential signal is applied to the two sets of interdigitated electrodes, one electrically biased and one grounded. The AC signal is generated by a waveform generator (WGF600; FLC Electronics Inc., Sweden). All optical images and videos are recorded with an inverse optical microscope (Axiovert s100; Zeiss, Germany).

3.3.2 Computational implementation

To quantify the DEP force and the corresponding torque on the cell, we developed 2D and 3D models using COMSOL Multiphysics software (version 4.4). The 2D models are developed to validate the new method and the 3D models are to quantify the magnitude of torques experienced by cells in experiments. The electric fields with and without the presence of a cell are simultaneously solved using electric current module with frequency

domain study. Because different models are developed for different purposes, for the sake of easy discussion we will leave the rest of modeling details in the results and discussion section as we discuss each individual situation case by case.

3.4 Results and discussion

3.4.1 Experimental observation

Our experimental observations show that when DEP force is exerted on rat adipose stem cells, some of the cells start to rotate. In Fig. 1(a) and (b), the circled cells keep rotating when an AC signal of 200 Vpp at 300 kHz is applied to the interdigitated electrodes. The direction of cell rotation is marked by red circles as rotating counter-clockwise and by green circles as clockwise. We repeated the experiment with a larger population of cells in which all rotating cells are circled out in Fig. 1(c) and (d). At a lower frequency (5 MHz), few cells can sustain constant rotation, but when the frequency reaches 20 MHz, more cells and cell agglomerates start to rotate. For some cells, the rotation is so fast that the chain structure is no longer present. We also noted that all rotating cells will rotate about the axis perpendicular to electrode plane at low frequency. But a few cells rotate about the axis parallel to the edge of electrode at high frequency (marked by green circles). The movies showing the rotation process are provided in supplemental material.

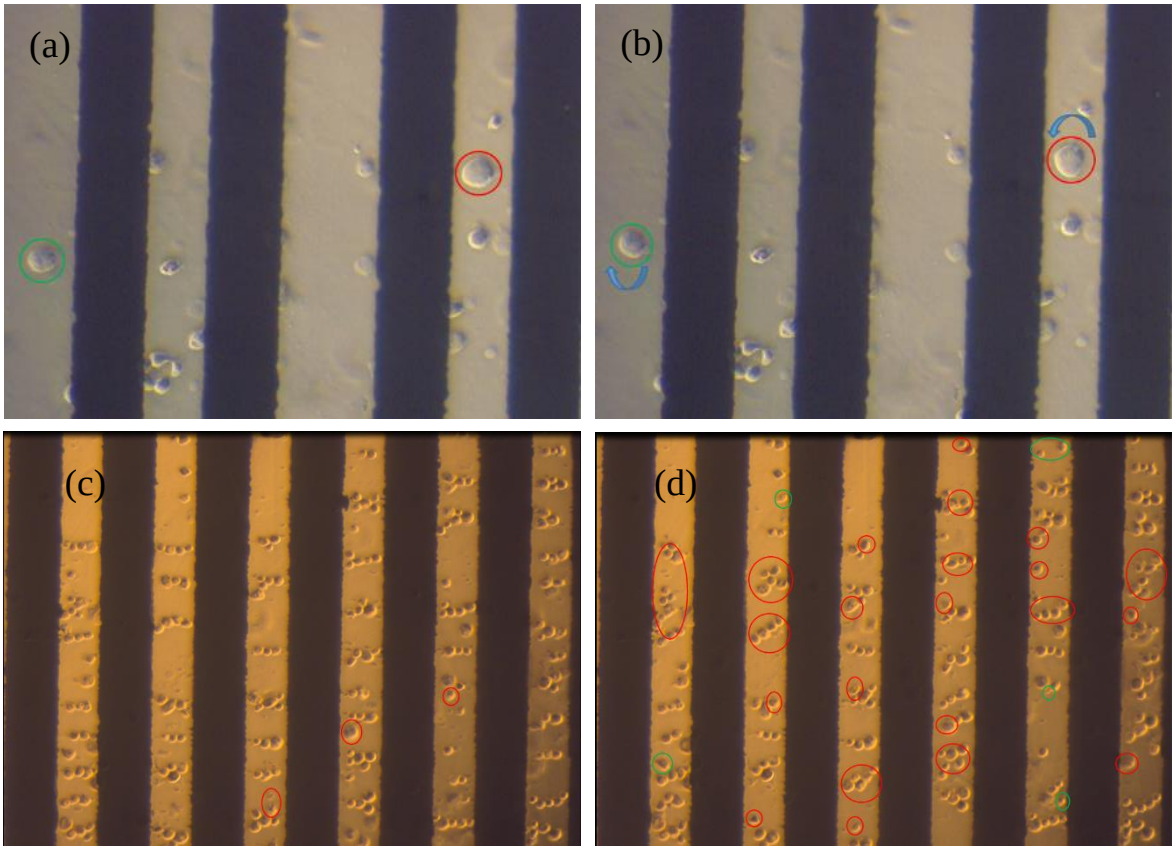

FIG. 1. Rat adipose stem cells rotate in the gap regions between interdigitated electrodes. (a) Initial orientation of cells. (b) Orientation of cells after 1 second under 300 kHz, 200 V peak to peak signal. The direction of rotation is marked by arrow. (c)-(d) Rat adipose stem cells rotate under 32V peak to peak signal. Rotating cells are marked by circles (Red circles indicate cells rotate about axis perpendicular to electrode plane and green circles indicate cells rotate about axis parallel to the edge of electrode). (c): Cells rotate at 5 MHz. (d): Cells rotate at 20 MHz.

3.4.2 Validation of volumetric-integration method

To explain the frequency-dependent behavior of a cell with consideration of sufficient cell internal structures but without demanding excessive computational power, we created a 2D cell model using COMSOL with the geometry shown in Fig. 2(a). The third dimension is assigned a unity in size (1 m in SI units). The cell is placed in the center of a square domain, surrounded by medium whose conductivity can be adjusted. The middle part of right edge (10 μm length) is grounded and the left edge is biased by 10V. Under this biasing setup, the field on right side is stronger than the field on left side, meaning cells will move to the right edge under pDEP and to the left edge under nDEP. We first consider a simplified cell model: a spherical cell with uniform cytoplasm (nucleus is neglected) with a radius of 5 μm and the thickness for cell membrane of 6 nm. The permittivity of medium, cell membrane and cytoplasm are 78.5, 10, and 60, respectively. Under this condition the cell membrane capacitance is calculated to be 1.48×10^{-2} F/m^2, which is within the normal range. The conductivity of medium is set to be 0.1 S/m and the conductivity of cytoplasm is 0.2 S/m. Because the main component of cell membrane is a compact lipid bilayer, its conductivity is very low (ion channels will only contribute to the weak conductivity). In our model, the membrane conductivity is set to 0 S/m to essentially neglect the influence of cell membrane conductance. By distinguishing different components of cell instead of treating the cell as having uniform dielectric property, we calculate the DEP force on the cell over the frequency range from 10 kHz to 20 MHz, with this range the DEP force is found to change in sign at around 250 kHz which is regarded as the crossover frequency as shown in Fig. 2(b).

Because crossover frequency is the most frequently used metric for distinguishing or separating different types of cells with the DEP technique, we further investigate possible factors that affect the crossover frequency, including capacitance and resistance of cell membrane, conductivity of cytoplasm, conductivity of medium and cell size.

a. Capacitance and resistance of cell membrane

Given the fact that thickness of the cell membrane does not change much, the capacitance per unit area is determined by the permittivity of the cell membrane. When the conductivity of cell membrane is assumed to be very small, say 0 S/m, we found an inverse linear relationship between crossover frequency and cell membrane permittivity as plotted in Fig. 2(c). This supports the fact that surface modification is sometimes done to alter the membrane permittivity so that cell separation can be achieved by crossover frequency for different types of cells (Gagnon *et al* 2008).

The effect of cell membrane conductivity on crossover frequency is further examined and shown in Fig. 2(d). Clearly, when the conductivity reaches a certain value and beyond, the DEP force will always be positive (pDEP), suggesting there will be no crossover when the frequency reduces. This prediction is consistent with the observation that dead cells experience pDEP even at very low frequency (Jen and Chen 2009) because the membrane conductivity of viable cells is much lower than that of non-viable cells due to more compact membrane structure (Talary *et al* 1996).

b. Conductivity of cytoplasm and medium

In terms of the effect of cytoplasm conductivity on crossover frequency, which is shown again in Fig. 2(c), we see almost no change in crossover frequency when the conductivity increases from 0.25 S/m to 0.4 S/m, indicating that cytoplasm conductivity has little effect on crossover frequency. This may explain why breast cancer cells and normal breast cells exhibit similar crossover frequency as observed in our experiments as shown Fig. 2(e)-(h). This behavior is also observed by An *et al* (2009) where they argued that the main difference between these two types of cells lies in the cytoplasm conductivity. To separate these types of cells, they applied a much higher frequency, close to a value that is commonly known as the second crossover frequency (to be discussed more later). Fig. 2(c) also shows that our model predicts that medium conductivity is linearly related with crossover frequency.

c. Cell size

Although Fig. 2(c) predicts an inversely proportional relationship between crossover frequency and cell radius, this relationship is rarely used to separate cells because cells in a population often vary in sizes. For this reason, cells of different sizes are often separated by the difference in DEP force magnitude (Kang *et al* 2008).

From above discussion, we confirm that those factors affect the first crossover frequency of cell in the same way as predicted by the analytical expression in Eq. (3), which validates the effectiveness of the volumetric-integration method.

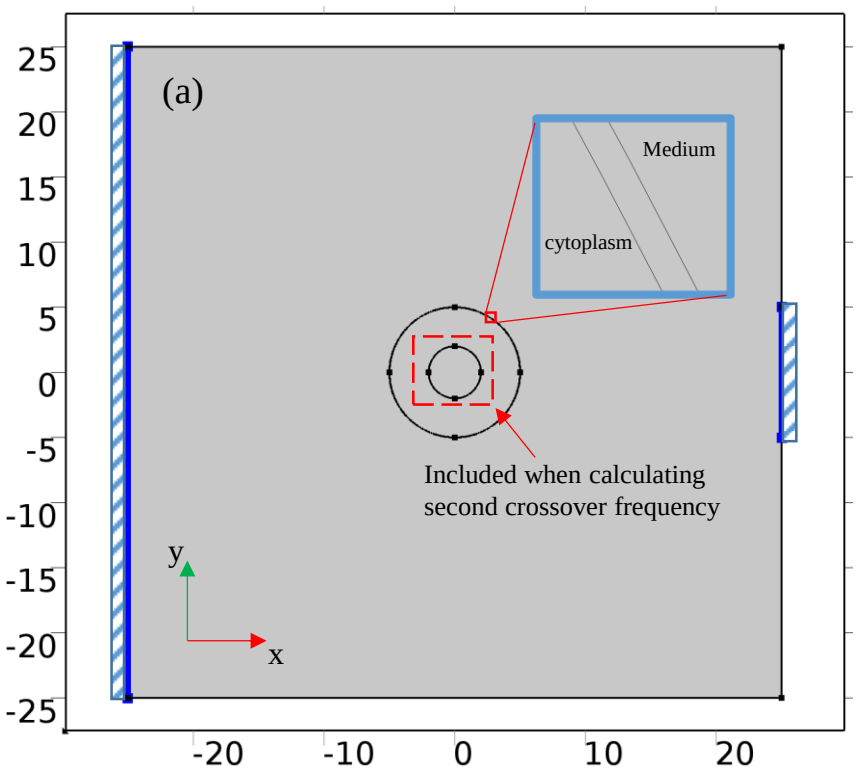
(a)
Medium
cytoplasm
Included when calculating
second crossover frequency
y
x
25
20
15
10
5
0
-5
-10
-15
-20
-25
-20
-10
0
10
20

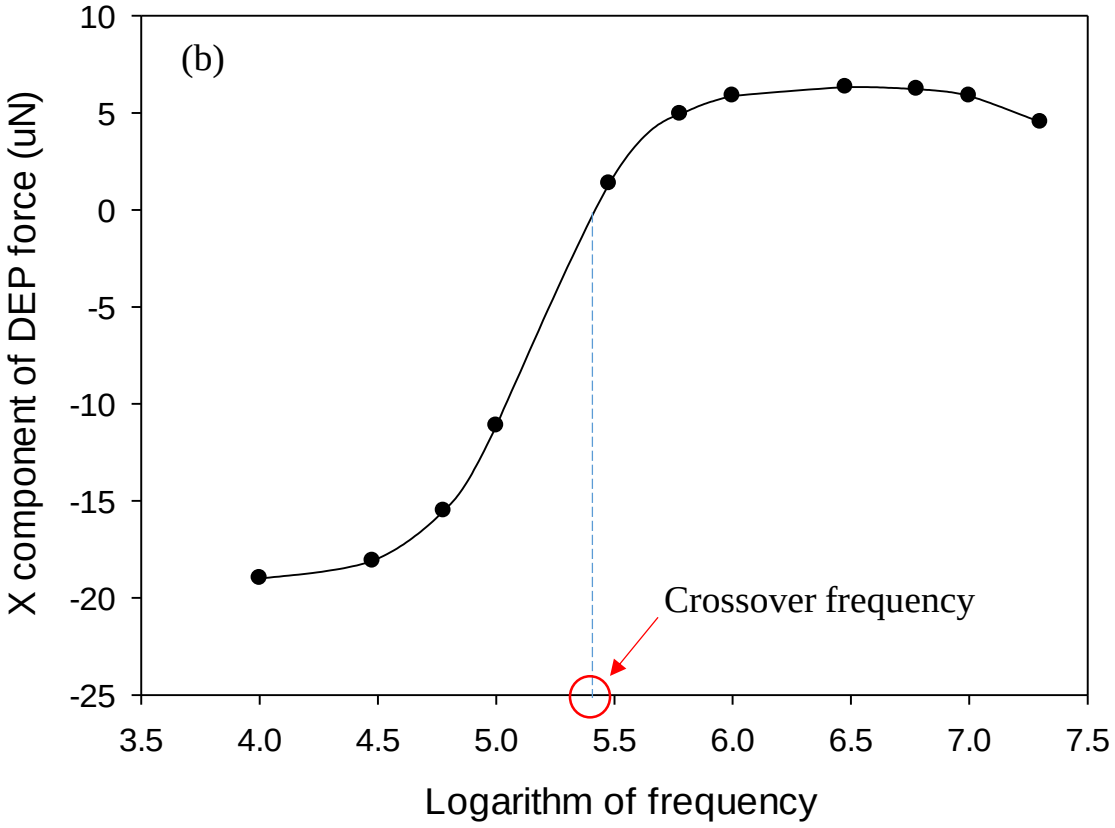
(b)
X component of DEP force (uN)
10
5
0
-5
-10
-15
-20
-25
3.5
4.0
4.5
5.0
5.5
6.0
6.5
7.0
7.5
Logarithm of frequency
Crossover frequency

(c)

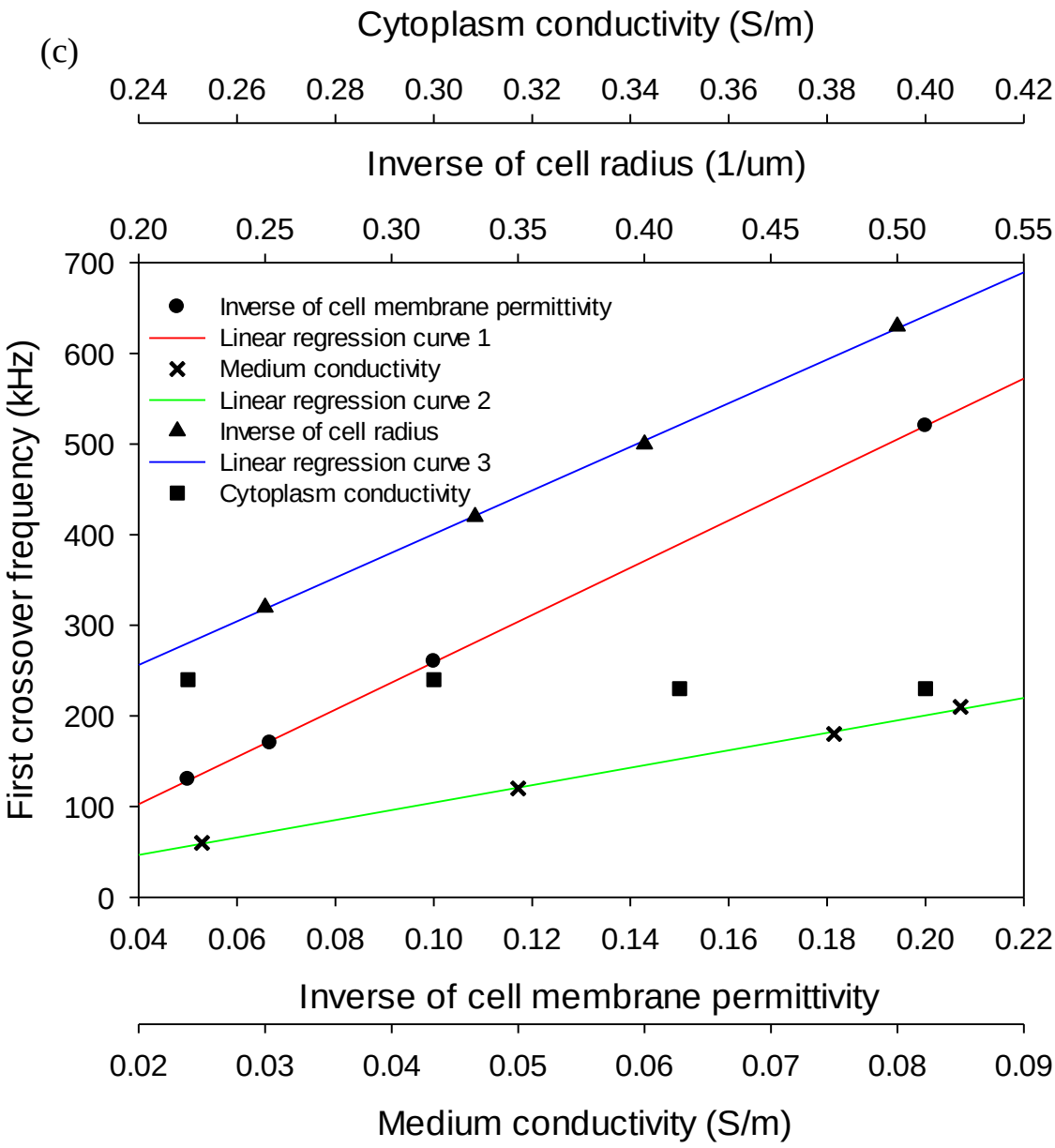
Cytoplasm conductivity (S/m)
0.24 0.26 0.28 0.30 0.32 0.34 0.36 0.38 0.40 0.42
Inverse of cell radius (1/um)
0.20 0.25 0.30 0.35 0.40 0.45 0.50 0.55
First crossover frequency (kHz)
0 100 200 300 400 500 600 700
Inverse of cell membrane permittivity
Linear regression curve 1
Medium conductivity
Linear regression curve 2
Inverse of cell radius
Linear regression curve 3
Cytoplasm conductivity
0.04 0.06 0.08 0.10 0.12 0.14 0.16 0.18 0.20 0.22
Inverse of cell membrane permittivity
0.02 0.03 0.04 0.05 0.06 0.07 0.08 0.09
Medium conductivity (S/m)

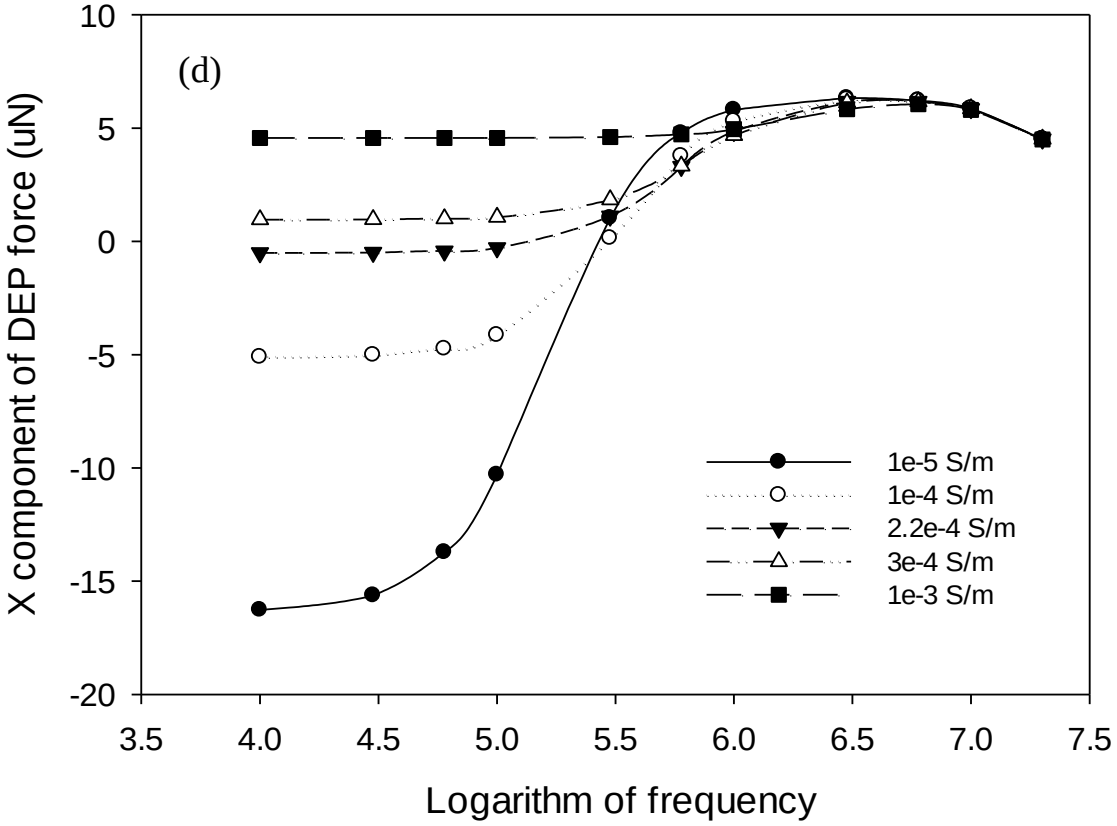
(d)
X component of DEP force (uN)
Logarithm of frequency
10
5
0
-5
-10
-15
-20
3.5
4.0
4.5
5.0
5.5
6.0
6.5
7.0
7.5
1e-5 S/m
1e-4 S/m
2.2e-4 S/m
3e-4 S/m
1e-3 S/m

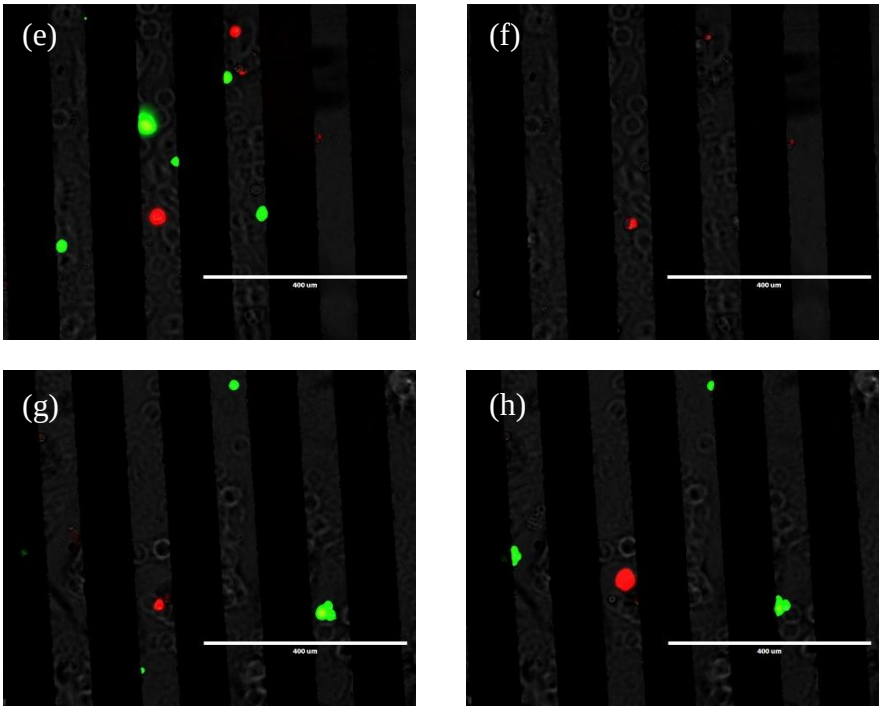
(e)
400 um
(f)
400 um
(g)
400 um
(h)
400 um

FIG. 2 (a) Geometry of the 2D model for quantifying DEP force and crossover frequency of cell. (b) Frequency response of DEP force shows a transition around 250 kHz. (c) Inverse linear relationship between permittivity of cell membrane and crossover frequency; Inverse linear relationship between cell radius and crossover frequency; Linear relationship between medium conductivity and crossover frequency; the cytoplasm conductivity has minor impact on crossover frequency. (d) Frequency response of DEP force on cell with different cell membrane conductivity. When the membrane conductivity reaches 3×10-4 S/m, the crossover frequency vanishes. (e) to (h) Frequency response of breast cancer cell (green) and normal breast cell (red). (e) A group of mixed cells, no voltage applied. (f) 350 KHz, 20 Vpp signal. Both types of cells lift up under nDEP. (g) Another group of cells, no voltage applied. (h) 450 kHz, 20 Vpp signal. Both types of cells are attracted to the edge of electrode under pDEP.

A cell has much more complex structures other than cell membrane and uniform cytoplasm. Of all inner cell organelles, cell nucleus differs most in dielectric property in most occasions. To enable our model to predict cell behavior, we expand it by including a cell nucleus with nuclear envelope (shown in Fig. 2(a)). The cell nucleoplasm normally has a higher conductivity than cytoplasm and the nuclear envelope is more conductive than cell membrane because of the existence of nuclear pores. The thickness of nuclear envelope is set at 40 nm and the conductivity is set at 10^{-3} S/m.

When frequency is increased, often to the range of several tens of MHz, a second transition in the sign of the DEP force will occur, and the frequency that marks this second transition is called the second crossover frequency. We next investigate the possible factors

affecting the second crossover frequency including cytoplasm conductivity, nucleus conductivity and the ratio of nucleus radius to cell radius.

a. Cell conductivity effect

Fig. 3 shows that both cytoplasm conductivity and nucleoplasm conductivity exhibit linear relationships with second crossover frequency. The higher the conductivity the higher the second crossover frequency owing to dominating contribution of conductivity in the effective permittivity at higher frequency, which causes a right shift in the second crossover frequency.

b. Ratio of nucleus radius to cell radius

Fig. 3 also shows that there exists a quadratic relationship between nucleus-to-cell ratio and the second crossover frequency. Note that given the fact results given here are from a 2D model, when applying this result to a 3D real situation, the ratio considered should be a volumetric one instead of area one, hence a cubic relationship may be expected.

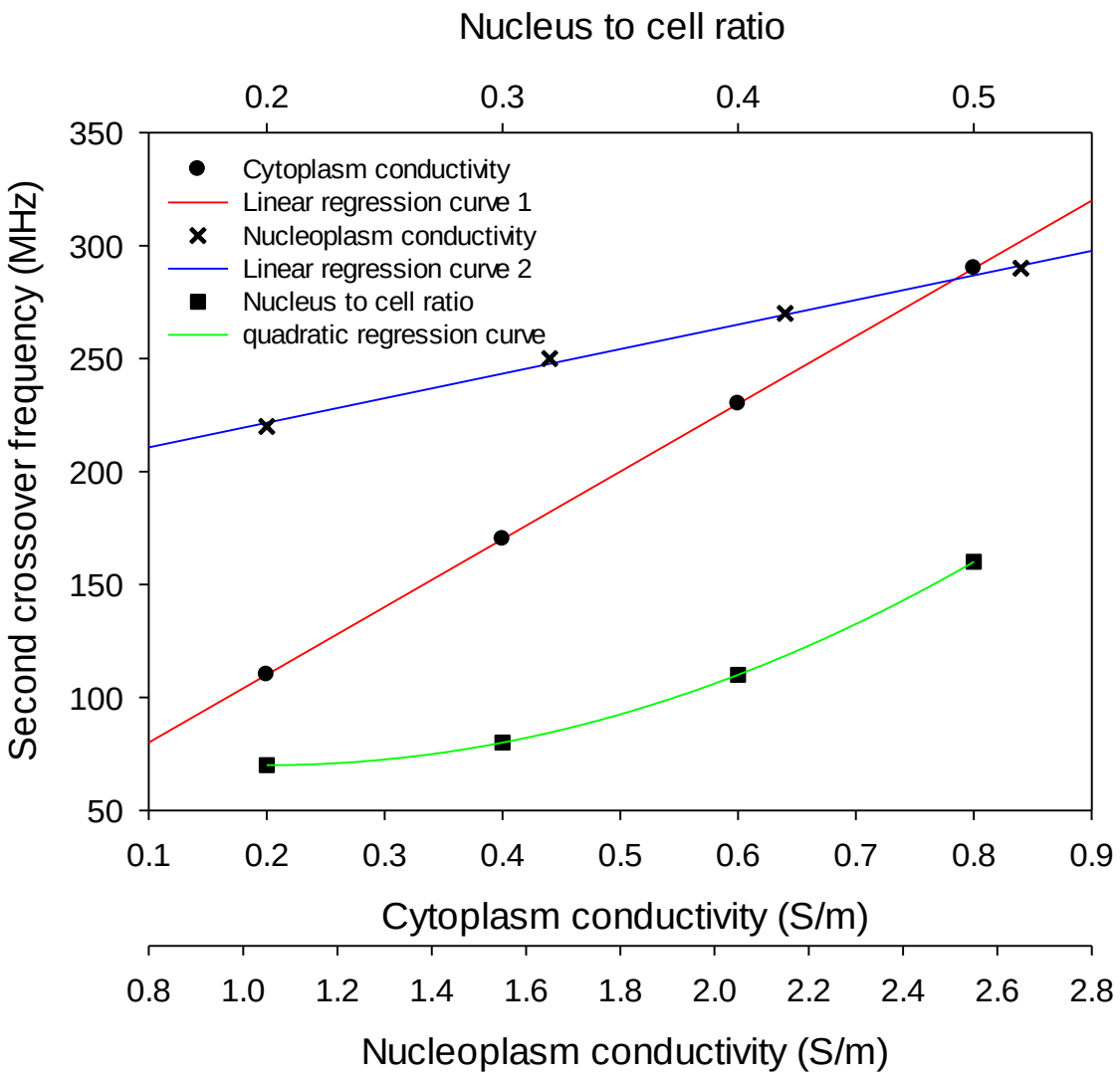

FIG. 3. The second crossover frequency is proportional to cytoplasm conductivity and nucleoplasm conductivity. The second crossover frequency is proportional to the volume ratio of nucleus to cell.

The discussion on second crossover frequency of cell also confirms the validity of the volumetric-integration method (Pethig *et al* 2010), which provides the basis for applying the new method to explain the cell rotation behavior.

To quantify the torque exerted on cells, a 2D model is built. Different from the model for quantifying the DEP force, only the middle part of left side (10 μm length) is biased to create a symmetrical non-uniform electric field as shown in Fig. 4(a). To investigate the difference between two expressions for torque calculation (Eq. (7) and (8)), we use an ellipsoidal particle with axis lengths of 14 μm and 10 μm, respectively, to represent the cell. To simplify the problem, the complex structure of cell components is neglected in this case. Both the cell and medium are treated as pure dielectric material with zero conductivity and relative permittivity at 60 and 78.5, respectively. The cell is initially aligned with its major axis perpendicular to the electrode and then parametrically rotated about its geometric center counterclockwise by 15° incrementally. Fig. 4(b) shows the torque calculated from the two expressions over a full rotational span of 360°. Clearly, both expressions predict four orientations at which the torque is zero: 0°, 90°, 180° and 270°. For the curve based on Eq. (7), when the cell is oriented at 90° or 270°, it is not stable because a small increase in angular orientation will generate a positive torque, which will force the cell to rotate counter-clockwise and favor a continuous deviation, meaning the cell tends to align with the major axis perpendicular to the electrode. On the other hand, the curve based on Eq. (8) shows that the cell will align with the major axis parallel to the electrodes as it is not stable when oriented at 0° and 180°. Experimentally particles under nDEP are observed (Mittal and Furst 2009, Singh *et al* 2009) to align with the major axis along the direction of electric field, suggesting that Eq. (8) is not a valid expression for torque calculation. For this reason, torques exerting on cells are obtained using Eq. (7).

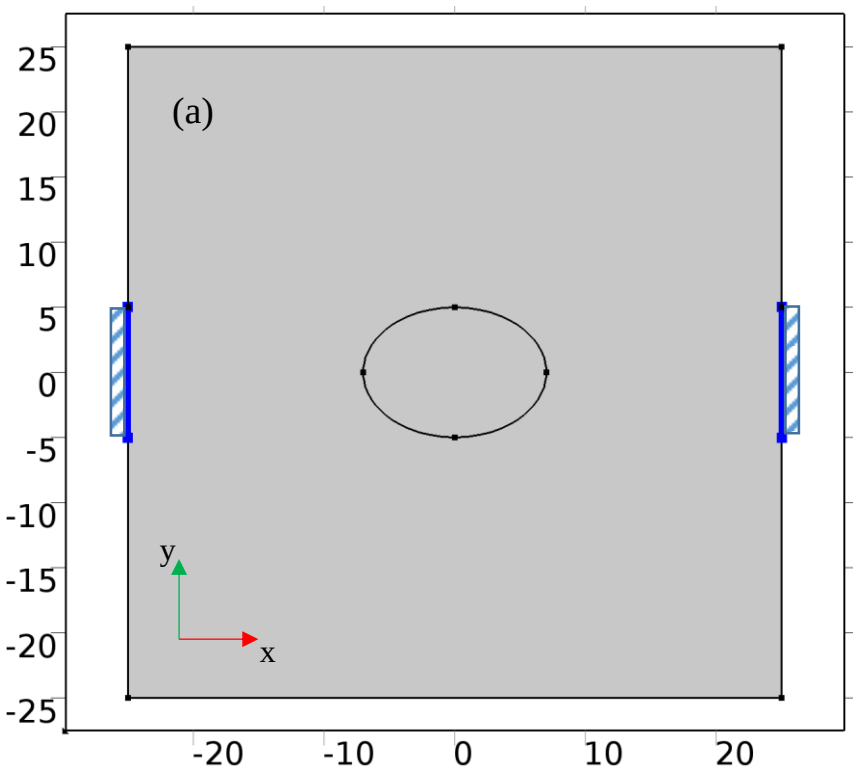
(a)
25
20
15
10
5
0
-5
-10
-15
-20
-25
-20
-10
0
10
20
y
x

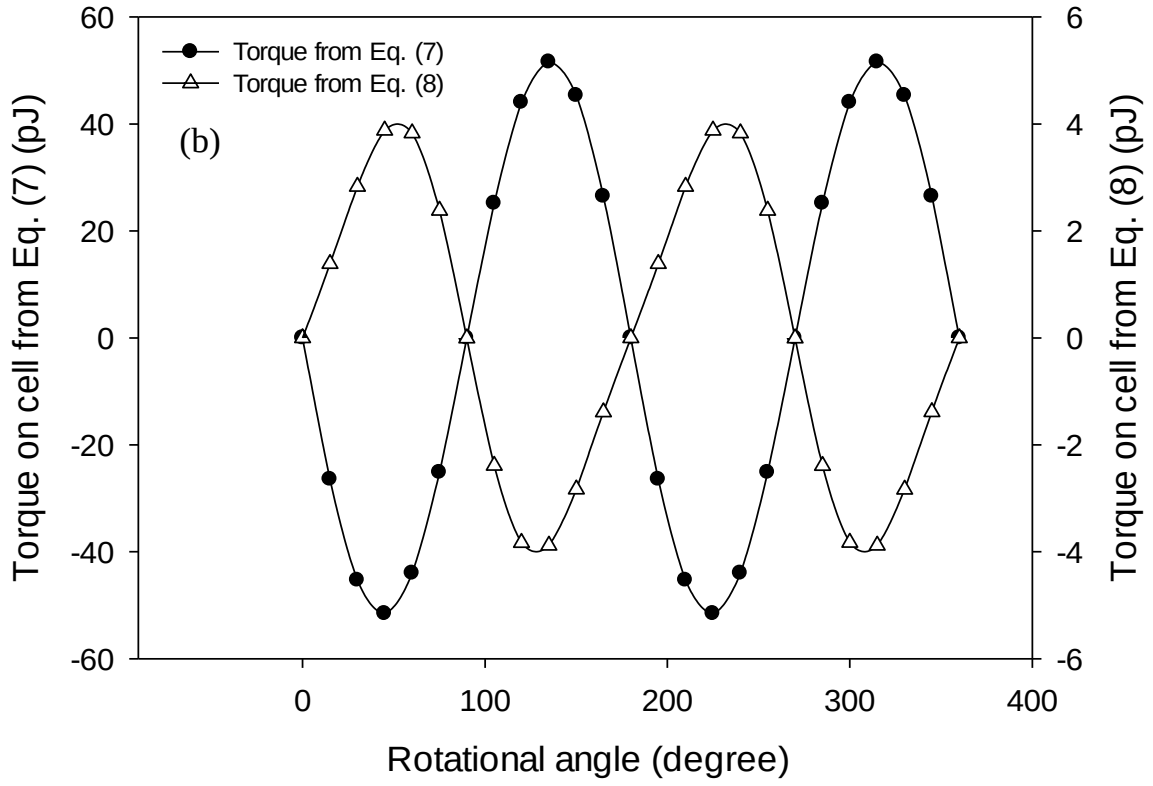

FIG. 4. (a) Geometry of the 2D model for quantifying torque exerted by electric field on cell. (b) Torques on cell from two expressions over a cycle of 360 degree.

3.4.3 Elucidating the mechanism of cell rotation

By inspecting the shapes of the cells that rotate in our experiments, we noted that the cells that rotate possess mostly irregular shapes. This observation led us to hypothesize that cells' non-spherical shapes are responsible for causing them to rotate. To prove this hypothesis, we created a 3D model mimicking the experimental setup (Fig. 5(a)), in which the width of electrodes is set at 100 μm and the gap distance at 80 μm. The electrodes are

marked in blue with the first and third (from left to right) electrodes grounded and the second and fourth electrically biased at 16 V. For a homogeneous spherical particle, changing in orientation will not affect the electric field inside the particle, thus the net torque will always be zero, indicating that it will not rotate. To simulate the non-spherical cell structure more closely, an ellipsoidal shaped particle with axis lengths of 20 μm, 15 μm and 10 μm in x, y and z directions, respectively, is considered and placed in the center of gap region between electrodes. First, we neglect cell nucleus and treat the interior of cell as having same dielectric property of the cytoplasm. Since the computational demand will be overwhelming if we mesh thin layer structures like the cell membrane in 3D model, to avoid this the geometric domain of the cell membrane is represented by the contact impedance boundary condition in COMSOL Multiphysics, which approximates the impedance of the membrane against the normal flow of ions, to capture the electric field distortion effect of the membrane. The dielectric properties of cell components and medium are given in Table 1.

Table 1. Parameters for calculating torque in 3D cell model

	Relative permittivity	Conductivity (S/m)
Cytoplasm	60	0.25
Cell membrane	10	0
Nucleus	60	6
Nuclear envelope	50	10^{-3}
Medium	78.5	2×10^{-4}

The ellipsoidal shaped cell is initially aligned with the major axis perpendicular to the edge of electrodes. It is then rotated counterclockwise by 15° incrementally. Fig. 5(b) shows that the torque on the cell exhibits a sine-wave type of variation as it rotates for a full range of 360° at 20 MHz. The average torque over this rotational span is determined to ascertain if the cell is experiencing a non-zero toque to sustain a continuous rotational motion. If the average torque is zero, the cell will be regarded as not be able to keep rotating due to viscous resistance of medium. The average torque is calculated as the sum of torque values at various evaluation angles (0°, 15°, 30°… 345°) divided by 24, the number of orientations considered in a full rotation span. To ensure reasonable evaluations, we calculated the average torque using the multiple sets of evaluation angles, e.g., at 5°, 20°, …, and 350°, or at 10°, 25°, …, and 355°. Table 2 (first column) lists the results from three sets when cell nucleus is ignored. Clearly, different sets of rotational spans generate both positive and negative values, indicating that the average torque value over a full rotation span is very small or close to zero. This suggests that ellipsoidal shape alone will not contribute to constant rotation of the cell.

We then consider an ellipsoidal cell with cytoplasm and off-centered spherical nucleus of 4 μm in radius. The dimension of the cell is kept the same as the case where nucleus is neglected. The nuclear envelope is also represented by the contact impedance boundary condition with a thickness of 40 nm.

Fig. 5(a) insets I and II show two cases in which the nucleus is positioned at different locations: in inset I the nucleus is in the upper right region of the cell while in inset II the nucleus sits in the lower right part. The locations of the nucleus in both cases

are symmetrical about the major axis. We calculate the torque exerted on cell over a full rational span of 360° at 20 MHz. Similarly, three sets of rotation spans are used to calculate the average torque. Table 2 (columns 2 and 3) lists the obtained results. When the nucleus is located on upper side, the net torque over a full rotational span is positive, suggesting that the cell will rotate counter-clockwise. When the nucleus is on the lower side, a negative net torque is obtained, indicating that the cell will rotate clockwise. Based on these results it is possible that cells could rotate in different directions depending on the relative location of nuclei inside. For further comparison, we also consider a spherical cell with off-centered nucleus as shown in Fig. 5(a) inset III. The nucleus is placed 5 μm away from the geometric center with a radius of 10 μm. In this case, the average torque is found to be much smaller (two orders of magnitude lower) (Table 2). These results, therefore, suggest that constant rotation of cell is unlikely to happen when a cell assumes a spherical shape, as confirmed by our observation.

Table 2. Torque on different types of cell models

	Ellipsoidal cell no nucleus	Ellipsoidal cell with upper nucleus	Ellipsoidal cell with lower nucleus	Spherical cell with nucleus
Orientations group 1 (J)	-4.76×10^{-22}	7.98×10^{-20}	-7.72×10^{-20}	1.61×10^{-22}
Orientations group 2 (J)	-7.34×10^{-23}	7.90×10^{-20}	-7.93×10^{-20}	9.88×10^{-23}
Orientations group 3 (J)	8.50×10^{-22}	7.58×10^{-20}	-7.87×10^{-20}	1.16×10^{-22}
Average of three groups (J)	1.00×10^{-22}	7.82×10^{-20}	-7.84×10^{-20}	1.25×10^{-22}

To further assess the possibility that cells could rotate about the y axis (parallel to the edge of electrodes), we modified the model further. Unlike rotation about the z axis, rotation about the y axis also involves the rise and fall of the cell centroid due to anisotropy. To simplify matters, we assume that rotation about the y axis will not cause deformation of the cell. Fig. 5(c) shows the orientation of a cell with its nucleus located on the right side in the beginning of a rotational span about the y axis. After calculating the torque at each orientation angle, we found the average torque to be 1.30×10^{-19} J for this case. As a reference, when the nucleus is on the opposite side in the beginning, the average torque is -1.30×10^{-19} J, suggesting that the net torque is not zero and depends on the position of the nucleus. When cells rotate about the y axis, they have to overcome the work of gravitational force, hence judging on the fact that the net torque is so small, it is believed that cells will rotate more easily about the z axis than about the y axis.

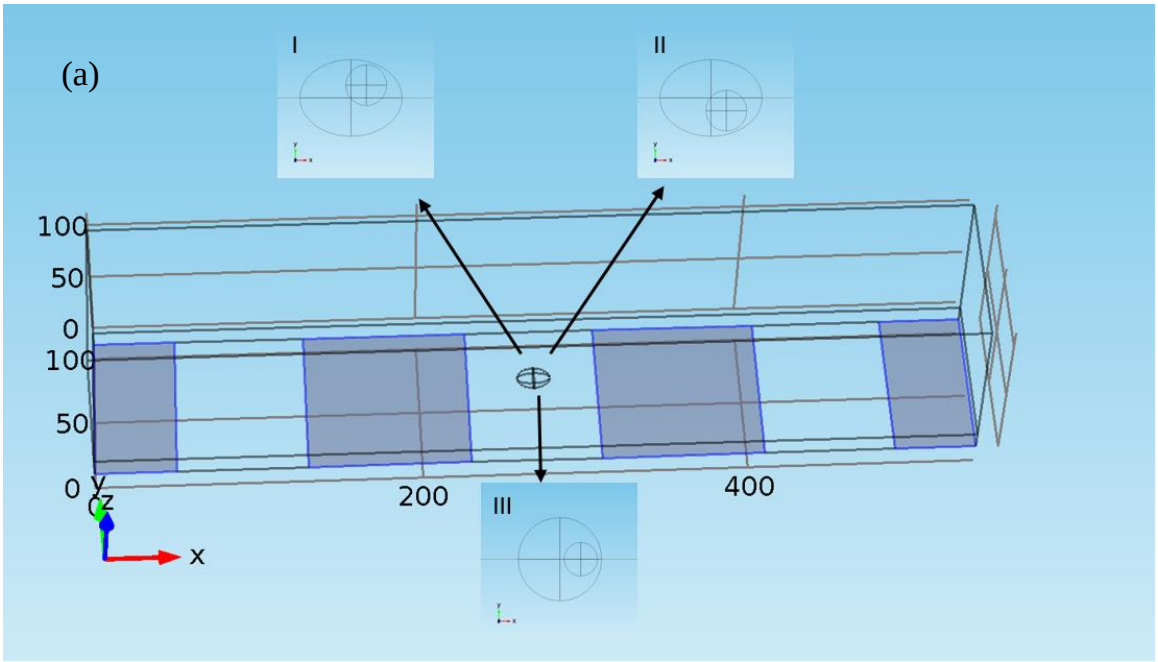
(a)
I
II
III
100
50
0
100
50
0
y
z
x
200
400

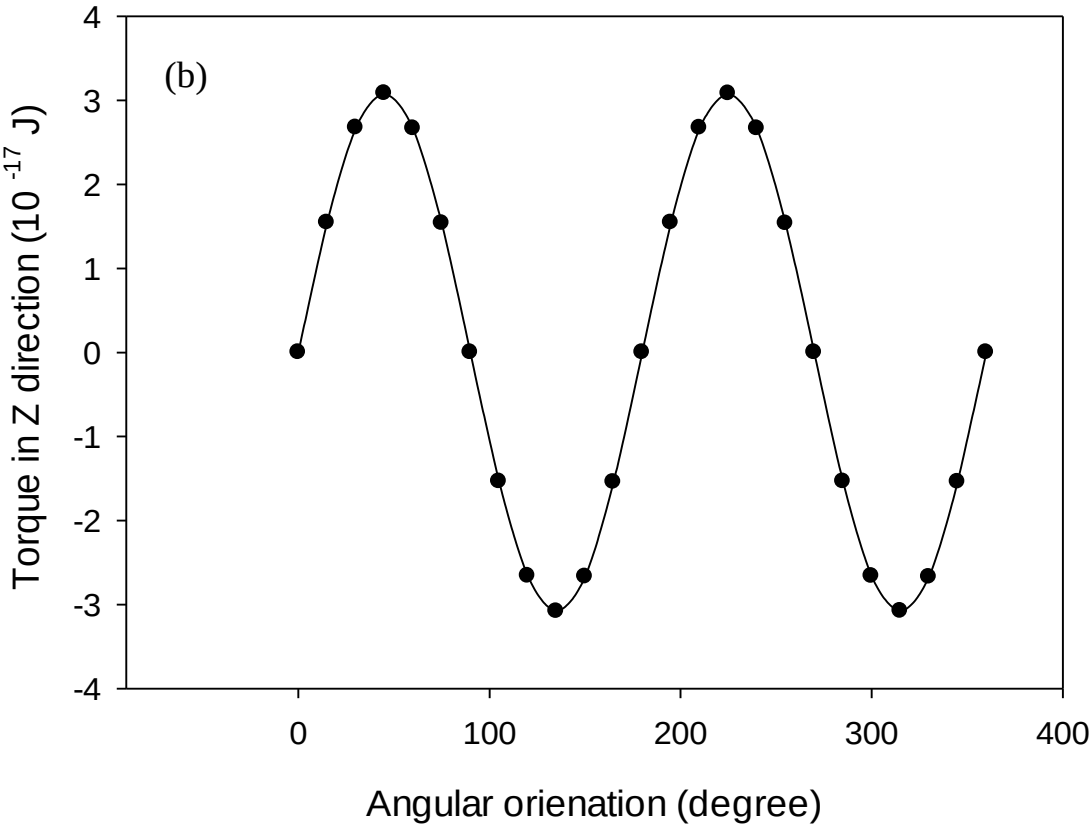
(b)
Torque in Z direction (10 -17 J)
4
3
2
1
0
-1
-2
-3
-4
0
100
200
300
400
Angular orienation (degree)

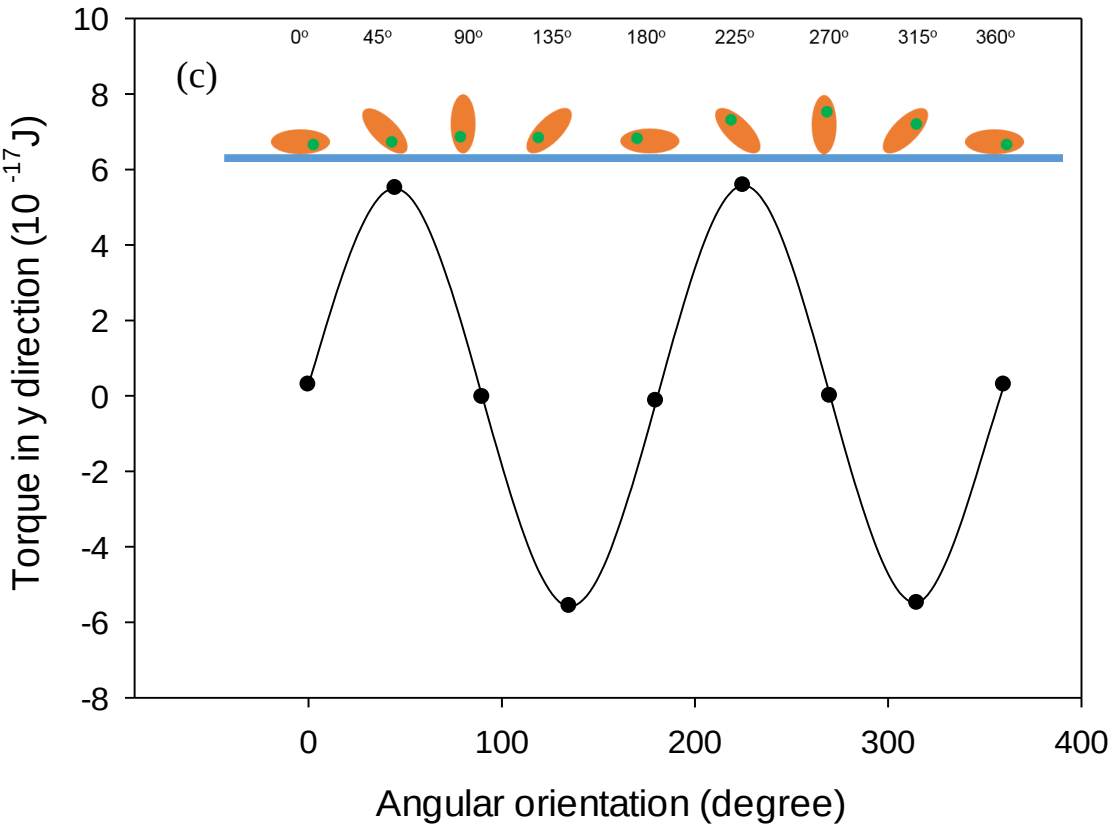
(c)
0°
45°
90°
135°
180°
225°
270°
315°
360°
Torque in y direction (10 -17 J)
10
8
6
4
2
0
-2
-4
-6
-8
0
100
200
300
400
Angular orientation (degree)

FIG. 5. (a) Illustration of 3D model setup. Cell lies in the center region between parallel electrodes and 16 V voltage is applied. I. Ellipsoidal cell with nucleus on the upper right region; II. Ellipsoidal cell with nucleus on the lower right region; III. Spherical cell with nucleus on the right side. (b) Torque in z direction on ellipsoidal cell with uniform dielectric property. Net torque over a cycle equals zero. (c) Torque in y direction on ellipsoidal cell with nucleus in lower part. Net torque over a cycle is non-zero. On top is schematic of cell with nucleus in lower part rotating about axis parallel to the edge of electrode (green circle represents nucleus).

Next we examine the influence of frequency on cell rotation by varying the frequency from 5 MHz to 50 MHz and quantifying the average torque. Fig. 6 shows that torque increases with frequency from 5 MHz to 20 MHz, which agrees with our experimental observation. As the frequency is further increased, the torque start to decrease gradually. This is attributed to that fact that the dielectric difference between cytoplasm and nucleoplasm reduces as the frequency becomes higher, consistent with the experimental observation on lymphocytes reported by Chau *et al* (Chau *et al* 2013).

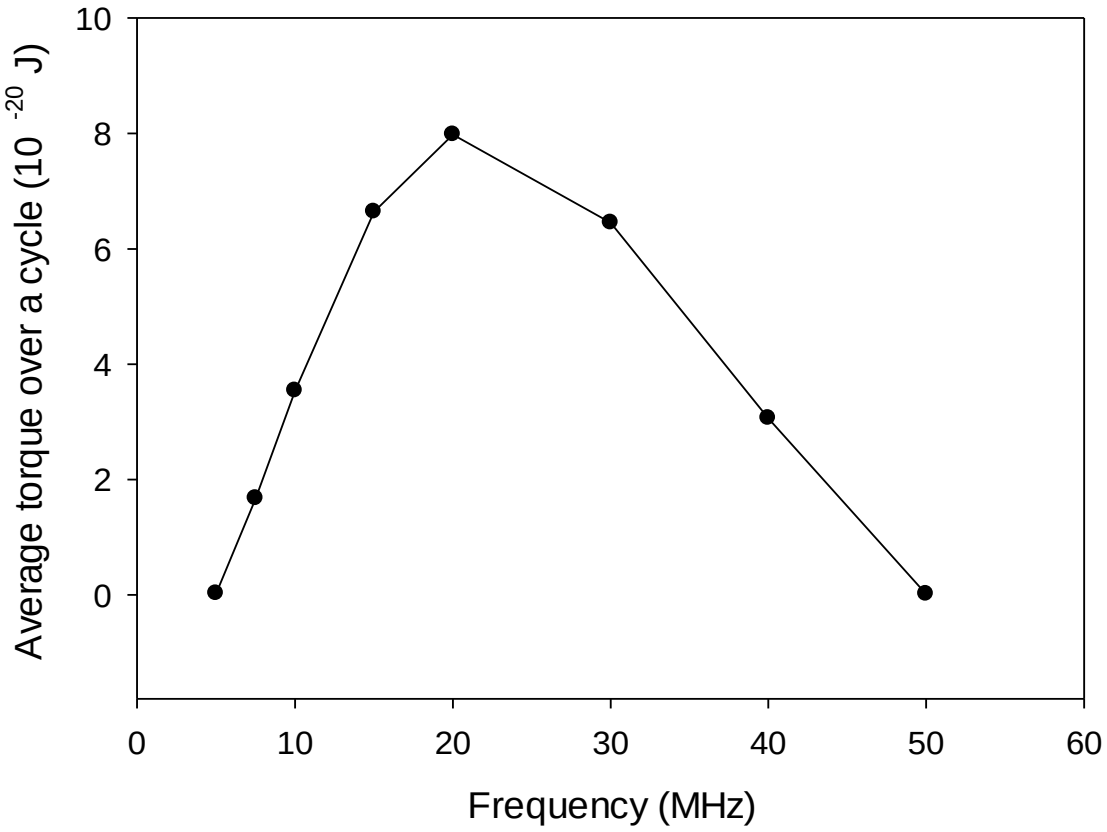

FIG. 6. The average torque over a cycle increases from 5 MHz to 20 MHz and gradually decreases when the frequency further increases.

To assess if the torque generated is strong enough to sustain the constant rotation of cell, we then estimated the rotational speed based on the torque. According to Sawatzki (1970), the drag torque acting on a sphere rotating around its diameter in fluid can be expressed as:

$$M = -C_{\omega}\frac{\rho}{2}\vec{\omega}\left|\vec{\omega}\right|r^{5} \tag{9}$$

where C_ω is the dimensionless drag torque coefficient and ρ is the density of liquid. For an ellipsoidal cell with off-centered nucleus on the upper side, the average torque at 20 MHz over a full rotational span is around 7.8×10^{-20} J. Assuming that the cell rotates in a constant speed, the torque generated from the DEP force and the torque from the drag force should be equal. Thus, by plugging the value of C_ω (0.08) derived from Vlasák *et al* (Vlasák *et al* 2013), the rotational speed is estimated at around 100 rad/s, suggesting that the torque generated by DEP is strong enough to induce fast rotation of cells.

3.5 Conclusions

We developed a new cell model by accounting for a cell's inner structure to quantify the force and torque exerted on different components of the cell. This new model predicts well how DEP force exerting on the cell changes with frequency leading to the quantification of crossover frequency for the cell. In examining possible factors affecting first and second crossover frequency, we confirmed with 3D modeling that non-spherical shapes and off-centered nucleus are responsible for inducing cell's self-rotation. This prediction is consistent with our experimental observation.

Reference

Ai, Y., and Qian, S., "DC dielectrophoretic particle–particle interactions and their relative motions," Journal of colloid and interface science 346, 448-454 (2010)

Ai, Y., Zeng, Z., and Qian, S., "Direct numerical simulation of AC dielectrophoretic particle–particle interactive motions," Journal of colloid and interface science 417, 72-79 (2014)

An, J., Lee, J., Lee, S. H., Park, J., and Kim, B., "Separation of malignant human breast cancer epithelial cells from healthy epithelial cells using an advanced dielectrophoresis-activated cell sorter (DACS)," Analytical and bioanalytical chemistry 394, 801-809 (2009)

Chau, L. H., Liang, W., Cheung, F. W. K., Liu, W. K., Li, W. J., Chen, S. C., and Lee, G. B., "Self-rotation of cells in an irrotational AC E-field in an opto-electrokinetics chip," PloS one 8, e51577 (2013)

Chen, N. C., Chen, C. H., Chen, M. K., Jang, L. S., and Wang, M. H., "Single-cell trapping and impedance measurement utilizing dielectrophoresis in a parallel-plate microfluidic device," Sensors and Actuators B: Chemical 190, 570-577 (2014)

Doh, I., Lee, W. C., Cho, Y. H., Pisano, A. P., and Kuypers, F. A. "Deformation measurement of individual cells in large populations using a single-cell microchamber array chip," Applied physics letters 100, 173702 (2012)

Gagnon, Z., Gordon, J., Sengupta, S., and Chang, H. C., "Bovine red blood cell starvation age discrimination through a glutaraldehyde‐amplified dielectrophoretic approach with buffer selection and membrane cross‐linking," Electrophoresis 29, 2272-2279 (2008)

Gascoyne, P. R., Wang, X. B., Huang, Y., and Becker, F. F., "Dielectrophoretic separation of cancer cells from blood," IEEE transactions on industry applications 33, 670-678 (1997)

Gimsa, J., Marszalek, P., Loewe, U., and Tsong, T. Y., "Dielectrophoresis and electrorotation of neurospora slime and murine myeloma cells," Biophysical journal 60, 749-760 (1991)

Guido, I., Jaeger, M. S., and Duschl, C., "Dielectrophoretic stretching of cells allows for characterization of their mechanical properties," European Biophysics Journal 40, 281-288 (2011)

Ho, C. T., Lin, R. Z., Chang, W. Y., Chang, H. Y., and Liu, C. H., "Rapid heterogeneous liver-cell on-chip patterning via the enhanced field-induced dielectrophoresis trap," Lab on a Chip 6, 724-734 (2006)

Ho, C. T., Lin, R. Z., Chen, R. J., Chin, C. K., Gong, S. E., Chang, H. Y., and Liu, C. H., "Liver-cell patterning lab chip: mimicking the morphology of liver lobule tissue," Lab on a Chip 13, 3578-3587 (2013)

House, D. L., Luo, H., and Chang, S., "Numerical study on dielectrophoretic chaining of two ellipsoidal particles," Journal of colloid and interface science 374, 141-149 (2012).

Hu, N., Yang, J., Yin, Z. Q., Ai, Y., Qian, S., Svir, I. B., Xia, B., Yan, J. W., Hou, W. S. and Zheng, X. L., "A high‐throughput dielectrophoresis‐based cell electrofusion microfluidic device," Electrophoresis 3, 2488-2495 (2011)

Jen, C. P., and Chen, T. W., "Selective trapping of live and dead mammalian cells using insulator-based dielectrophoresis within open-top microstructures," Biomedical microdevices 11, 597-607 (2009)

Kang, Y., Li, D., Kalams, S. A., and Eid, J. E., "DC-Dielectrophoretic separation of biological cells by size," Biomedical microdevices 10, 243-249 (2008)

Kimura, Y., Gel, M., Techaumnat, B., Oana, H., Kotera, H., and Washizu, M., "Dielectrophoresis‐assisted massively parallel cell pairing and fusion based on field constriction created by a micro‐orifice array sheet," Electrophoresis 32, 2496-2501 (2011)

Liang, W., Zhang, K., Yang, X., Liu, L., Yu, H., and Zhang, W., "Distinctive translational and self-rotational motion of lymphoma cells in an optically induced non-rotational alternating current electric field," Biomicrofluidics 9, 014121 (2015)

Ling, S. H., Lam, Y. C., and Chian, K. S., "Continuous cell separation using dielectrophoresis through asymmetric and periodic microelectrode array," Analytical chemistry 84, 6463-6470 (2012)

Mittal, M., and Furst, E. M., "Electric Field‐Directed Convective Assembly of Ellipsoidal Colloidal Particles to Create Optically and Mechanically Anisotropic Thin Films," Advanced Functional Materials 19, 3271-3278 (2009)

Ouyang, M., Cheung, W. K., Liang, W., Mai, J. D., Liu, W. K., and Li, W. J., "Inducing self-rotation of cells with natural and artificial melanin in a linearly polarized alternating current electric field," Biomicrofluidics 7, 054112 (2013)

Pethig, R., "Review article—dielectrophoresis: status of the theory, technology, and applications," Biomicrofluidics 4, 022811 (2010)

Pethig, R., Menachery, A., Pells, S., and De Sousa, P., "Dielectrophoresis: a review of applications for stem cell research," BioMed Research International 2010

Sawatzki, O., "Das Strömungsfeld um eine rotierende Kugel," Acta Mechanica, 9, 159-214 (1970)

Şen, M., Ino, K., Ramón-Azcón, J., Shiku, H., and Matsue, T., "Cell pairing using a dielectrophoresis-based device with interdigitated array electrodes," Lab on a Chip 13, 3650-3652 (2013)

Singh, J. P., Lele, P. P., Nettesheim, F., Wagner, N. J., and Furst, E. M., "One-and two-dimensional assembly of colloidal ellipsoids in ac electric fields," Physical Review E 79, 050401 (2009)

Sukhorukov, V. L., Mussauer, H., and Zimmermann, U. "The effect of electrical deformation forces on the electropermeabilization of erythrocyte membranes in low-and high-conductivity media," The Journal of membrane biology 163, 235-245 (1998)

Talary, M. S., Burt, J. P. H., Tame, J. A., and Pethig, R., "Electromanipulation and separation of cells using travelling electric fields," Journal of Physics D: Applied Physics 29, 2198 (1996)

Vaillier, C., Honegger, T., Kermarrec, F., Gidrol, X., and Peyrade, D., "Comprehensive analysis of human cells motion under an irrotational AC electric field in an electro-microfluidic chip," PloS one 9, e95231 (2014)

Vlasák, P., Chára, Z., and Kysela, B., "Experimental Evaluation of Drag Force, Drag Torque, and Magnus Force Acting on a Rotating Particle Moving in Fluid," In ASME 2013 Fluids Engineering Division Summer Meeting(pp. V01CT20A012-V01CT20A012). American Society of Mechanical Engineers (2013)

Wang, X. B., Huang, Y., Becker, F. F., and Gascoyne, P. R. C., "A unified theory of dielectrophoresis and travelling wave dielectrophoresis,".Journal of Physics D: Applied Physics 27, 1571 (1994)

Yang, J., Huang, Y., Wang, X., Wang, X. B., Becker, F. F., and Gascoyne, P. R., "Dielectric properties of human leukocyte subpopulations determined by electrorotation as a cell separation criterion," Biophysical journal 76, 3307-3314 (1999)

Yasukawa, T., Hatanaka, H., and Mizutani, F., "Simple detection of surface antigens on living cells by applying distinct cell positioning with negative dielectrophoresis," Analytical chemistry 84, 8830-8836 (2012)

Zhao, Y., Hodge, J., Brcka, J., Faguet, J., Lee, E., and Zhang, G., "Elucidating the mechanism governing the cell rotation behavior under DEP," COMSOL conf. Pro. Boston (2013)

Zhao, Y., Brcka, J., Faguet, J., and Zhang, G., "Elucidating the DEP phenomena using a volumetric polarization approach with consideration of the electric double layer," Biomicrofluidics 11, 024106 (2017)

Zhu, J., Canter, R. C., Keten, G., Vedantam, P., Tzeng, T. R. J., and Xuan, X., "Continuous-flow particle and cell separations in a serpentine microchannel via curvature-induced dielectrophoresis," Microfluidics and nanofluidics 11, 743-752 (2011)

CHAPTER FOUR

ELUCIDATING THE MECHANISM OF PARTICLE-PARTICLE INTERACTION UNDER DEP BY TWO CASES: TUMBLING MOTION OF PEARL CHAINS AND ALIGNMENT OF ELLIPSOIDAL PARTICLES

Abstract

While the mechanism governing the alignment of spherical particles with similar sizes has been studied by using different approaches, the movement of pearl chain structures under DEP in a flow condition is by no means understood. Some work has been done to simulate the alignment of ellipsoidal particles. But the modeling results do not match experimental observations. In this paper, the authors applied our newly developed volumetric-integration method to elucidate the underlying mechanism for a newly observed movement of pearl chains under DEP in a flow condition, and explain the alignment patterns of ellipsoidal particles.

4.1 Introduction

As one of the most studied electrokinetic phenomena, dielectrophoresis (DEP) has been recognized as having promising potential in manipulating small particles since DEP can be used to move either charged or non-charged particles. Initially, the applications of DEP are mainly focused on separating different types of particles. Based on the difference

in physical or dielectric property, particles are either guided into separate trajectories or pushed into different regions (Church *et al* 2010, 2011, Kang *et al* 2008, Lapizco-Encinas *et al* 2004, Li *et al* 2013, Moon *et al* 2011). Lately, due to significant progresses made in the field of biomanufacturing, researchers are paying more attention to apply the DEP technique to pattern cells based on the interaction forces between them. For example, cells of different types have been patterned into liver-like tissue structure with specially designed electrodes (Ho *et al* 2006, 2013). Moreover, cell fusion is successfully achieved based on the close alignment of cells between parallel electrodes (Gel *et al* 2010, Kimura *et al* 2011).

To elucidate the governing mechanism for particle alignment, various modeling approaches have been developed. Based on the technical differences in these methods, they can be divided into two classes: point-dipole approach and Arbitrary Lagrangian-Eulerian (ALE) moving mesh approach based on the MST method. With the point-dipole approach, researchers have gained certain understanding of the alignment of particles with different initial orientations (Kadaksham *et al* 2006). The ALE method provides more accurate estimation of the DEP force as well as the hydrodynamic force, albeit the number of particles that can be considered is limited. For example, the dynamic movement of several particles (usually two to three) under either DC or AC condition have been investigated in detail (Ai and Qian 2010, Ai *et al* 2014).

Most DEP applications are based upon the pearl chain structures formed by particles on a planar surface, in which a peal chain structure serves as a basic unit for forming large-scale patterns and structures. The promising potential of the DEP technology

in biomanufacturing would be hindered if no other alignment or movement modes for the particles can be generated. To advance the field of DEP and diversify its applications, we conducted experiments coupled with computational modeling to investigate the alignment and movement of particles under fluid flow conditions rather than static conditions. Moreover, unlike in most of the previous work dealing with particles of the same size, we also considered the alignment of particles of different sizes.

To elucidate the underlying mechanisms for some newly observed particle movements or alignments, we used three modeling approaches: static force analysis based on volumetric-integration method, ALE method based on volumetric-integration and interactive point-dipole method. The volumetric-integration method is a newly developed method which overcomes the limitations of MST method. Each of the three approaches has its advantage and disadvantage and thus we will use the most appropriate one to suit the right situations.

Additionally, we also investigated the alignment of ellipsoidal particles. For ellipsoidal particles, although some modeling work has been conducted, the modeling results do not seem to capture experimental observations closely (House *et al* 2012, Singh *et al* 2009). In our approach we employed an integrative approach combining experimental observation and computational modeling to investigate the mechanisms governing some newly observed particle movements and alignments under DEP in our own experiments.

4.2 Experimental setup and observation

4.2.1 Experimental setup

On the experimental side, the test setup mainly consists of a chip with interdigitated electrodes etched on it as the base. A polyethylene insulation layer covers the base chip and a chamber with inlet is built on top of the insulation layer. During experiments polystyrene particles suspended in DI water are injected into the chamber through the inlet. For electric biasing, an AC potential signal is applied to the interdigitated electrodes in an alternating live/ground manner. The AC signal is generated by a waveform generator (WGF600; FLC Electronics Inc., Sweden). All optical images are recorded with an inverse optical microscope (Axiovert s100; Zeiss, Germany).

4.2.2 Experimental observation

A. Tumbling motion of pearl chains of particles in a flow condition

10 μm polystyrene particles were mixed in DI water and injected into the chamber. Under an AC signal at 20 Vpp and 20 MHz, particles formed pearl-chain structures in the gap region between electrodes. When a fluid flow condition perpendicular to the edge of electrode was introduced to the medium to cause the particles to move across electrodes, we observed a very interesting phenomenon in which particle chains aligned horizontally in the gap regions move along with the flow and the chains assume a vertical configuration when they are above the electrodes. This phenomenon can be seen in the images recorded

sequentially in time during experiments (note the highlighted chain in red circles in particular) shown in Fig. 1(a)-(f). In a close inspection, it is noted that the change in configurations of the particle chaines appears to take a tumbling motion. Since this type of tumbling motion under DEP has not been reported or investigated in the literature, we repeated the experiment by using particles of different sizes such that we can be certain that the change in configurations of the particle chains is in a tumbling motion. By tracing the motions and configurations of the same chains of particles in consecutive images in Fig. 1(g)-(h) (e.g., the ones highlighted either in small green circles or in large red circles), we noted that the chains of particles move along in a clockwise tumbling motion. In this tumbling motion, the trailing particle of a horizontal chain becomes the leading one after assuming a vertical configuration, as depicted in Fig. 1(i).

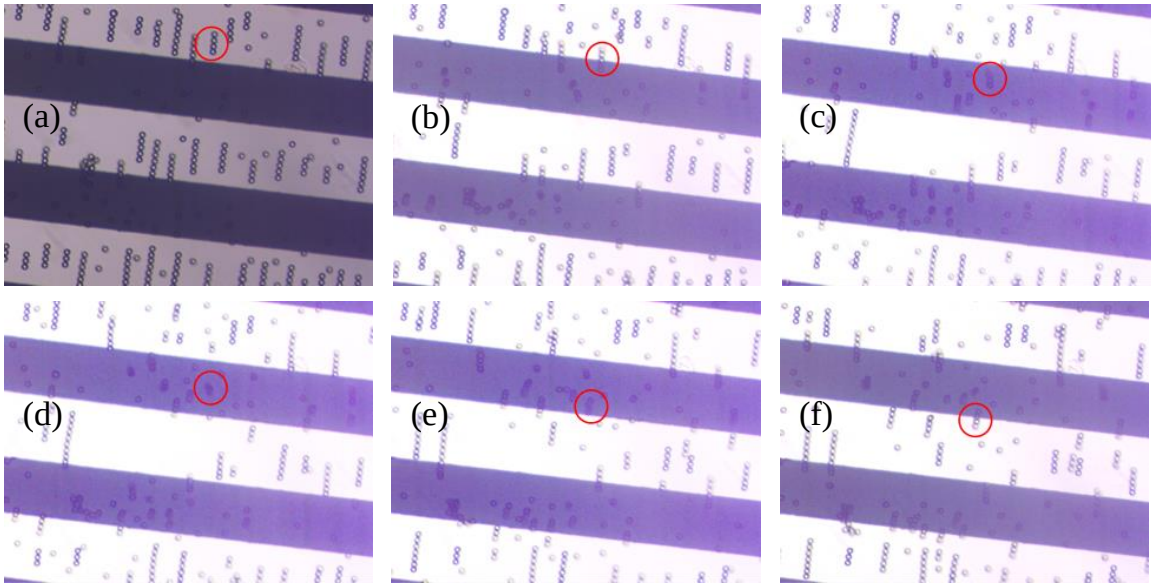
(a)
(b)
(c)
(d)
(e)
(f)

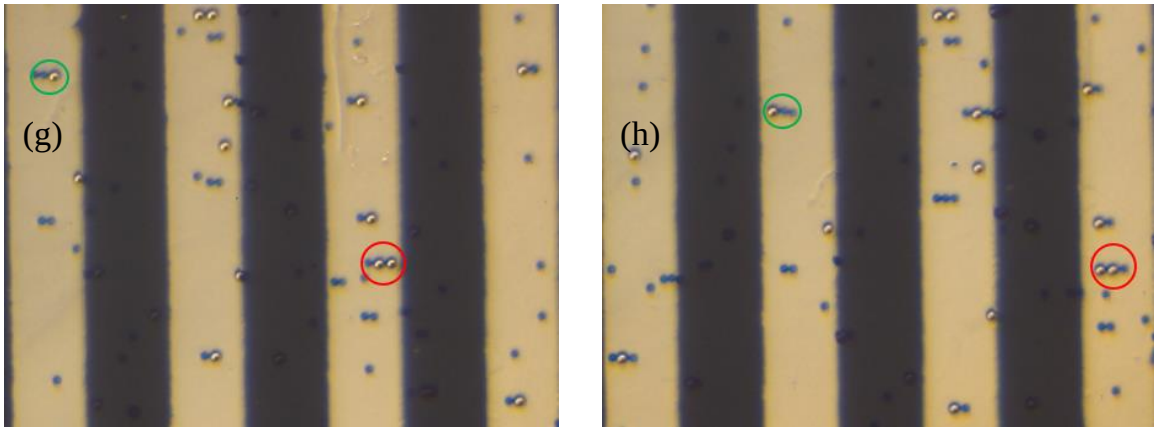
(g)
(h)

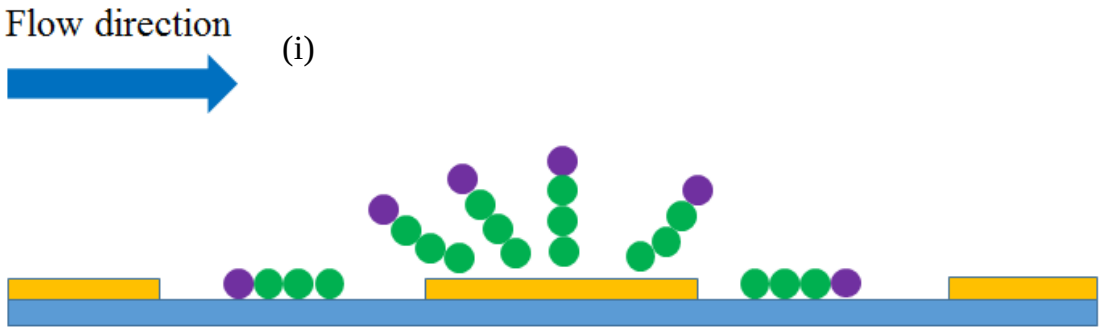
Flow direction
(i)

FIG.1. Optical images showing the tumbling motion of particle chains. A chain of four particles circled in red moves with the flow in a gap region (a), near the edge of an electrode (b), above the electrode off to the upper side (c), at the center the electrode (d), off the lower side (e), and near the other edge of the electrode (f). (g) and (h) Tumbling motion of chains of particles with different sizes. (i) Schematic illustration of the tumbling motion of a chain of particles. The trailing end of the chain gets lifted up to form an angle with the floor and stand straight at the center of electrodes, and after that the chain gradually tumbles back as it moves into the next gap region.

B. Alignment of particles with mixed sizes

In a different experiment with particles of mixed sizes (radius = 7.5 μm and 1 μm), we observed the formation of different antenna-like structures at different frequencies in static DI water. At a high frequency (20 MHz), both the large and small particles experience nDEP, and the resulted antenna-like structure is shown in Fig. 2(a). At a low frequency (100 kHz), the large particles still expereince nDEP but the small ones pDEP due to larger surface conductance (Arnold *et al* 1987), and the resulted antenna-like structure is shown in Fig. 2(b).

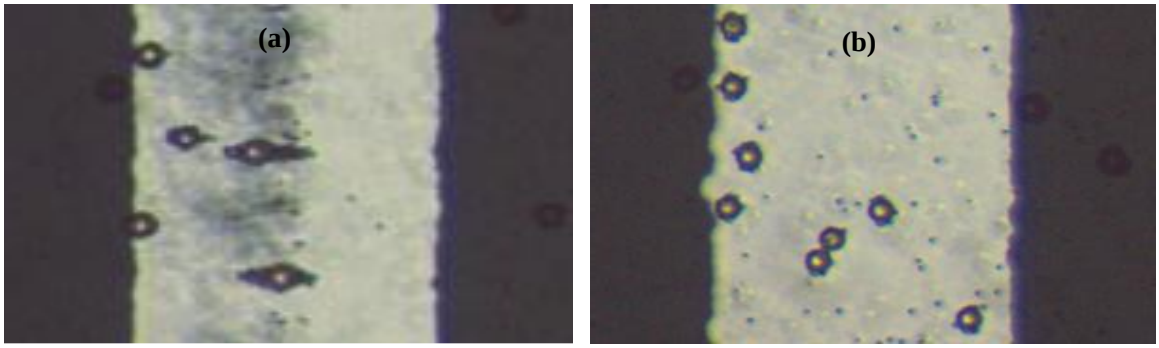

FIG.2. (a)-(b) Images of antenna-like structure formed by mixed size particles (7.5 μm and 1 μm) at a high frequency of 20MHz (a) and a low frequency of 100 kHz (b).

4.3 Theoretical development

4.3.1 Volumetric-integration method (for spherical and non-spherical particle)

In our previous paper (Zhao *et al* 2017) we have developed a new method based on volumetric polarization to quantify the DEP force exerted on particles. Here we will expand this volume integration method to investigate the above observed DEP phenomena through minimization of the total energy.

A spherical infinitesimal unit inside the particle placed in electric field is treated as a dipole composed of two point charges with opposite polarity (Q and $-Q$) separated by a distance of d (d is the diameter of the spherical particle unit). The potential on the two point charges are U_+ and U_- respectively. The electrostatic energy on each point charge can be expressed as QU_+ and $-QU_-$ respectively. By summing these two terms together we have:

$$w_p = QU_+ - QU_- = Q\vec{\boldsymbol{d}}\frac{U_+ - U_-}{\vec{\boldsymbol{d}}} \tag{1}$$

where $\vec{\boldsymbol{d}}$ is the vector pointing from the negative point charge to the positive point charge. Per the definition of dipole moment and electric field, Eq. (1) can be expressed as:

$$w_p = -\mathrm{d}\vec{\boldsymbol{m}} \cdot \vec{\boldsymbol{E}} \tag{2}$$

where $\mathrm{d}\vec{\boldsymbol{m}}$ is the dipole moment of the particle unit and $\vec{\boldsymbol{E}}$ is the original electric field (as if the particle possesses the same property as the surrounding medium or is not there) at the location of the particle unit.

Based on previously derived expression of polarization density in terms of electric field, Eq. (2) can be expressed as:

$$w_p = -\vec{\boldsymbol{P}} \cdot \vec{\boldsymbol{E}}\mathrm{d}V = 3\varepsilon_m(\vec{\boldsymbol{E}}_{particle} - \vec{\boldsymbol{E}}) \cdot \vec{\boldsymbol{E}}\mathrm{d}V \tag{3}$$

where ε_m is the permittivity of medium and $\vec{\boldsymbol{E}}_{particle}$ is the electric field inside the particle unit. Thus the total energy of the particle can be expressed in summation as:

$$W_p = \iiint 3\varepsilon_m(\vec{\boldsymbol{E}}_{particle} - \vec{\boldsymbol{E}}) \cdot \vec{\boldsymbol{E}}\mathrm{d}V \tag{4}$$

If the object to be studied is ellipsoid, the torque needs to be considered other than the electrostatic potential energy. For a particle unit, the torque exerted by the electric field can be derived as:

$$\vec{t} = \vec{r}_+ \times (Q\vec{E}_+) + \vec{r}_- \times (-Q\vec{E}_-) = Q(\vec{r}_+ \times (\vec{E} + \frac{(\nabla \cdot \vec{E})\vec{d}}{2}) - \vec{r}_- \times (\vec{E} - \frac{(\nabla \cdot \vec{E})\vec{d}}{2}))$$
$$= Q((\vec{r}_+ - \vec{r}_-) \times \vec{E} + (\vec{r}_+ - \vec{r}_-) \times \frac{(\nabla \cdot \vec{E})\vec{d}}{2}) = Q\vec{d} \times \vec{E} + Q\vec{d}\frac{(\nabla \cdot \vec{E})\vec{d}}{2} = \mathrm{d}\vec{m} \times \vec{E} \quad (5)$$
$$= \vec{P} \times \vec{E}\mathrm{d}V = 3\varepsilon_m(\vec{E} - \vec{E}_{particle}) \times \vec{E}\mathrm{d}V$$

where $\vec{r}_+$ and $\vec{r}_-$ are the vectors from a random point to the positive and negative point charges. $\vec{E}_+$ and $\vec{E}_-$ are the electric field at the positive and negative point charges. The net torque exerted by electric field on the ellipsoidal particle can also be expressed in summation as:

$$\vec{T} = \iiint 3\varepsilon_m(\vec{E} - \vec{E}_{particle}) \times \vec{E}\mathrm{d}V \quad (6)$$

With Eq. (4) the stable orientation of particle in an electric field can be determined by minimizing the total energy. The torque on the particle will also be examined to ensure the stability of the lowest-energy state. To study the alignment of ellipsoidal particles, we will first test the validity of Eq. (4) and (6) by analyzing the orientation of single ellipsoidal particle and the orientation of a pearl chain formed by spherical particles. We will then investigate the chain configurations of ellipsoidal particles and compare with experimental observations (Singh *et al* 2009).

4.3.2 Arbitrary Lagrangian-Eulerian (ALE) method (for spherical particle)

To study the dynamic movement of particles in fluid, governing equations for both the fluid flow and solid mechanics are simultaneously solved. For the fluid, the mass and momentum conservation conditions can be expressed as:

$$\rho_{fluid} \nabla \cdot \boldsymbol{u}_{fluid} = 0 \tag{7}$$

$$\rho_{fluid} \frac{\partial \boldsymbol{u}_{fluid}}{\partial t} + \rho_{fluid} (\boldsymbol{u}_{fluid} \cdot \nabla) \boldsymbol{u}_{fluid} = \nabla \cdot [-p\mathbf{I} + \eta(\nabla \boldsymbol{u}_{fluid} + (\nabla \boldsymbol{u}_{fluid})^{\mathrm{T}})] \tag{8}$$

where $\boldsymbol{u}_{fluid}$ is the velocity of the fluid, ρ_{fluid} the density of fluid, p the pressure and η the dynamic viscosity.

For the particle, the movement is governed by the following equations:

$$\rho_{particle} \frac{\partial^2 \mathbf{u}_{solid}}{\partial t^2} - \nabla \cdot \boldsymbol{\sigma} = (3\varepsilon_m (\vec{\boldsymbol{E}} \text{-} \vec{\boldsymbol{E}}_{particle}) \cdot \nabla) \vec{\boldsymbol{E}} \tag{9}$$

$$\boldsymbol{\varepsilon} = \frac{1}{2} [(\nabla \mathbf{u}_{solid})^{\mathrm{T}} + \nabla \mathbf{u}_{solid} + (\nabla \mathbf{u}_{solid})^{\mathrm{T}} \nabla \mathbf{u}_{solid}] \tag{10}$$

where $\mathbf{u}_{solid}$ is the displacement of particle, $\rho_{particle}$ the density of particle, $\boldsymbol{\sigma}$ the stress tensor, $\boldsymbol{\varepsilon}$ the strain tensor. The part on the right-hand side of Eq. (9) is the DEP force density. Because rotation of this spherical particle will not change the electric field distribution inside the particle, the net torque exerted by electric field is zero, hence there is no need to consider the effect of torque exerted by electric field on a spherical particle.

At the interface between particle and fluid, we have the following relationship:

$$\boldsymbol{u}_{fluid} = \frac{\partial \mathbf{u}_{solid}}{\partial t} \tag{11}$$

$$\boldsymbol{\sigma} \cdot \boldsymbol{n} = [-p\mathbf{I} + \mu(\nabla \boldsymbol{u}_{fluid} + (\nabla \boldsymbol{u}_{fluid})^{\mathrm{T}})] \cdot \boldsymbol{n} \tag{12}$$

To ensure that multiple particles will not coalesce together, a normal interaction force between two adjacent particles is assigned as follows:

$$\vec{\boldsymbol{F}}_{ij} = \begin{cases} k\left(q\alpha_i - q\alpha_j\right)\left(\exp\left(\left(2a - d_{ij}\right)/l\right) - 1\right) & d_{ij} <= 2a \\ 0 & d_{ij} > 2a \end{cases} \quad (\alpha = x, y, z) \tag{13}$$

where d_{ij} represents the distance between particle i and particle j, k a coefficient, a the radius of particle, l a small constant value, $q\alpha$ the coordinates of particle with α representing one of the three orthogonal directions. To prevent the particle sticking to the floor, it is also necessary to keep the particle above the bottom floor by applying a proper boundary condition to the particle in the form of a vertical uplifting force to keep the particle afloat, as:

$$\vec{\boldsymbol{F}}_n = \begin{cases} k\left(th + a - qh\right) & qh < th + a \\ 0 & qh \geq th + a \end{cases} \tag{14}$$

In this expression, th is the thickness of the insulation layer, and qh the height location of the center of the particle. Eq. (14) basically assures that the particle will only experience an uplifting force when it falls (mathematically) below the level of $th + a$.

Aside from the forces considered above, the particle is also subject to gravitational force and buoyancy force as follows:

$$\vec{\boldsymbol{F}}_g = vol \cdot \rho_{particle} \cdot g \tag{15}$$

$$\vec{\boldsymbol{F}}_b = vol \cdot \rho_{medium} \cdot g \tag{16}$$

where $\vec{\boldsymbol{F}}_g$ is gravitational force, $\vec{\boldsymbol{F}}_b$ buoyancy force, vol volume of particle. Since we normally deal with particles with sizes up to tens of microns, the impact of drifting due to diffusion and Brownian motion is regarded as negligible. The particle-fluid-surface system

can be simultaneously solved using the ALE method to obtain the positions of particles at each moment.

4.3.3 Interactive point dipole method (for spherical particle)

In point dipole model, The DEP force $\vec{F}$ on a particle can be expressed as (Wang *et al* 1994)

$$\vec{F} = (\vec{m} \cdot \nabla)\vec{E} \tag{17}$$

Here $\vec{m}$ stands for the dipole moment of the particle. The dipole moment is determined by the permittivity and volume of the particle as well as the difference in dielectric property between particle and medium, which is usually represented by the Clausius-Mossotti factor ($f\_cm = \frac{\varepsilon_p^* - \varepsilon_m^*}{\varepsilon_p^* + 2\varepsilon_m^*}$, in which ε_p^* and ε_m^* are the complex permittivity of particle and medium respectively). For the circumstance where a single particle exists, the electric field strength ($\vec{E}$) is solely determined by the local electric field generated by electrodes. However, when multiple particles are present in the system, each particle will be affected by the fields generated by other particles. The electric field at a point in space generated by a particle can be expressed as (La Magna *et al* 2012):

$$\vec{E}_p = \frac{1}{4\pi\varepsilon_m R^3}(3(\vec{m} \cdot \hat{R})\hat{R} - \vec{m}) \tag{18}$$

Here R is the distance between the point and geometric center of particle and $\hat{\boldsymbol{R}}$ is the unit vector along the direction pointing from center of particle to the point. By including the electric field generated by surrounding particles in Eq. (18), the particle-particle interaction is considered. Other than gravitational force (Eq. (15)) and buoyancy force (Eq. (16)), particles also experience hydrodynamic force:

$$\vec{\boldsymbol{F}}_h = 6\pi a\mu\vec{\boldsymbol{v}} \tag{19}$$

where $\vec{v}$ is relative velocity between fluid and the particle.

4.4 Numerical implementation

4.4.1 Tumbling motion of pearl chains of particles in a flow condition

3D models are built with same geometry as in experimental setup using COMSOL Multiphysics as shown in Fig. 3(a) (side view). The electrode width and gap distance between electrodes are both set at 100 μm. On top of the electrode is polyethylene layer (relative permittivity = 2.3) with thickness of 12 μm. To simplify the problem, we only consider pearl chains formed by two particles. To apply the volumetric-integration method to static force analysis, two particles in contact are considered in the model. In this case, the orientation of the particle chain as well as the position of the particles can be freely adjusted. The stable orientations of the particle chain at different positions above electrodes are determined. For the static force analysis method, only the Electric Current Module is solved in Frequency Domain Study. The two side electrodes are biased by 10 V and the

middle electrode is grounded. Secondly, the ALE method is implemented through the Fluid-Structure Interaction Module. Two particles in contact are initially placed in the gap region lying on the bottom. The same electrical biasing condition as in the static force analysis is applied. By solving the Fluid-Structure Interaction Module along with Electric Current Module in Time Dependent Study, the movement of particle chains can be simulated. The third approach is to use an interactive point dipole method, in which the two particles are treated as two points initially in contact lying on the floor. In this case, Laminar Flow Module, Mathematical Particle Tracing Module and Electric Current Module are simultaneously solved in Time Dependent Study. To simplify matters, both the particle and fluid are treated as pure dielectric material (conductivity equals zero). This approximation is appropriate when the conductivity of fluid is low and frequency is high.

4.4.2 Alignment of particles with mixed sizes

A 3D model with a similar geometry as in Section 4.4.1 is built. Two (2) large particles (particle radius = 7.5 μm) and 98 small particles (particle radius = 1 μm) are released in a designated region in the gap. The surface conductance (K_S) of the large and small particles are set to be identical so the conductivity of the large particles (σ_l) and the small particles (σ_s) is inversely proportional to their respective radius. In this case, since we are simulating a large numbers of particles, it is more efficient to use interactive point dipole method. Mathematical Particle Tracing Module and Electric Current Module are

simultaneously solved in Time Dependent Study to simulate the alignment process of 100 particles. The values of parameters used are listed in Table 1.

Table 1. Parameters used in interactive point dipole model

Parameter	Physical meaning	Value
k	Coefficient of normal force	10^{-12} N/μm
d	Thickness of insulation layer	12 μm
l	A small value to characterize normal force change	1 μm
$\rho_{particle}$	The density of particle	1050 kg/m^3
ρ_{medium}	The density of medium	1000 kg/m^3
η	Dynamic viscosity	10^{-3} Pa·s
K_S	Surface conductance of particle	1.2 nS
σ_l	Conductivity of 7.5 μm particle	3.2×10^{-4} S/m
σ_s	Conductivity of 1 μm particle	2.4×10^{-3} S/m
σ_m	Conductivity of medium	1.8×10^{-4} S/m
ε_m	Permittivity of medium	78.5
ε_p	Permittivity of particle	2.5

4.4.3 Ellipsoidal particle alignment

Another 3D model is created with the same geometry as in Singh's experiment design using COMSOL Multiphysics as shown in Fig. 3(b). In the model, parallel electrodes in a rectangular shape are placed at the bottom with width set at 1 mm and length set at 500 μm. The gap distance between two electrodes is 2 mm. On top of electrode is pure dielectric material with height of 100 μm to mimic the adhesive spacer used in

experiment. Above the bottom plane in the gap region is a medium layer with height of 100 μm. The parallel electrodes are biased by an AC signal in an alternating biasing/ground manner. The particle is placed atop the bottom plane in the center of the gap. The electric field with and without particle presence are first solved with the Electric Current Module and Frequency Domain Study. In Frequency domain, the electric field is expressed in a complex variable, by taking the phase lag between polarization and electric field into consideration, the electrostatic potential energy as well as the torque of the particle can be expressed as:

$$W_p = \frac{1}{2} Re(\iiint 3\varepsilon_m (\vec{\boldsymbol{E}}_{particle} - \vec{\boldsymbol{E}}) \cdot \vec{\boldsymbol{E}}^* \mathrm{d}V) \tag{20}$$

$$\vec{\boldsymbol{T}} = \frac{1}{2} Re(\iiint 3\varepsilon_m (\vec{\boldsymbol{E}} - \vec{\boldsymbol{E}}_{particle}) \times \vec{\boldsymbol{E}}^* \mathrm{d}V) \tag{21}$$

where $\vec{\boldsymbol{E}}^*$ is the conjugate of electric field.

For the case of alignment of multiple particles, it is important to note that the original electric field $\vec{\boldsymbol{E}}$ is different for the calculation of energy and torque. The electrostatic potential energy is a value defined relative to the initial electric field. All particles in the system will be assigned with the dielectric property of medium to obtain the original electric field. By contrast, the torque is an absolute value which includes the influence of particle-particle interaction from surrounding particles. Thus, only the particle to be studied will be assigned the dielectric property of medium while all other particles are assigned their intrinsic dielectric property to obtain the original electric field.

A. Validation of integration expression of energy and torque

a. Orientation of a single ellipsoidal particle

For comparison with experiment, all ellipsoidal particles with different aspect ratios considered here have the same volume as the spherical particle because in Singh's experiment all ellipsoidal particles are made from spherical particles with a diameter of 3 μm. By assuming that the minor axes are of equal length, the length of the major axis and minor axis are $3n^{2/3}$ and $3n^{-1/3}$ μm, respectively, where n is the aspect ratio of the particle. An AC potential signal is applied to the electrodes to create a parallel electric field over the gap region with an rms value of 100 V/cm. A single ellipsoidal particle with an aspect ratio of 3 is placed in the center of gap region. The particle and medium are treated as pure dielectric material (conductivity equals zero), with the relative permittivity of medium set at 78.5. Two different polarization cases are considered here. In the first case, the relative permittivity of particle is 60 (smaller than that of medium) and in the second, the relative permittivity of particle is 100 (larger than that of medium). The orientation of particles is characterized by the angle between the major axis and the electric field. The particle is parametrically rotated about its geometric center counterclockwise from 0° to 360° with an incremental 30° step. Electrostatic potential energy and torque of particle are calculated at each orientation.

b. Orientation of pearl chain formed by spherical particles

Here we study the configuration of particle chains formed by three particles by examining the state of the middle particle. The relative permittivity of particle and medium are set at 2.5 and 78.5, respectively. In the model, three particles are initially aligned in a line parallel to the electric field. The three particles shall always align in a line when the middle particle is in a force equilibrium. Considering the symmetrical condition, the chain is parametrically rotated from 0° to 90° with the middle particle fixed. Electrostatic potential energy and torque of particles are calculated for the middle particle at each orientation.

B. Alignment of ellipsoidal particles

To facilitate comparison with experimental observation, both the particle and medium are assigned with the same dielectric property as in the experiment. The conductivity of sodium dodecyl sulfate (SDS) solution with concentration of 2.5 mM is 2×10^{-2} S/m (Khan and Shah 2008) and the surface conductance of polystyrene particles is assumed to be 1.2 nS. The surface conductance is converted to conductivity of particles according to the relationship for a spherical particle: $K_{total} = K_{bulk} + \frac{2K_s}{a}$ where K_{bulk} is the bulk conductivity and K_s is the surface conductance. a is the radius of spherical particle (1.5 μm).

We consider three ellipsoidal particles initially aligned in a line with the major axis parallel to the electric field. The two particles on each side rotate around the geometric

center of the middle particle and always maintain a point contact with the middle particle. The geometric centers of the three particles are always kept in a line to ensure force equilibrium. The orientation of the chain is varied from 0° to 90° with the middle particle remained fixed in orientation. The electrostatic potential energy and torque are calculated for the middle particle at each chain orientation to identify the stable angle for the chain. The value for the surface conductance is also varied for studying its effect on the stable orientation of particle chain.

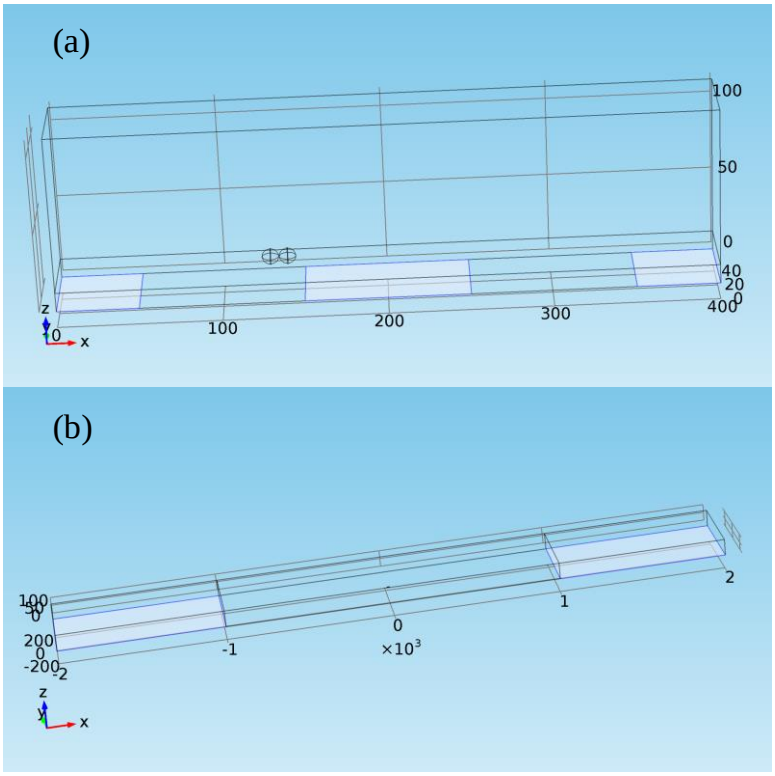
(a)
100
50
0
40
20
0
400
300
200
100
0
z
x
(b)
100
50
0
200
0
-200
-2
-1
0
×10³
1
2
z
x

(c)

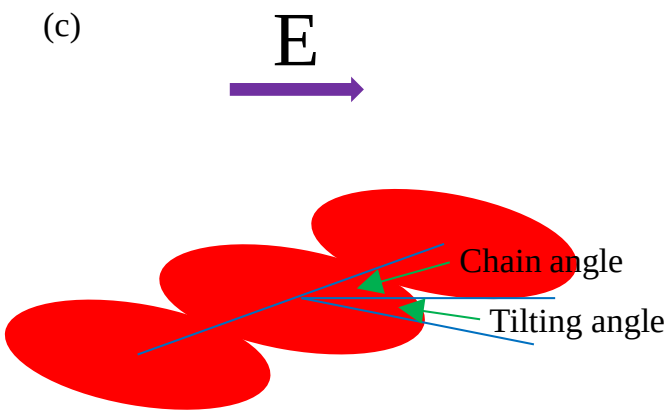
E
Chain angle
Tilting angle

(d)

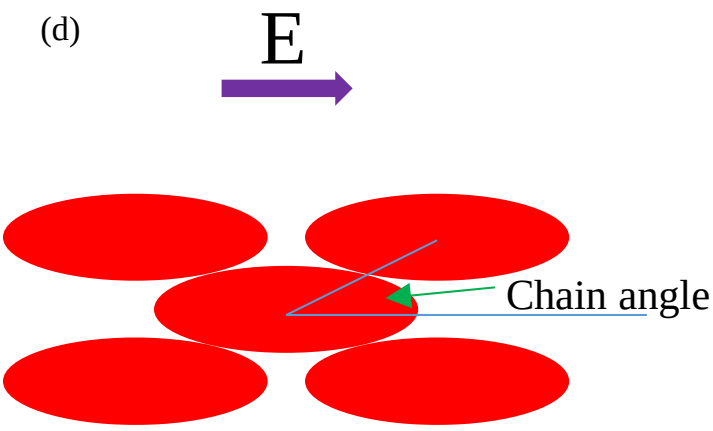
E
Chain angle

FIG.3. (a) Geometry of the 3D model for simulating the tumbling motion of pearl chain in a flow condition. (b) Geometry of the 3D model same as the experimental setup of Singh et al for simulating the alignment of ellipsoidal particles. (c) Illustration of ellipsoidal particle alignment in chain configuration. (d) Illustration of ellipsoidal particle alignment in stacked configuration.

4.5 Results and discussion

4.5.1 Tumbling motion of pearl chains of particles in a flow condition

A. Static force analysis

For the tumbling motion to occur, the particles should always remain in a stable contact condition as their positions and orientation change. Since the particles will move with flow, they are assumed to be always in quasi-static condition. Using the free-body diagram shown in Fig. 4(a), where Fx1, Fz1, Fx2 and Fz2 are the x and z components of the DEP force for particles 1 and 2 respectively, N is the normal contact force and net-force-1 and net-force-2 are the net force (i.e., gravitation – bouyancy) for each particle, we can express the stable contact conditions as 1) Fx1 - N $\cos\theta$ = Fx2 + N $\cos\theta$ (equilibrium in x direction), 2) Fz1 + N $\sin\theta$ = net-force-1 and Fz2 – N $\sin\theta$ = net-force-2 (equilibrium in z direction). Note that when we consider particles of the same material and the same size, these two net forces will be the same (estimated to be around 2.57×10^{-13} N). Thus the second condition becomes Fz1 + N $\sin\theta$ = Fz2 – N $\sin\theta$ = 2.57×10^{-13} N. To examine these conditions in detail, we first placed the leading particle of the two-particle chain at 170 μm

on the floor and allowed the tailing particle to assume an oblique position. As the oblique angle increases from 0° to 90°, we obtained the relevant forces as listed in Table 1. The normal force N was obtained by assuming equilibrium condition in x direction was satisfied. Within the angular range from 11.25° to 67.5°, Fz1 + N $\sin\theta$ keeps increasing while Fz2 – N $\sin\theta$ decreasing as angle increases and they will become equal at some angle between 45° and 56.25°. However the magnitude is larger than 2.57×10^{-13} N. This fact suggests that the two particles will not be in a stable union in this position. But when the leading particle was placed 16 μm above the floor, the situation changed. As listed in Table 2, the condition Fz1 + N $\sin\theta$ = Fz2 – N $\sin\theta$ $\approx 2.57\times10^{-13}$ N can be reached when the angle is about 50°, indicating that the chain of particles will rise a bit and take this orientation as a stable union. By repeating this procedure with the position of the leading particle set to vary from the gap close to edge (140 μm) to the center (200 μm) of the electrode we obtained the variation of the stable angle as a function of the particle position. Fig. 4(b) shows that the oblique angle of the chain of particles will increase from 5° when the chain is 10 μm away from the edge of the electrode to 90° when the chain is at the center of the electrode. Since the force is symmetrical about the center of the electrode, the chain of particles will tumble back to a horizontal configuration once it moves into the next gap region.

Table 2. Forces on two particles (particle 2 sits on the floor on top of electrode 20 μm from the left edge)

θ	Fx1 (10^{-13}N)	Fx2 (10^{-13}N)	Fz1 (10^{-13}N)	Fz2 (10^{-13}N)
0	-3.12	6.50	16.7	3.25×10^{-2}
11.25	2.40	0.299	14.8	-0.353
22.5	6.49	-4.25	10.8	2.16
33.75	8.28	-6.24	5.72	6.12
45	7.70	-5.63	1.07	10.1
56.25	5.28	-3.00	-2.17	13.0
67.5	1.94	0.683	-3.42	14.0
78.75	-1.33	4.32	-2.60	13.0
θ	Fx1-Fx2 (10^{-13}N)	N (10^{-13}N)	Fz1 + N $\sin\theta$ (10^{-13}N)	Fz2 – N $\sin\theta$ (10^{-13}N)
0	-9.61	-4.81	16.7	3.25×10^{-2}
11.25	2.10	1.07	15.0	-0.562
22.5	10.7	5.81	13.0	-6.56×10^{-2}
33.75	14.5	8.73	10.6	1.27
45	13.3	9.42	7.73	3.44
56.25	8.28	7.45	4.02	6.79
67.5	1.26	1.64	-1.90	12.5
78.75	-5.64	-14.5	-16.8	27.2

Table 3. Forces on two particles (particle 2 sits 16 μm above the floor on top of electrode 20 μm from the left edge)

θ	Fx1 (10^{-13}N)	Fx2 (10^{-13}N)	Fz1 (10^{-13}N)	Fz2 (10^{-13}N)
0	-0.700	1.39	6.90	-0.354
11.25	1.78	-1.13	6.22	-0.185
22.5	3.62	-3.00	4.37	1.23
33.75	4.32	-3.68	2.02	3.25
45	3.83	-3.12	-0.134	5.20
47.81	3.56	-2.82	-0.569	5.61
50.63	3.23	-2.46	-0.951	5.97
53.44	2.86	-2.06	-1.28	6.27
θ	Fx1-Fx2 (10^{-13}N)	N (10^{-13}N)	Fz1 + N $\sin\theta$ (10^{-13}N)	Fz2 – N $\sin\theta$ (10^{-13}N)
0	-2.09	-1.04	6.90	-0.354
11.25	2.91	1.49	6.51	-0.474
22.5	6.62	3.58	5.74	-0.144
33.75	8.00	4.81	4.69	0.579
45	6.95	4.91	3.34	1.73
47.81	6.38	4.75	2.95	2.09
50.63	5.69	4.49	2.52	2.50
53.44	4.92	4.13	2.04	2.96

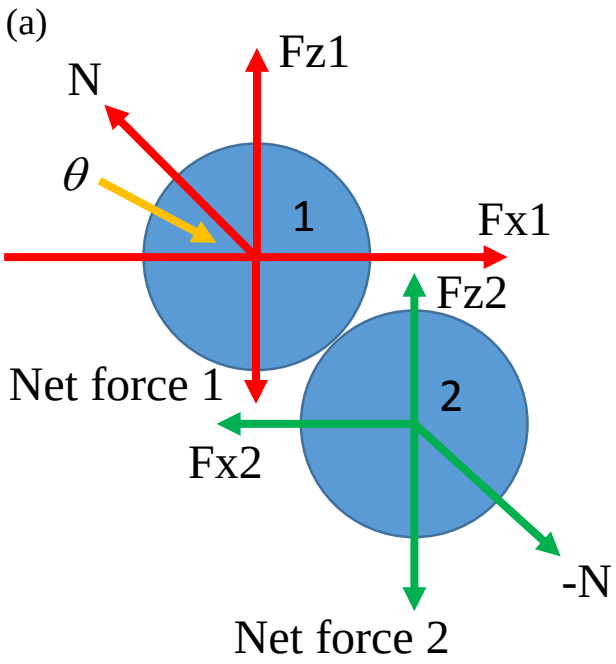
(a)
N
Fz1
θ
1
Fx1
Fz2
Net force 1
2
Fx2
-N
Net force 2

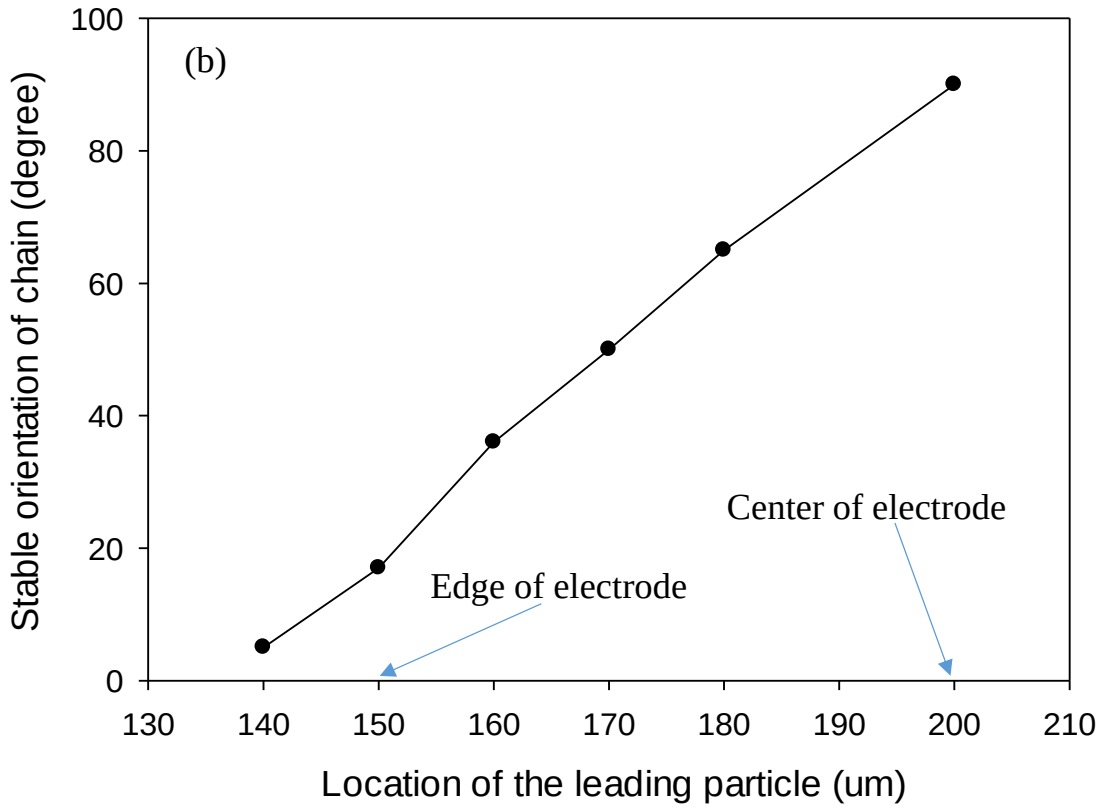

FIG.4. (a) A free-body diagram showing two particles in contact, where Net force equals the difference of gravitational force and buoyancy force, N is normal force and θ is the angle. (b) The stable angle formed by the particles with respect to the floor increases as the chain of particles moves from the gap region close to the edge of electrode to the center of an electrode.

B. ALE method

While the ALE method allows accurate consideration of all possible forces, especially the hydrodynamic force, because the ALE method utilizes moving mesh technique, the mesh elements will be strongly distorted when the displacement increases, which could lead to a convergence problem. To avoid this problem, the displacement of the particles will be exported and used to reset the initial positions of particles in an incremental iterative process. The average flow velocity is set to be 20 μm/s because at a higher flow rate convergence will be an issue again. Fig. 5(a)-(f) show the variation of the pearl-chain orientation as the chain moves with flow, capturing exactly the observed tumbling motion for the particle chain. The difference between the results of the ALE method and static force analysis is that the chain will assume upright configuration before it reaches the center of electrode in ALE method. This is likely due to negligence of the hydrodynamic forces on particles in the static force analysis.

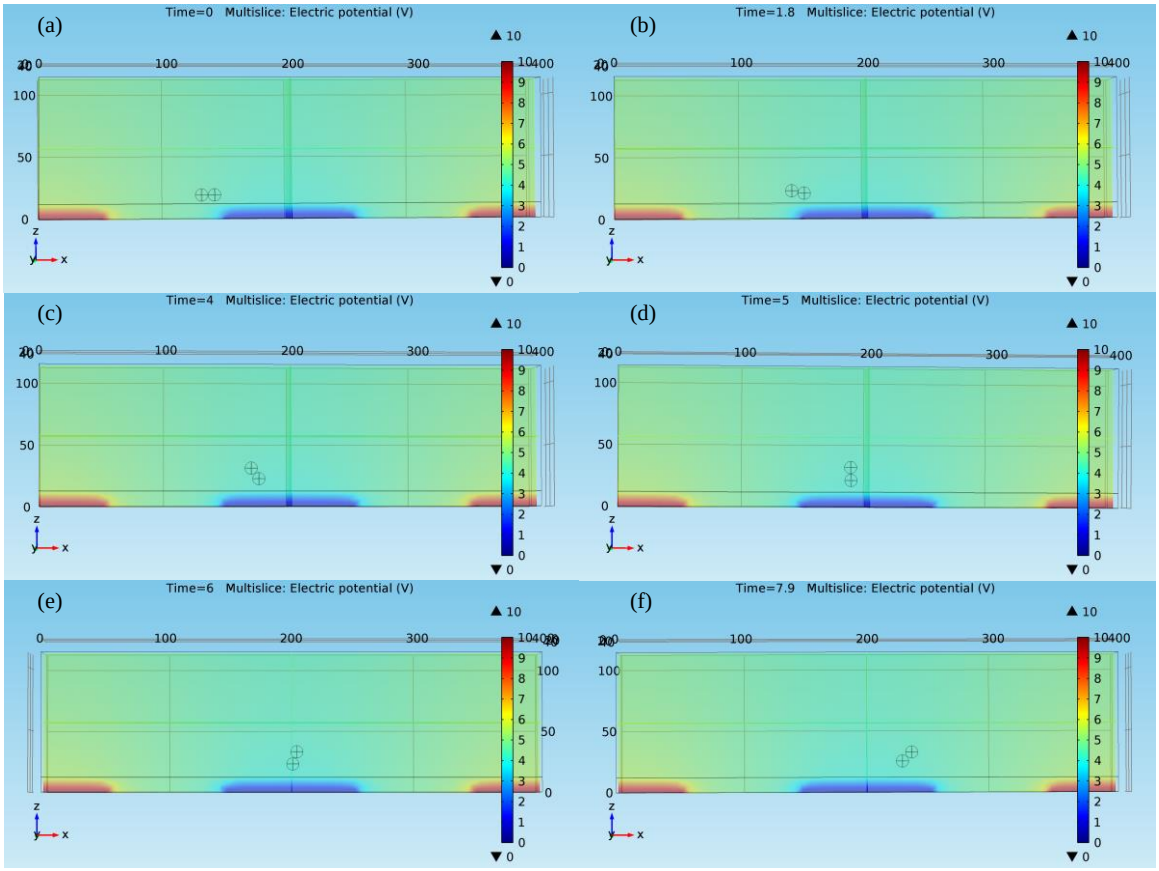

FIG.5. The orientation and position of chains formed by two particles from ALE method at different time points. (a) 0 second (b) 1.8 seconds (c) 4 seconds (d) 5 seconds (e) 6 seconds (f) 7.9 seconds. The scale bar represents the potential distribution.

C. Interactive point dipole method

When the biasing AC signal is at 10 V (same in both the static analysis and ALE method), the two particles will separate from each other when they reach the edge of the electrode as shown in Fig. 6(a)-(d). When the potential is increased to 15 V, two particles will keep in contact and exhibit the tumbling motion as shown in Fig. 6(e)-(h). But instead

of having the trailing particle to levitate, the leading particle rises in the beginning. This fact may suggest that the interactive point-dipole method is not able to capture the interaction between particles in a flow condition correctly.

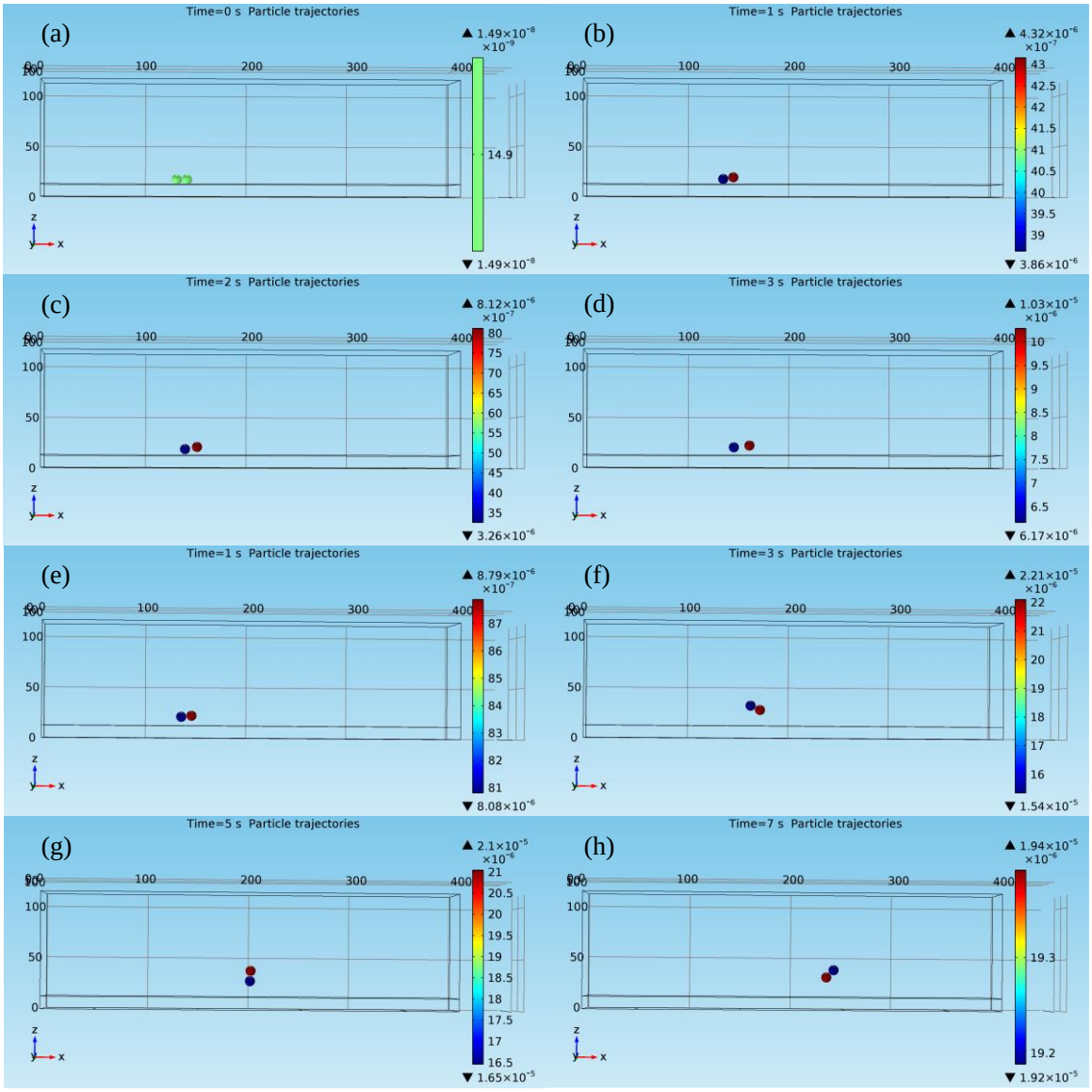

FIG.6. The orientation and position of chains formed by two particles from interactive point dipole method at different time points. (a)-(d) 10 V (e)-(h) 15 V. The scale bar represents the velocity of particle.

4.5.2 Alignment of particles with mixed sizes

Fig. 7(a) shows the modeling result at a high frequency (20 MHz) in which small particles gather around the large ones by entending in tail-like constructs on both the right and left sides of the large particles (along the direction of the electrical field). Fig. 7(b) shows that at a low frequency (100 kHz) small particles in pearl-chains will coalesce together with the large particles from the above and below. Clearly, the antenna-like structures observed in our experiments resemble these modeling predictions, suggesting that the interactive point dipole method for DEP analysis can capture very well experimental observations.

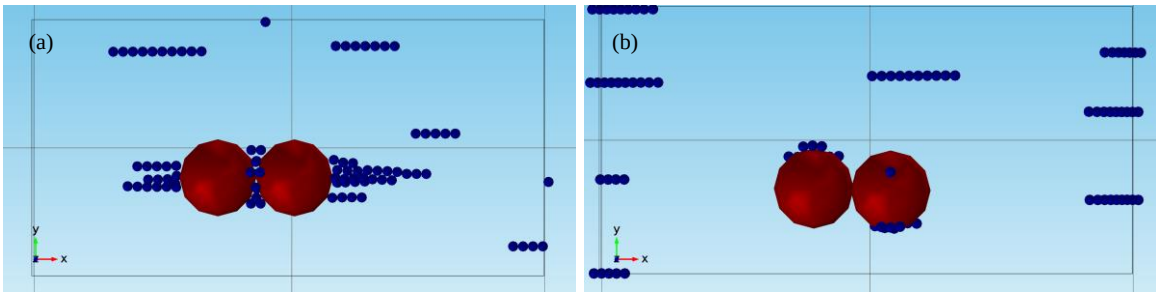

FIG.7. Simulated results of particle structures by interactive dipole method at 20 MHz (a) and 100 kHz (b).

4.5.3 Ellipsoidal particle alignment

A. Validation of integration expression of energy and torque

a. Orientation of a single ellipsoidal particle

Fig. 8(a) shows the variation of electrostatic potential energy and torque with the orientation of the ellipsoidal particle. When the particle has relative permittivity of 60, it experiences nDEP. The electrostatic potential energy reaches its minimum at 0° and 180°, where the major axis is aligned along the direction of electric field. The torque is zero when the major axis is either in parallel or perpendicular to the electric field direction. By examining the change in torque through introducing a small rotation angle in these orientations, we noted that only when the major axis is parallel to the electric field, the particle will return to its original orientation. In this case, the electrostatic potential energy and torque are consistent in predicting the stable orientation of ellipsoidal particle. When the particle has relative permittivity of 100, it experiences pDEP. Both the electrostatic potential energy and torque predict an orientation of perpendicular alignment. These modeling results agree with the experimental results by Mittal and Furst (2009), where the titanium oxide ellipsoidal particles align perpendicular to the electric field at low frequency due to high surface conductance. At high frequency, the particles undergo transition from pDEP to nDEP and start to align parallel to the electric field.

b. Orientation of pearl chain formed by spherical particles

Fig. 8(b) shows the variation of electrostatic potential energy and torque experienced by the middle particle with the orientation of the particle chain. The energy is minimum and the torque is zero when the chain is parallel to the electric field, suggesting that a parallel alignment is a stable configuration for the particle chain formed by spherical particles under nDEP. This conclusion again agrees with experimental observation and confirms the validity of the integration expression of energy and torque.

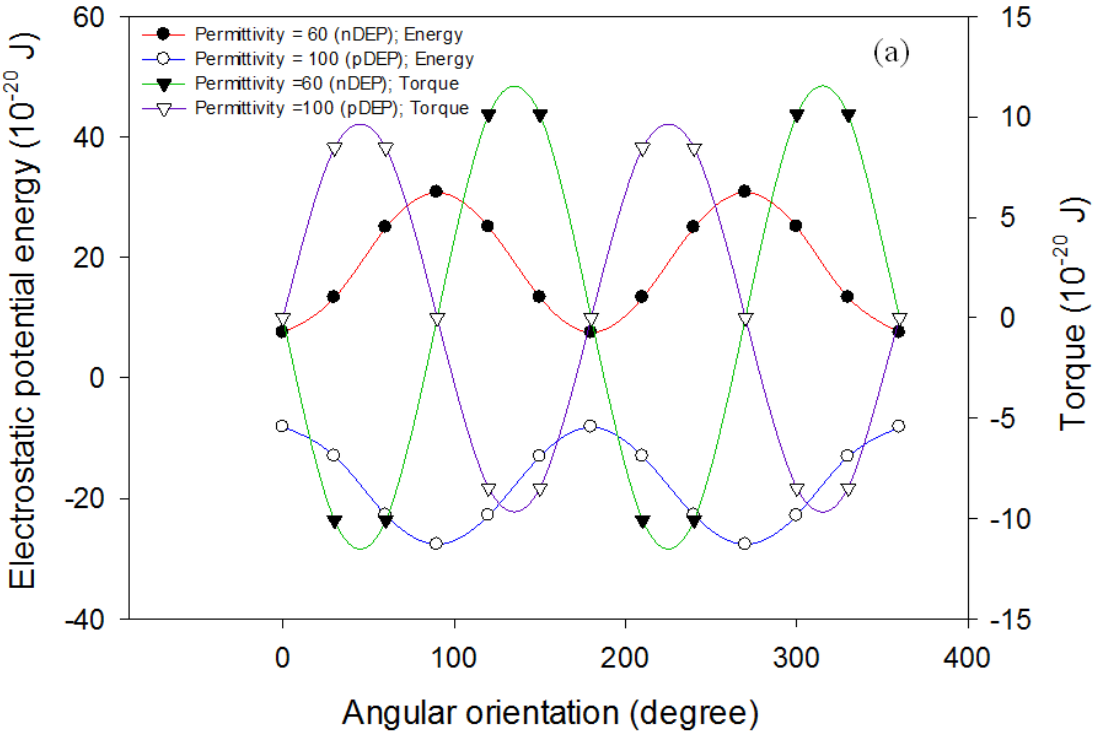
Permittivity = 60 (nDEP); Energy
Permittivity = 100 (pDEP); Energy
Permittivity =60 (nDEP); Torque
Permittivity =100 (pDEP); Torque
(a)
Electrostatic potential energy (10-20 J)
Torque (10-20 J)
Angular orientation (degree)
60
40
20
0
-20
-40
15
10
5
0
-5
-10
-15
0
100
200
300
400

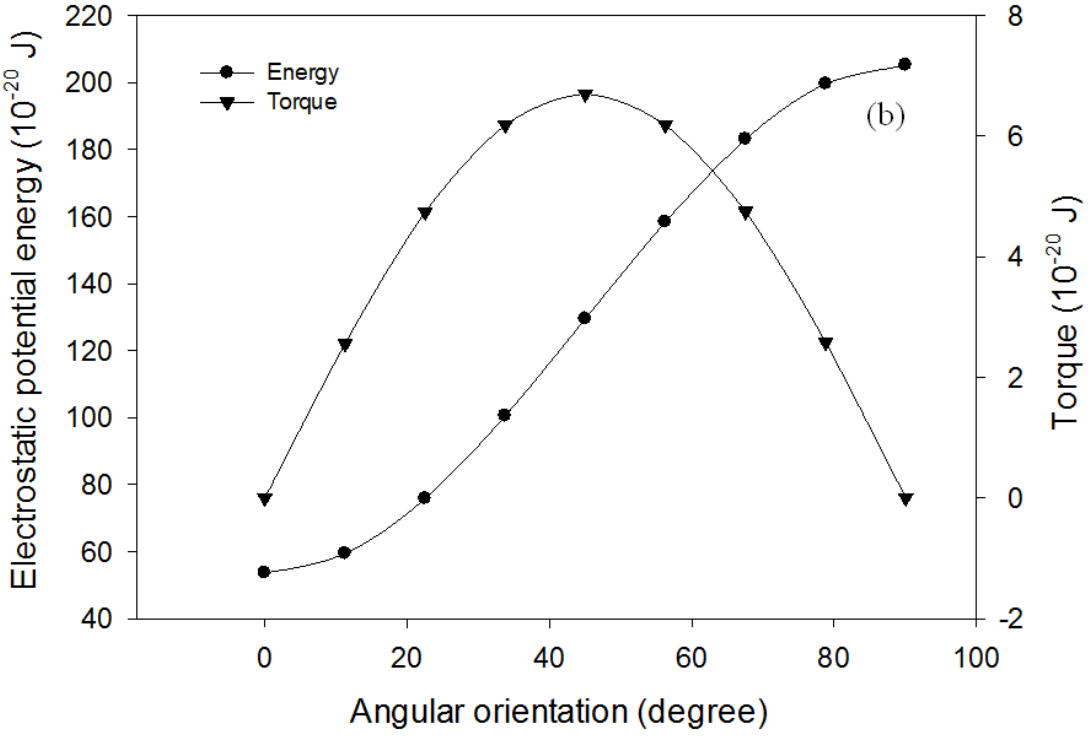
Energy
Torque
(b)
Electrostatic potential energy (10-20 J)
Torque (10-20 J)
Angular orientation (degree)
220
200
180
160
140
120
100
80
60
40
8
6
4
2
0
-2
0
20
40
60
80
100

FIG. 8. (a) Variation of electrostatic potential energy and torque on a single ellipsoidal particle when it rotates for 360 degree. (b) Variation of electrostatic potential energy and torque on the middle spherical particle in three particle chain when the chain rotates for 90 degree.

B. Determination of the stable orientation of ellipsoidal particle chain

We first define the tilting angle as the angle between the major axis of ellipsoidal particle and electric field. Fig. 9(a) shows that when the major axes of all three particles are parallel to the electric field (tilting angle equals 0 degree), the energy reaches its minimum when the chain of particles forms a small angle with respect to the electric field, different from the case for spherical particles where an energy minimum is obtained when the chain is parallel to the electric field. By examining the torque exerted on the middle particle, we noted that the torque is negative. When the angle between the chain and electric field further increases, the torque will become even more negative, indicating that the middle particle will rotate clockwise about its geometric center. This will lead to disassembly of the chain structure. To obtain a stable configuration for the chain, we gradually rotate each ellipsoid particle about its geometric center clockwise (increase the tilting angle) and evaluate the change in energy and torque with respect to the angle between the line connecting geometric centers of particles and the major axis of particles. As shown in Fig. 9(a), the minimum energy will gradually decrease when the tilting angle increases. When the tilting angle reaches 6°, the minimum energy is the lowest. At this

minimum energy configuration, the angle between the line connecting geometric centers of particles and the major axis of particle is at 12.5° and the torque is positive to ensure contacts between particles. Further increase in tilting angle will lead to increase of the minimum energy, thus the angle between the particle chain and electric field is calculated as 6.5° when the chain is in its lowest minimum energy orientation. Similarly we can determine the most probable angle between particle chain and electric field for ellipsoidal particles with aspect ratio of 4.3 and 7.6 (Table 4).

Table 4. Most probable angle between chain and electric field from modeling and experimental results

	Most probable angle between chain and electric field (modeling)	Most probable angle between chain and electric field (experiment)
Aspect ratio = 3 (degree)	6.5	13
Aspect ratio = 4.3 (degree)	5	12
Aspect ratio = 7.6 (degree)	3	12

Table 4 shows that probable stable angles predicted from modeling are smaller than the statistical average values measured in experiments. This difference may be attributed to the contact surface topology affecting the stability of configuration. Since the contact between irregular surfaces is a complex issue, it is almost impossible to consider the actual contact in modeling. One may interpret the impact of contact surface topology in an intuitive way. For example, the curvature is larger on the major axis end of particle, leading

to more concentrated distribution of normal force. Thus, ellipsoidal particles may favor a contact in the small curvature region, causing the most probable angle to increase.

Fig. 9(b) shows the variation of energy with respect to chain angle. The horizontal line represents the lowest energy of a single particle. The results suggest that when the chain angle is smaller than 26 degree the chain is likely to be stable. Table 5 shows the comparison of modeling and experimental results for all three kinds of particles. The negative value is due to the small tilting angle of particle with respect to electric field. Modeling results agrees with experimental observation by predicting a narrower chain angle distribution as the aspect ratio increases.

Table 5. Distribution of angle between chain and electric field from modeling and experimental results

	Distribution of angle between chain and electric field (modeling)	Distribution of angle between chain and electric field (experiment)
Aspect ratio = 3 (degree)	-6 ~ 26	4 ~ 32
Aspect ratio = 4.3 (degree)	-4 ~ 20.5	4 ~ 26
Aspect ratio = 7.6 (degree)	-2 ~ 13	4 ~ 20

As we have pointed out earlier that the surface conductance of particle is unknown and likely to affect the stable orientation of chain, three surface conductance values (1.2 nS, 6.0 nS and 12 nS) are assigned to the ellipsoidal particle with aspect ratio of 3

(corresponding conductivity of particle equals 1.6×10^{-3} S/m, 8×10^{-3} S/m and 1.6×10^{-2} S/m). Fig. 9(c) shows the variation of energy with respect to the angle between line connecting centers of particles and major axis. For all surface conductance cases, the electrostatic potential energy reaches its minimum value at almost the same angle, suggesting that the surface conductance has a minor effect on the stable orientation of the particle chain.

Further addition of more particles could lead to a structure shown in Fig. 3(d). To have such a structure as a favored configuration, the energy of the middle particle in stacked configuration should be lower than that of the middle particle in a chain. Fig. 9(d) shows the variation of energy with respect to the angle between line connecting centers of the middle particle and one of the surrounding particle and the major axis. Below 12°, the surrounding particles will overlap with each other geometrically. The lowest energy of stacked particles (1.2×10^{-20} J) is much lower than the lowest energy of particle in a chain (16×10^{-20} J). This suggests that the stacked configuration is more energy-favored than the chain configuration.

The modeling results from volumetric-integration method are then compared with previous modeling results from other modeling methods. In Singh et al (2009), both the particle and medium are treated as pure dielectric material. As the frequency of the AC signal is set only 10 kHz, the contribution of conductivity dominates that of permittivity according to the expression of complex permittivity $\varepsilon^* = \varepsilon - i\frac{\sigma}{\omega}$, suggesting the simplification is wrong. In House et al (2012), dynamic modeling based on the MST method was adopted. However, the predicted angles are far different from the experimental

measurement. Although the influence of contact surface topology has not been accounted for, our modeling results nevertheless provide coherently explanations for the angle distribution of the particle chain and the transition from a chain configuration to a stacked configuration.

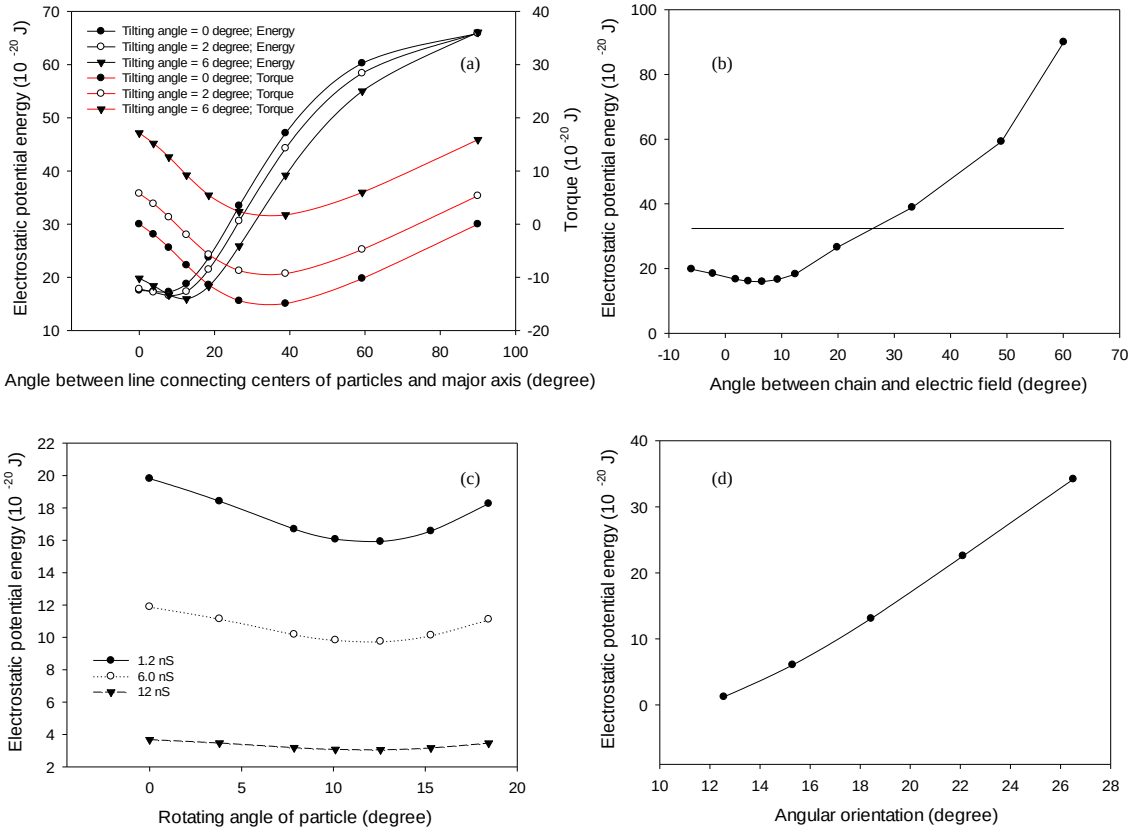

FIG.9. (a) Variation of electrostatic potential energy and torque on the middle ellipsoidal particle in three-particle pearl chain as the chain rotates for 90 degree. (b) Variation of electrostatic potential energy of the middle ellipsoidal particle in chain with respect to chain angle and the minimum energy of a single ellipsoidal particle. (c) Particles with different surface conductance have minimum electrostatic potential energy value around the same angle. (d) Variation of electrostatic potential energy of the middle ellipsoidal particle in stacked configuration with respect to diagonal chain angle.

4.6 Conclusions

This work reported a newly observed movement of pearl chains in a fluid flow condition under DEP and developed a computational model based on the volumetric-integration method to explain the underlying cause for such movements using a static-force analysis approach and dynamic ALE approach, and the alignment of ellipsoidal particles. Results confirm the strength of the volumetric-integration method in explaining how particles interact with each other under DEP. It is believed that this method will help advance and accelerate new applications of the DEP technique in biomanufacturing.

Reference

Ai, Y., and Qian, S., "DC dielectrophoretic particle–particle interactions and their relative motions," Journal of colloid and interface science 346, 448-454 (2010)

Ai, Y., Zeng, Z., and Qian, S., "Direct numerical simulation of AC dielectrophoretic particle–particle interactive motions," Journal of colloid and interface science 417, 72-79 (2014)

Arnold, W. M., Schwan, H. P., and Zimmermann, U., "Surface conductance and other properties of latex particles measured by electrorotation," Journal of Physical Chemistry 91, 5093-5098 (1987)

Church, C., Zhu, J., Nieto, J., Keten, G., Ibarra, E., and Xuan, X., "Continuous particle separation in a serpentine microchannel via negative and positive dielectrophoretic focusing," Journal of Micromechanics and Microengineering 20, 1–6 (2010)

Church, C., Zhu, J., and Xuan, X., "Negative dielectrophoresis-based particle separation by size in a serpentine microchannel," Electrophoresis 32, 527–531(2011)

Gel, M., Kimura, Y., Kurosawa, O., Oana, H., Kotera, H., and Washizu, M., "Dielectrophoretic cell trapping and parallel one-to-one fusion based on field constriction created by a micro-orifice array," Biomicrofluidics 4, 022808 (2010)

Ho, C. T., Lin, R. Z., Chang, W. Y., Chang, H. Y., and Liu, C. H., "Rapid heterogeneous liver-cell on-chip patterning via the enhanced field-induced dielectrophoresis trap," Lab on a Chip 6, 724-734 (2006)

Ho, C. T., Lin, R. Z., Chen, R. J., Chin, C. K., Gong, S. E., Chang, H. Y., Peng, H. L., Hsu, L., Yew, T. R., Chang, S. F., and Liu, C. H., "Liver-cell patterning lab chip: mimicking the morphology of liver lobule tissue," Lab on a Chip 13, 3578-3587 (2013)

House, D. L., Luo, H., and Chang, S., "Numerical study on dielectrophoretic chaining of two ellipsoidal particles," Journal of colloid and interface science, 374, 141-149 (2012)

Kadaksham, J., Singh, P., and Aubry, N., "Manipulation of particles using dielectrophoresis," Mechanics Research Communications 33, 108-122 (2006)

Khan, A. M., and Shah, S. S., "Determination of critical micelle concentration (Cmc) of sodium dodecyl sulfate (SDS) and the effect of low concentration of pyrene on its Cmc using ORIGIN software," JOURNAL-CHEMICAL SOCIETY OF PAKISTAN 30, 186-191 (2008)

Kang, Y., Li, D., Kalams, S. A., Eid, J. E., "DC-Dielectrophoretic separation of biological cells by size," Biomedical Microdevices 10, 243–249 (2008)

Kimura, Y., Gel, M., Techaumnat, B., Oana, H., Kotera, H., and Washizu, M., "Dielectrophoresis‐assisted massively parallel cell pairing and fusion based on field constriction created by a micro‐orifice array sheet," Electrophoresis 32, 2496-2501 (2011)

La Magna, A., Camarda, M., Deretzis, I., Fisicaro, G., Coffa, S., "Coupled Monte Carlo-Poisson method for the simulation of particle-particle effects in dielectrophoretic devices," Applied Physics Letters 100, 2–7 (2012)

Lapizco-Encinas, B. H, Simmons, B. A., Cummings, E. B., Fintschenko, Y., "Dielectrophoretic Concentration and Separation of Live and Dead Bacteria in an Array of Insulators," Analytical Chemistry 76, 1571–1579 (2004)

Li, M., Li, S., Li, W., Wen, W., and Alici, G., "Continuous manipulation and separation of particles using combined obstacle- and curvature-induced direct current dielectrophoresis," Electrophoresis 34, 952–960 (2013)

Mittal, M., and Furst, E. M., "Electric Field‐Directed Convective Assembly of Ellipsoidal Colloidal Particles to Create Optically and Mechanically Anisotropic Thin Films," Advanced Functional Materials 19, 3271-3278 (2009)

Moon, H. S., Kwon, K., Kim, S. I., Han, H., Sohn, J., Lee, S., Jung, H. I, "Continuous separation of breast cancer cells from blood samples using multi-orifice flow fractionation (MOFF) and dielectrophoresis (DEP)," Lab on a Chip 11, 1118–1125 (2011)

Singh, J. P., Lele, P. P., Nettesheim, F., Wagner, N. J., and Furst, E. M., "One-and two-dimensional assembly of colloidal ellipsoids in ac electric fields," Physical Review E 79, 050401 (2009)

Wang, X. B., Huang, Y., Becker, F. F., and Gascoyne, P. R., "A unified theory of dielectrophoresis and travelling wave dielectrophoresis," Journal of Physics D: Applied Physics 27, 1571-1574 (1994)

Zhao, Y., Brcka, J., Faguet, J., and Zhang, G., "Elucidating the DEP phenomena using a volumetric polarization approach with consideration of the electric double layer," Biomicrofluidics 11, 024106 (2017)

CHAPTER FIVE

PRELIMINARY STUDY ON THE FLOW REVERSAL BEHAVIOR OF ACEO

5.1 Introduction

Different from DEP, AC-electroosmosis (ACEO) is a phenomenon which occurs in a much narrower frequency range. Instead of inducing movement of particles, ACEO causes the movement of fluid by the electrostatic force exerted on the charges in EDL surrounding electrodes. Thus, an ACEO phenomenon only occurs when the fluid is in contact with the surface of electrodes. Like traveling wave dielectrophoresis (tw-DEP), ACEO is often used as a technique for microscale pumping purpose. The velocity of ACEO flow can be as high as several hundred μm/s with low-voltage excitation, assuring high efficiency (Green *et al* 2000) in operations. Other than pumping application, ACEO can also be used for mixing purpose (Huang *et al* 2007). In this study, we investigated the ACEO with a set of spiral electrodes to study the influence of voltage and frequency of biasing signal on the ACEO flow behavior. Aside from experimental investigation we also developed a COMSOL model with consideration of the EDL surrounding the electrodes and the Faradic current due to hydrolysis at the surface of the electrodes. The results provide some new understanding regarding the effect of electrochemical reactions at the electrode surface on the ACEO and reasonable explanations for the not-yet-understood flow reversal phenomenon commonly observed under ACEO.

5.2 Material and methods

A set of four spiral electrodes is fabricated on glass slides using conventional photolithographic technique. The width of electrodes and gap distance between electrodes are set at 20 μm. A liquid well is formed by laser cutting on double-sided adhesives stuck on a base slide. During experiments, polystyrene particles suspended in DI water are injected into the well and a cover slip is used to seal the well. AC signals with the same magnitude and frequency at four different phases are applied to each of the four electrodes respectively either in an ascending or descending manner. The phase difference is set at 90 degree between adjacent electrodes. The AC signals are generated by a multichannel waveform generator (WGF600; FLC Electronics Inc., Sweden). All optical images are recorded with an inverse optical microscope (Axiovert s100; Zeiss, Germany).

5.3 Experimental observation

Particles are dispersed in DI water with conductivity around 1.8×10^{-4} S/m. When AC potential signals at 6 V_{pp} and 1 kHz with ascending phase from outside to inside are applied to the spiral electrodes, particles will move towards the center region with high velocity (Fig. 1(a)). Before reaching the center space, particles will rise and then move outwards (Fig. 1(b)). After several seconds, these particles will gradually settle back down. This process will keep going continuously with a slight outward shift in the particle rising position in each consecutive repeat. In a radial sectional view, these particles experience a vortex type of motion (Fig. 1(c)) with the vortex region getting smaller and smaller as time

passes by (Fig. 1(d)). Reversing the phase ascending direction will reverse the particle movement direction (Fig. 2(a)). Similar vortex behavior is seen in a radial sectional view except that the rotating direction is reversed as well (Fig. 2(b)).

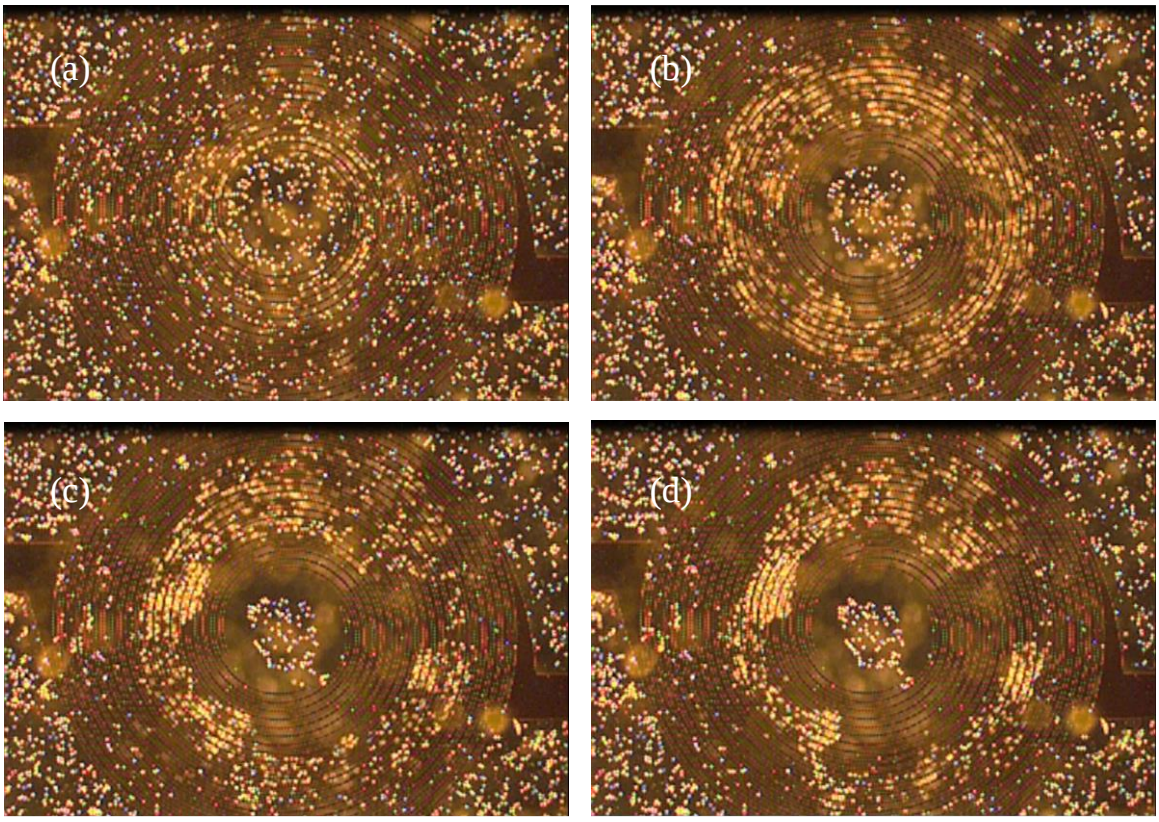

FIG. 1. (a)-(d) Optical images of moving particles under 6 Vpp, 1 kHz potentials with ascending phase at different stages.

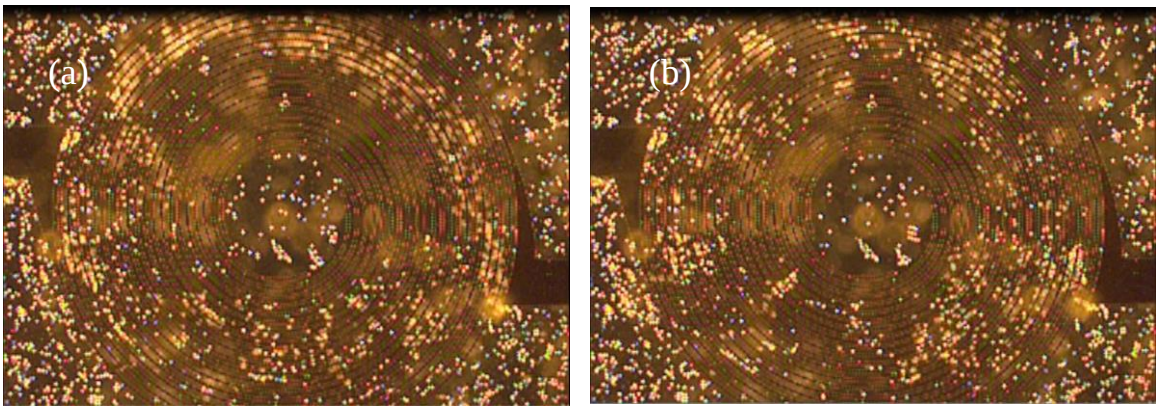

FIG. 2. (a)-(b) Optical images of moving particles under 6 Vpp, 1 kHz potentials with descending phase at different stages.

During the experiments, we observed that there exists a critical value for the potential magnitude at a given frequency below which the moving velocity of particles is quite slow and no obvious large-scale particle movement is seen, and above which, motion of particles is enhanced. By examining the relationship between this critical potential and frequency, we noted that this critical potential value will increase as frequency increases (Table 1). Note that although the critical value is listed at 4 V_{pp} for both 100 Hz and 1 kHz cases, the velocity of particles is much higher at 100 Hz. At a lower frequency, the vortex motion is more stable and particles tend to form ring structure. At a higher frequency, the movement will become so chaotic that a critical potential value does not exist for situations with frequency above 25 kHz (Fig. 3(a)-(d)).

Table 1. Frequency of signal and corresponding critical voltage magnitude

Frequency (kHz)	0.1	1	5	10	25
Critical voltage magnitude (V_{pp})	4	4	8	10	14

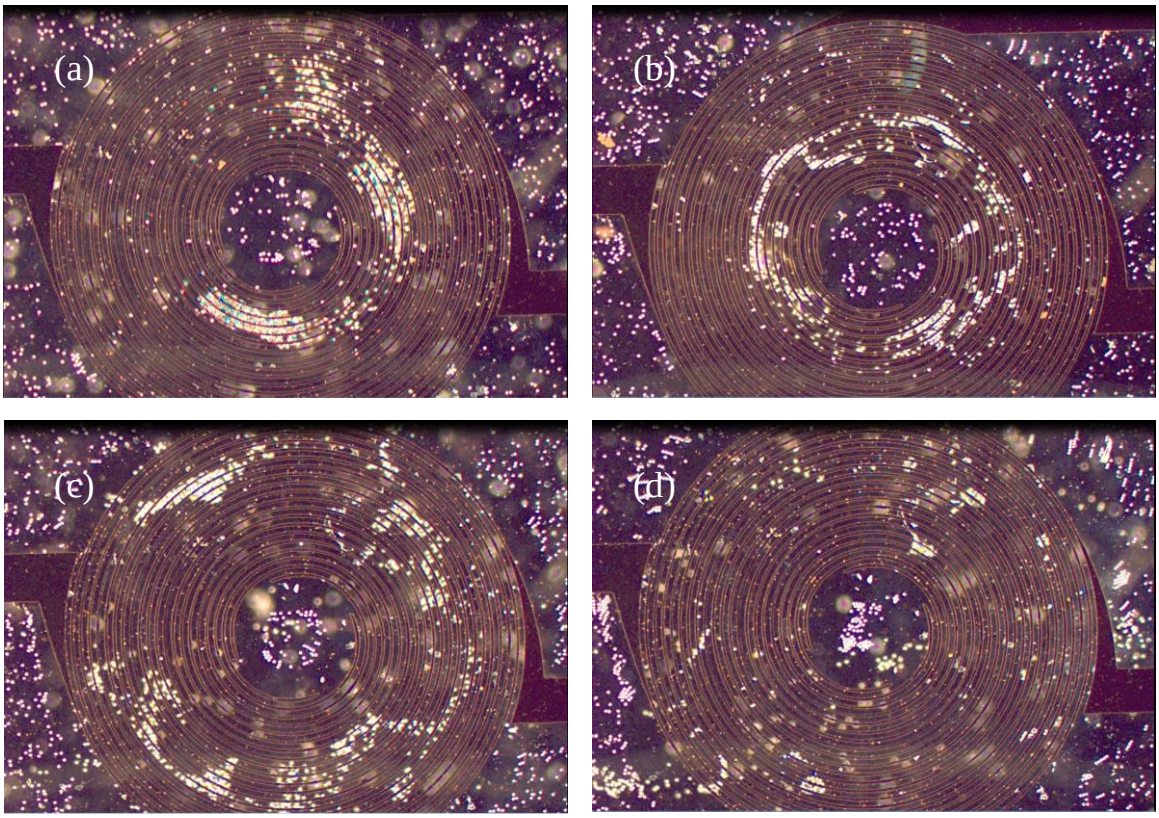

FIG. 3. Distribution of particles under critical voltage after 50 seconds. (a) 4 Vpp, 100 Hz (b) 4 Vpp, 1 kHz (c) 10 Vpp, 10 kHz (d) 14 Vpp, 25 kHz.

5.4 Modeling results

2D model was built to simulate the ACEO phenomenon. The geometry of the model is shown in Fig. 4. The four blue lines at the bottom of the model represent the biased electrodes. The phase increases from left to right. Both the width of electrodes and gap distance are set to be 20 μm. The rectangle domain is filled with pure water with no other ions. The ions considered in the model come from the dissociation of water. Outside the electrodes an insulation layer with thickness of 1 nm is considered to represent the stern layer. The ion distribution in the EDL can be solved by the diffusion and migration equation:

$$\frac{\partial c_i}{\partial t} + \nabla \cdot (-D_i \nabla c_i - z_i u_{m,i} F c_i \nabla V) = R_i \tag{5}$$

$$N_i = -D_i \nabla c_i - z_i u_{m,i} F c_i \nabla V \tag{6}$$

where c_i is the concentration, D_i the diffusion coefficient, z_i the valence charge, $u_{m,i}$ the mobility ($u_{m,i} = \frac{D_i}{RT}$), R_i the rate of concentration change, N_i the flux of ion *i*. As there are only two types of ions in medium: H^+ and OH^-, the concentration of both ions are determined by the self-ionization of water $H_2O \rightleftarrows H^+ + OH^-$. The production rate of H^+ and OH^- can be expressed as:

$$R_{H^+} = R_{OH^-} = k_d c_{H_2O} - k_b c_{H^+} c_{OH^-} \tag{7}$$

where k_d and k_b are the forward and backward reaction rate constant.

By solving Eqs. (5) - (7), the distribution of ions can be determined. Then the electrostatic force density exerted on medium can be expressed as:

$$f = F(c_{H^+} - c_{OH^-}) \cdot \vec{E} \tag{8}$$

With parameters listed in Table 2, Laminar Flow Module, Electric Current Module and Transport of Dilute Species Module are simultaneously solved in Time Dependent Study. Based on the frequency of the signal, the model is solved for two cycles. Each cycle is divided into 16 uniform periods. The flow velocity at each point is obtained by calculating the average value in the second cycle.

Table 2. Parameters used in the model

Parameter	Value	Physical meaning
D_{H^+}	9.31×10^{-9} m^2/s	Diffusion coefficient of H^+
D_{OH^-}	5.30×10^{-9} m^2/s	Diffusion coefficient of OH^-
T	293.15 K	Temperature
k_b	1.3×10^{8} $m^3/(mol\cdot s)$	Backward reaction rate constant of self-ionization
k_d	2.3×10^{-5} 1/s	Forward reaction rate constant of self-ionization
V_0	3 V	Standard potential
k_e	10^{-20} $mol/(m^2\cdot s)$	Reaction rate constant of water electrolysis

L	10^{13}	Parameter to characterize the conductivity of fluid

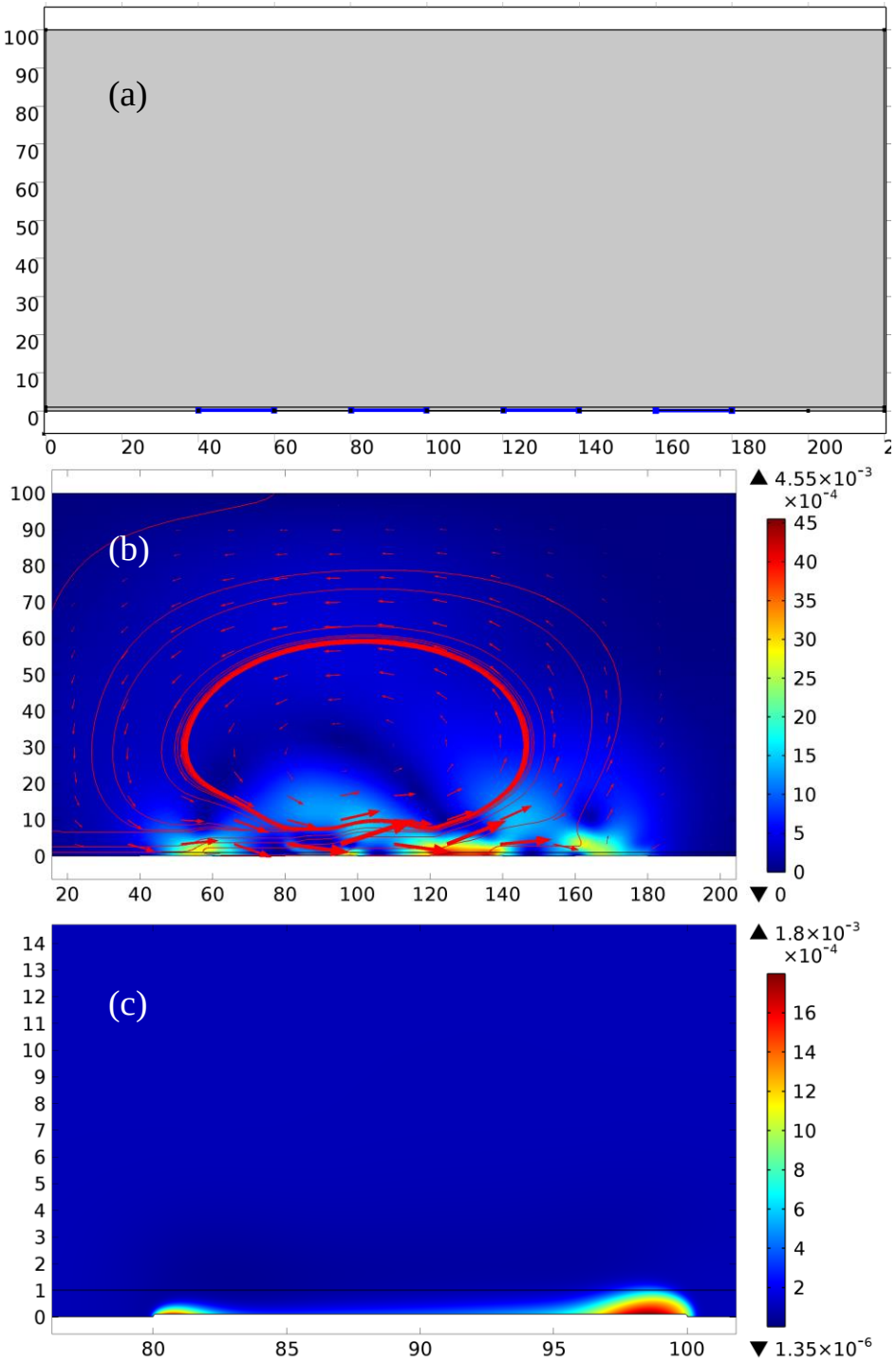
(a)
(b)
(c)
▲ 4.55×10^-3
×10^-4
▼ 0
▲ 1.8×10^-3
×10^-4
▼ 1.35×10^-6

FIG. 4. (a) Geometry of the 2D model for simulating ACEO phenomenon. (b) ACEO flow profile and particle trajectory under 4 Vpp at 1 kHz. (c) Concentration of H^+ in the EDL around the electrode surface.

Fig. 4(b) shows the flow profile at 4 Vpp and 1 kHz. The arrows point to the directions of flow and the streamlines represent the trajectories of a moving particle starting from the bottom. The particle will move in a vortex motion whose size gradually reduces. This vortex motion behavior agrees with experimental observation and is consistent with other simulation works (Pham *et al* 2007). However, the direction of the vortex flow predicted by our model is opposite to our experimental observation. This phenomenon has also been observed and regarded as flow reversal behavior of ACEO (García-Sánchez *et al* 2006). Currently there are two explanations for this flow reversal behavior. The first explanation attributes it to the Faradic current occurring at the electrode surface leading to a change in polarity of the EDL (García-Sánchez *et al* 2009, Yang and Wu 2008). The second explanation claims that steric effect is the cause of flow reversal (Storey *et al* 2008). In examining the concentration of ions at the electrode surface, as shown in Fig. 4(c), we noted that the concentration is relatively low hence it will not likely lead to steric blockage.

In view of the possible hydrolysis occurring at the electrode surface under electric biasing we hypothesize that the flow reversal may be caused by undergoing Faradic current caused by hydrolysis at the electrode surface. The exponential relationship between reaction rate and voltage dictated by Butler-Volmer equations are likely to be the cause of this transition. To prove our hypothesis, we incorporate electrochemical reactions in our

model to examine such a possibility, and we do so by implementing a predefined expression for the flux of ions at electrode surface as a result of the electrochemical driven hydrolysis as a function of the applied electrode potential.

Since there are four electrodes in the model, we consider two at a time as a pair sequentially (6 pairs in total in combination). For a given pair, the voltages on electrodes 1 and 2 are represented by $V1$ and $V2$. At the electrode of a higher voltage, oxygen gas and H^+ will be generated and at the electrode of a lower voltage, hydrogen gas and OH^- will be generated. Thus the H^+ and OH^- fluxes at electrode 1 can be expressed as:

$$\begin{aligned} j_{H^+} &= k_e \exp(F \cdot (V1 - V2 + V0) / RT) \cdot (V1 - V2 > 0) \\ j_{OH^-} &= k_e \exp(F \cdot (V2 - V1 + V0) / RT) \cdot (V2 - V1 > 0) \end{aligned} \tag{9}$$

where k_e is the reaction rate constant of water electrolysis and $V0$ is the standard potential of water electrolysis reaction. Under DC signal, $V0$ = -1.23 V. The exact value of $V0$ under AC condition is unknown at current stage. Theoretically it should be more negative as the constantly changing direction of current flow does not favor the reaction. In the model we assume that $V0$ = -3 V at 1 kHz. Here we choose -3 V so that the voltage at which flow reversal behavior occurs is consistent with experimental observations. By examining Eq. (9), we find that the flux will increase exponentially, this is not true as we know the flux is also dependent on the conductivity of the medium. Thus we modify Eq. (9) as shown below:

$$j_{H^+} = \frac{k_e \exp(F \cdot (V1 - V2 + V0) / RT) \cdot L \cdot abs(V1 - V2) \cdot F / RT (V1 - V2 > 0)}{\exp(F \cdot (V1 - V2 + V0) / RT) + L \cdot abs(V1 - V2) \cdot F / RT}$$
$$j_{OH^-} = \frac{k_e \exp(F \cdot (V2 - V1 + V0) / RT) \cdot L \cdot abs(V1 - V2) \cdot F / RT (V2 - V1 > 0)}{\exp(F \cdot (V2 - V1 + V0) / RT) + L \cdot abs(V1 - V2) \cdot F / RT} \quad (10)$$

where L is a parameter characterizing the conductivity of the medium. When the voltage difference between $V1$ and $V2$ is small, the flux is determined by the exponential term. When the difference becomes large, the flux becomes proportional to the voltage difference. Eq. (10) is logically feasible and we implement it to the model to see if it can predict the flow reversal behavior.

Fig. 5(a)-(c) shows the flow direction under different voltages at 1 kHz. Under 3 Vpp, the flow is in the same direction as shown in the case where water electrolysis is neglected. When the voltage is increased to 4 Vpp, the flow direction is reversed. Further increase of the applied potential to 5 Vpp leads to more uniform flow with higher velocity. Fig. 5(d) shows that the flow reversal also occurs at 10 Vpp and 5 kHz. These results support our hypothesis that the flow reversal is caused by water electrolysis reaction.

Consequently, we expect the pH value of liquid medium will affect the fluid flow under ACEO. To demonstrate that, the pH value of the medium is adjusted to 11.5 by adding $NaOH$ in the solution and with signals at 6 V_{pp} and 100 Hz having ascending phases from outside to inside applied to the spiral electrodes. Different from the case of DI water, particles will move outwards instead of moving inwards.

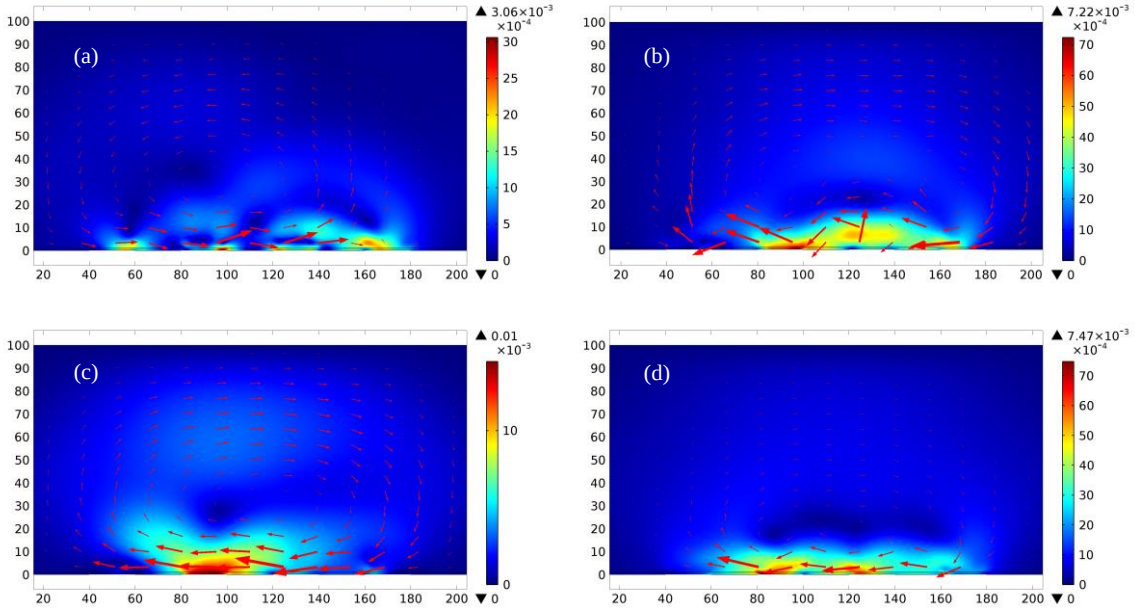

FIG. 5. (a)-(c) ACEO flow profile under different voltages at 1 kHz by accounting for water electrolysis. (a) 3 Vpp (b) 4 Vpp (c) 5 Vpp. (d) ACEO flow profile under 10 Vpp at 10 kHz by accounting for water electrolysis.

5.5 Conclusions

The ACEO flow is generated by using a set of spiral electrodes biased by AC signals with different phases. With this setup, we observed the commonly reported flow reversal behavior. To elucidate the underlying mechanism, we expanded upon our volumetric integration method by accounting for the ion fluxes generated by electrochemical reactions at the surface of electrodes to investigate the ACEO flow behavior. The obtained results show that our new method shed new insight into the cause of commonly observed but not-yet-understood the flow reversal behavior.

Reference

García-Sánchez, P., Ramos, A., González, A., Green, N. G., and Morgan, H., "Flow reversal in traveling-wave electrokinetics: An analysis of forces due to ionic concentration gradients," Langmuir 25, 4988-4997(2009)

García-Sánchez, P., Ramos, A., Green, N. G., and Morgan, H., "Experiments on AC electrokinetic pumping of liquids using arrays of microelectrodes. IEEE Transactions on Dielectrics and Electrical Insulation 13, 670-677 (2006)

Green, N. G., Ramos, A., González, A., Morgan, H., and Castellanos, A., "Fluid flow induced by nonuniform ac electric fields in electrolytes on microelectrodes. I. Experimental measurements," Physical review E 61, 4011-4018 (2000)

Huang, S. H., Wang, S. K., Khoo, H. S., and Tseng, F. G., "AC electroosmotic generated in-plane microvortices for stationary or continuous fluid mixing," Sensors and Actuators B: Chemical 125, 326-336 (2007)

Pham, P., Howorth, M., Planat-Chrétien, A., and Tardu, S., "Numerical simulation of the electrical double layer based on the poisson-boltzmann models for ac electroosmosis flows," In Excerpt from the Proceedings of the COMSOL Users Conference 2007 Grenoble.

Storey, B. D., Edwards, L. R., Kilic, M. S., and Bazant, M. Z., "Steric effects on ac electro-osmosis in dilute electrolytes," Physical Review E 77, 036317 (2008)

Yang, K., and Wu, J., “Investigation of microflow reversal by ac electrokinetics in orthogonal electrodes for micropump design,” Biomicrofluidics 2, 024101 (2008)

CHAPTER SIX

CONCLUSIONS AND FUTURE WORK

6.1 Conclusions

This dissertation presents an extensively investigation of the DEP phenomena and some preliminary study on the ACEO phenomena. It is often perceived that current DEP theories are capable of explaining experimental observations and guiding designs for EDP applications. However, through carefully examination of the derivation process of both the point-dipole method and MST method in elucidating the DEP mechanism, the author found some inherent limitations in both methods. To overcome these limitations, a new volumetric-integration method has been utilized to reexamine the DEP phenomena and elucidate the underlying mechanism.

The results obtained from this new method are compared with those from the other two methods for quantifying the DEP force on both homogeneous and non-homogeneous particles. These comparisons show that the new method can accurately quantify not only the DEP force and but the particle-particle interaction force as well. It also shed some new insight into the impact of EDL structure on the crossover frequency of particles.

The unique strength of this new volumetric-integration method is further demonstrated when it is used to explain the observed cell behavior under DEP and particle-particle interactions. Additionally, this new method has also been utilized to study the ACEO phenomena with the consideration of ion flux (due to hydrolysis) at the surface of

electrodes under AC potential signals and provided reasonable explanations for the not-yet-understood flow reversal phenomenon commonly observed under ACEO.

6.2 Future work

Although the volumetric-integration method has been proven to be powerful in explaining many well reported as well as newly observed DEP phenomena, it is still challenging to deal with the dynamic behavior of a large numbers of particles. In future studies, the volumetric-integration method shall be incorporated with other methods (e.g. Monte-Carlo method) to overcome this drawback such that the volumetric-integration method can be applied to advance the DEP field to meet large-scale biofabrication and biomanufacturing needs. Moreover, the volumetric-integration method needs to be further expanded to consider the more intricate structures of individual cells and cell population to provide full understanding of the DEP driven cell clustering, grouping, alignment, and patterning behavior of the same type of cells or different types of cells. On elucidating the flow reversal behavior under ACEO, although this new method has provided reasonable insight, the relationship between the critical potential magnitude and frequency has yet to be established. Thus, it needs to be modified and refined to provide coherent explanations for all experimental observations.